

RES

THE SCHOOL
for RENEWABLE ENERGY SCIENCE

**Porosity Evolution in the Newberry Volcano
Geothermal System, Oregon, USA:
Feedback between deformation and alteration**

James Andrew Fetterman



UNIVERSITY OF ICELAND



University
of Akureyri

**Porosity Evolution in the Newberry Volcano
Geothermal System, Oregon, USA:
Feedback between deformation and alteration**

James Andrew Fetterman

A 30 ECTS credit units Master's thesis

Supervisors

Dr. Nicholas Davatzes, Temple University, USA

A Master's thesis done at

RES | The School for Renewable Energy Science

in affiliation with

University of Iceland &

University of Akureyri

Akureyri, February 2010

Porosity evolution in Newberry Volcano Geothermal System: Feedback between deformation and alteration

A 30 ECTS credit units Master's thesis

© James Andrew Fetterman, 2010

RES | The School for Renewable Energy Science

Solborg at Nordurslod

IS600 Akureyri, Iceland

Telephone + 354 464 0100

www.res.is

Printed in 2011

at Stell Printing in Akureyri, Iceland

ABSTRACT

This study attempts to quantify a relationship between 1) fracture porosity, 2) deformation and 3) mineral precipitation and hydrothermal alteration in crystalline basaltic rock from Newberry Volcano in Oregon. It attempts to find a quantifiable set of restraints for these three factors that will maximize potential for permeability enhancement of low-porosity rock using Engineered Geothermal Systems (EGS) technology. Porosity of selected samples is mapped in hand sample and microscopically using petrographic analysis with thin sections. Mineralogy is mapped through hand-sample mapping, petrographic analysis and XRD analysis. The transport of elements due to fluid flow is quantified through XRF analysis.

The generation of skeletal and open porosity through dilation is explored in two end member systems, non-clay and clay-dominated fractures. Data gathered in this study suggests that both systems evolve and grow in complexity via the same processes up until a critical stage in fracture evolution. In early stages of fracture evolution, both the create porosity via dilation during slip, into which geofluids can precipitate and provide high-strength cement to support re-fracturing. After the critical point in non-clay fractures, porosity generation can outpace mineral precipitation and provide open pore space between re-fracturing events, a necessary prerequisite for permeability. After the critical point in clay-filled fractures, slip ceases to generate significant porosity from dilation during slip due to the “clogging” effect of the clay. Nevertheless, clay fractures widen and develop complexity over time due to alteration at the fracture core/damage zone boundary fed by fluids via microscopic porosity.

Table of Contents

1	Introduction	1
1.1	Overview	1
1.2	Definition of Terms.....	1
1.3	The Geothermal Potential of Newberry Volcano.....	2
1.4	Geologic History of Newberry Volcano	3
1.5	Fracture Permeability	7
1.5.1	Calcite and silica healing in non-clay filled fractures.....	7
1.5.2	Clay-lined fractures.....	10
1.6	Fracture Evolution.....	10
2	Methodology	12
2.1	Trace Mapping.....	15
2.1.1	Macroscopic porosity measurement.....	16
2.2	Petrographic Microscope Analysis of Representative Thin Sections	16
2.2.1	Microscopic porosity measurement	17
2.3	XRF Analysis.....	19
2.4	XRD Analysis	20
3	Results.....	21
3.1	Macroscopic Porosity Results	21
3.1.1	Photos and maps of macroscopic structures and related healing and porosity characteristics.....	21
3.1.2	Macroscopic skeletal porosity.....	33
3.1.3	Macroscopic open porosity.....	36
3.1.4	Macroscopic maximum porosity trends	37
3.2	Microscopic Porosity Results.....	38
3.2.1	Maps of microscopic structures, fault rocks and related porosity	38
3.2.2	Microscopic skeletal porosity.....	44
3.2.3	Microscopic open porosity.....	47
3.2.4	Microscopic maximum porosity trends	48
3.3	XRF Analysis: Independent Evidence of Fluid Flow.....	48
3.4	Correcting the Macroscopic Data for Clay Fractures.....	55
3.4.1	Macroscopic vs. Microscopic Porosity Measurements	55
3.4.2	Possible errors in porosity measurement.....	56
3.4.3	Method to correct macroscopic porosities in clay stages 4 and 5	58
3.5	XRD Analysis Results	59
3.5.1	Using quartz weight % as an indicator of fracture stage and porosity	59
4	Discussion.....	61
4.1	Implications for Open Porosity in Fracture Systems	61
4.2	A Conceptual Mechanism Model for Clay and Non-Clay Fracturing	64
5	Conclusions	65
6	Acknowledgments.....	66
7	Tables	67
7.1	Table 1	67
7.2	Table 2	68
8	Bibliography	73

LIST OF FIGURES

Figure 1: Regional Map of Newberry Volcano.....	4
Figure 2: Generalized geologic map of Newberry Volcano.....	5
Figure 3: Underneath Newberry Volcano.	6
Figure 4: Idealized non-clay fracture.	9
Figure 5: Idealized clay fracture.....	10
Figure 6: Conceptual model of a fault zone.	11
Figure 7: A schematic diagram of time vs. fracture evolution.	12
Figure 8: Actual fracture evolution, non-clay	13
Figure 9: Actual fracture evolution, clay.....	14
Figure 10: Map of Newberry geothermal wells	15
Figure 11: Example of basaltic host rock thin section view.....	18
Figure 12: Healed crack porosity, defined	19
Figure 13: Coloring scheme for macroscopic mineralogy maps.....	22
Figure 14: Non-clay stage 2 transparency map	23
Figure 15: Non-clay stage 2.5 transparency map	24
Figure 16: Non-clay stage 3 transparency map	25
Figure 17: Non-clay stage 4 transparency map	26
Figure 18: Clay stage 2 transparency map	27
Figure 19: Clay stage 3 transparency map	28
Figure 20: Clay stage 4 transparency map	29
Figure 21: Clay stage 5 transparency map	30
Figure 22: Macroscopic porosity maps, all non-clays.....	31
Figure 23: Macroscopic porosity maps, all non-clays.....	32
Figure 24: Macroscopic skeletal porosity 1/2	34
Figure 25: Macroscopic skeletal porosity 2/2	35
Figure 26: Macroscopic open porosity, all stages	36
Figure 27: Macroscopic maximum porosity trends.....	37
Figure 28: Thin section photos, non-clays	39
Figure 29: Thin section photos, clays.....	42
Figure 30: Thin section porosity maps, all samples	43
Figure 31: Microscopic skeletal porosity 1/2	44
Figure 32: Microscopic skeletal porosity 2/2	46
Figure 33: Microscopic open porosity.....	47
Figure 34: Microscopic maximum porosity trends	48

LIST OF FIGURES (CONT'D)

Figure 35: Non-clay Zr/Ti XRF plots.....	51
Figure 36: Non-clay Ca/Ti XRF plots.....	52
Figure 37: Clay Zr/Ti XRF plots.....	53
Figure 38: Clay Ca/Ti XRF plots	54
Figure 39: Macro vs. micro skeletal porosity comparison	56
Figure 40: Plot of the elements Ti and Zr, which define a line, in clay stage 5	57
Figure 41: Ca/Ti and Sr/Ti XRF plots for clay stage 5	58
Figure 42: Corrected skeletal porosity for clay groups	59
Figure 43: Quartz depletion/enrichment relative to fracture stage.....	60
Figure 44: Open porosity development in non-clay systems	62
Figure 45: Open porosity development in clay systems.....	63

LIST OF TABLES

Table 1 Core sample list	53
Table 2 XRD Reitveld results	54

1 INTRODUCTION

1.1 Overview

This study quantifies the relationship between: (1) fracture porosity and pore geometry, (2) deformation, and (3) mineral precipitation and hydrothermal alteration in crystalline basaltic rocks. Two main types of mineral alteration are distinguished: quartz and silica pore-filling cement and phyllosilicate precipitation into pores or alteration of minerals. Eight core samples from shallow drill cores from Newberry Volcano, near Bend, Oregon are studied to investigate this relationship. These properties evolve during fault formation and recurrent slip, thus the samples represent two sets of four different stages of rock fracture development. The mineralogy of the samples will be determined through hand sample mapping, petrographic, and X-Ray diffraction (XRD) analysis. The transport of elements due to fluid flow is quantified through X-Ray fluorescence (XRF) analysis. The porosity is quantified by pore mapping in thin section. The dependence of porosity generation will be evaluated for its dependence on degree of fault development and alteration type. The primary focus will be to quantify the difference between calcite/silica precipitates vs. phyllosilicate alteration on the porosity of a rock at each stage of its geometric fracture maturation. To simplify the language of this proposal, strong secondary minerals like calcite and silica will be grouped together and referred to at times as “non-clay.” Weaker minerals including phyllosilicates such as smectite, illite, chlorite, as well as other minerals of low strength as compared to the basaltic host-rock, such as talc, serpentine, zeolites and hematite will be grouped together and referred to as “clays.”

Quantifying porosity and its regeneration in fractures and faults lays the groundwork for determining permeability of a rock and its evolution through the life-cycle of a geothermal field. This research will complement future studies in the Newberry geothermal system that will analyze the frictional strength and permeability of fractured rocks. This research will help determine how to best enhance the geothermal fluid production of the Newberry geothermal system by stimulating deformation as part of the U.S. Department of Energy Enhanced Geothermal Systems (EGS) demonstration project at this site.

1.2 Definition of Terms

In this thesis a number of terms will be commonly used regarding porosity, fracturing, and mineralogy. In case the terminology used in this paper do not correlate exactly with terminology of other papers regarding similar subject matter, the following list of terms has been compiled:

- **Host rock**- the original rock within which a fracture or a fault system develops. Can also be referred to as **protolith**.
- **Porosity**- open-space within the rock volume .
- **Primary porosity**- porosity present in the host rock from the time of formation. This includes vugs (vesicles).
- **Secondary porosity**- any porosity generated after the original formation of the host rock. This includes fracture-induced porosity or chemical-induced

porosity, whereby dissolution by geo-fluids or in-place mineral replacement of the host rock create open space.

- **Open porosity**- Open space within the host rock “today”
- **Healed crack porosity**- Any volume added to the rock (i.e., second porosity) that has been filled with a secondary mineral like calcite or alteration material like clays since its formation.
- **Secondary minerals**- minerals brought into a host rock system via transport by geo-fluids (e.g., calcite or quartz, clays).
- **Alteration minerals**- minerals formed by the alteration of primary minerals through heat and pressure via geofluids.
- **Cementing mineral**- A secondary mineral similar in strength to the host rock that fills the open porosity formed by fracturing.
- **Breccia**- broken fragments of the host rock found in the core of the fault zone. The pieces are incongruous to each other due to a material filling the spaces between them, either a secondary mineral or an alteration mineral.
- **Gouge**- The natural progression from breccia; very small, incohesive rock fragments that originate from the host rock but no longer have the same mineralogy due to heavy weathering.
- **Fault core**-central zone of a fault in which the majority of deformation is localized and the original host rock has been destroyed either through grain size reduction or replacement.
- **Damage zone**- volume of elevated deformation adjacent to the fault core and exceeded any pervasive deformation characterizing the rock volume containing the fault.

1.3 The Geothermal Potential of Newberry Volcano

Under Newberry Volcano lies high-temperature rock with the potential to be a source of commercially-viable geothermal energy. However, the low permeability of the volcanic rock prohibits exploitable fluid circulation. Enhanced geothermal systems [EGS] technology may be able to increase Newberry Volcano’s permeability through various means of induced fracturing. Permeability largely depends on connected porosity. Introduction of connected porosity via formation, opening, and slip of fractures is both a critical naturally developing hydrothermal systems and a mechanism employed to enhance natural permeability in Enhanced (Engineered) Geothermal Systems, EGS. Porosity development via fracturing will be the primary area of focus in this study.

The success of EGS at Newberry depends on whether or not fracture-generated porosity remains high or returns to pre-fracturing levels (or even lower) after the fracturing fluid is withdrawn from the system. High porosity can be maintained when mismatch between surface roughness on two fracture surfaces caused by slip props them apart, a process called shear-induced dilation (Brown, 1987). A key control on this potential for dilation is the type of mineral present along the surfaces of the fracture zone. In natural systems that ubiquitously contain fractures, the surfaces of the fractures any ground up rock are subject to chemical interaction with in situ waters providing a natural background of fracture characteristics that will interact with EGS stimulation.

This study uses drill cores from Newberry to examine how a fractures have evolved in basaltic rocks across two different end members of secondary minerals that fill and “heal” existing fractures: (1) brittle quartz/silica and (2) relatively ductile phyllosilicates. By

examining multiple examples of each system, I will determine if re-fracturing “healed” rock tends to promote porosity generation in each of these groups.

This study quantifies stages of fracture evolution by calculating the relative ratio of secondary mineral to host rock using hand sample mapping, petrographic thin-section image analysis and X-Ray Fluorescence (XRF) and X-Ray Diffraction (XRD) analysis. The skeletal and open porosity of each stage is quantified by pore mapping in thin section and in hand sample. If a pattern between mineral ratios and rock porosity can be established, this study will create a method to estimate porosity in potential geothermal rock using drill cuttings, which are less expensive to retrieve than drill core.

This research will complement future studies in the Newberry geothermal system that will analyze the frictional strength and permeability of fractured rocks.

1.4 Geologic History of Newberry Volcano

Newberry Volcano is located near the town of Bend in central Oregon. It is located near the volcanic Cascade Range of the Northwestern United States (Figure 1). The Newberry geothermal system is geologically complex owing to its volcanic origins. The flanks of the volcano are mantled by more than 400 cinder cones and fissure vents, several rhyolitic domes, flows, and pyroclastic deposits (Bargar and Keith, 1999). The Newberry caldera is noted for its numerous obsidian flows (Figure 2). Surface geophysical surveys of resistivity and density suggest that the interior of Newberry volcano consists of three distinct zones, as shown in Figure 3 (Fitterman, 1988). The upper zone is young, relatively unaltered, low in density and high in electrical resistivity. The intermediate zone is more hydrothermally altered, moderately dense and has low electrical resistivity. The lower zone is characterized by high density and high electrical resistivity. All contain layers of mafic to silicic lava flows and tuffs along with their feeder pipes and dikes documented by surface mapping or in wells. Seismic studies reveal a low-velocity zone about three to five kilometers below the surface of the caldera that may be a small molten magma body (Achauer, et al., 1988).

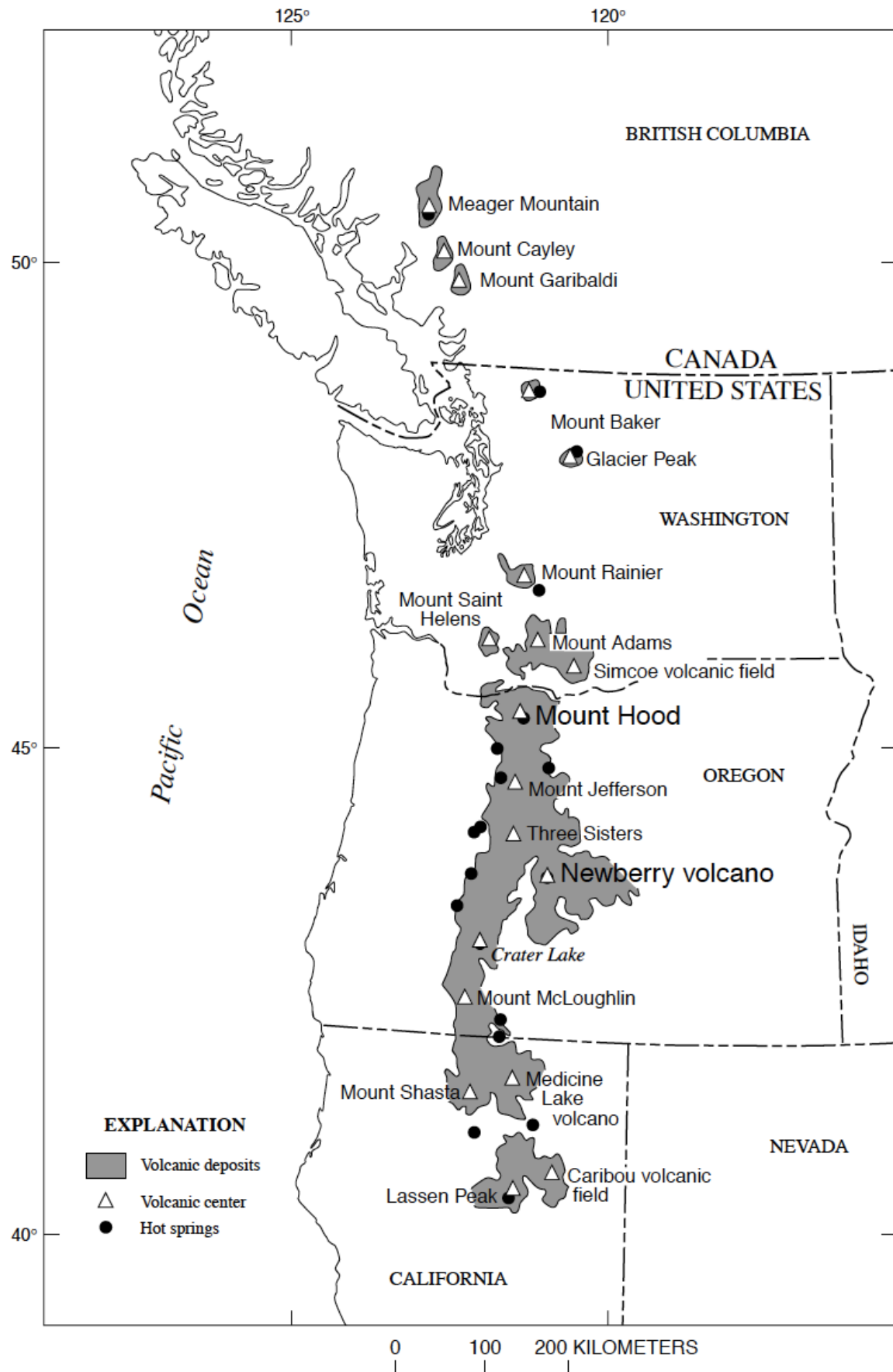


Figure 1: Map showing Newberry Volcano in relation to the Cascade Volcano Range in the northwestern United States (reproduced from Barger and Keith, 1999).

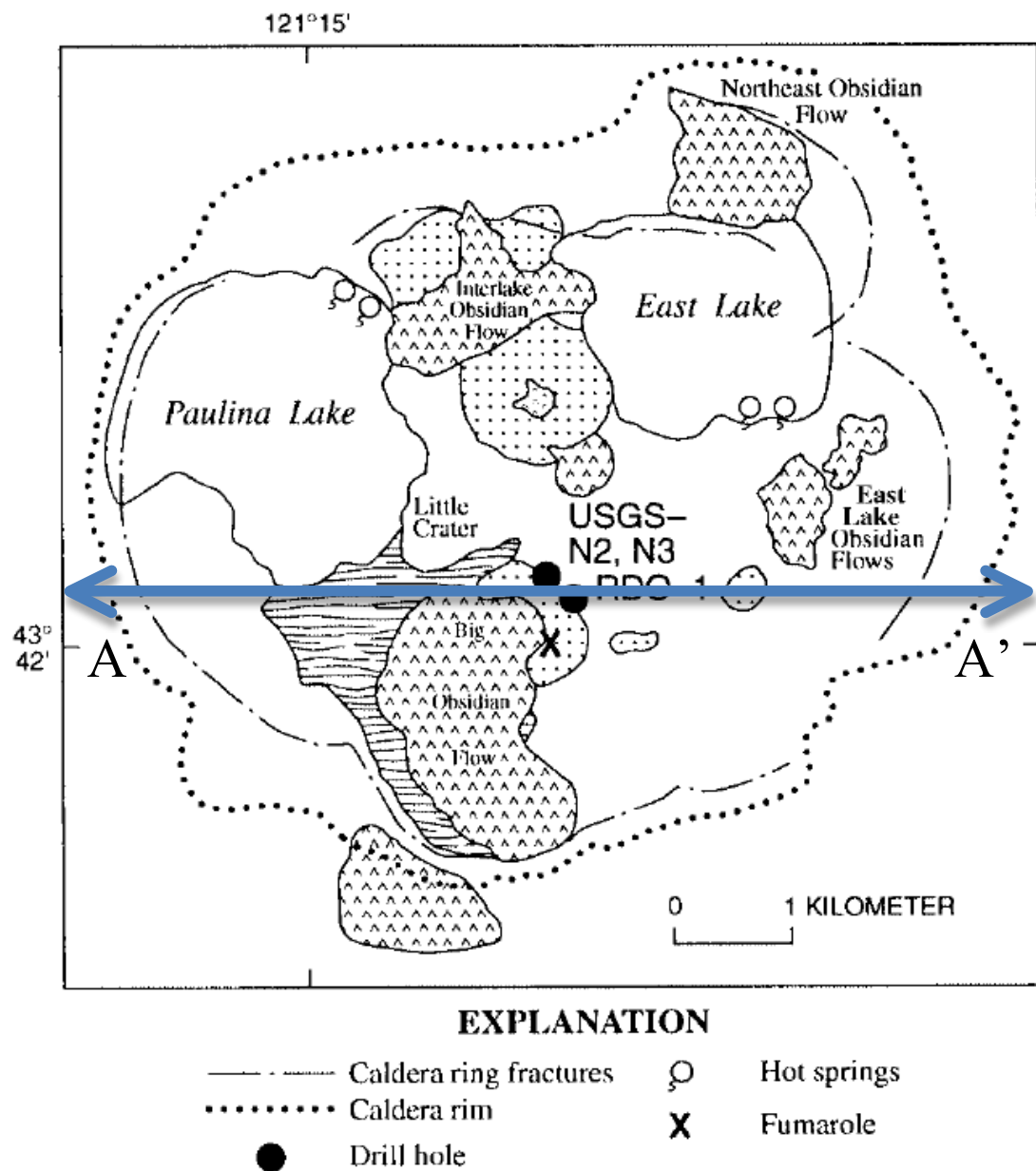


Figure 2: Generalized geologic map and surface hydrothermal features associated with the Newberry caldera geothermal system, Oregon (reproduced from Bargar and Keith, 1999). Line A-A' represents a portion of the schematic cross-sectional length shown in figure 3.

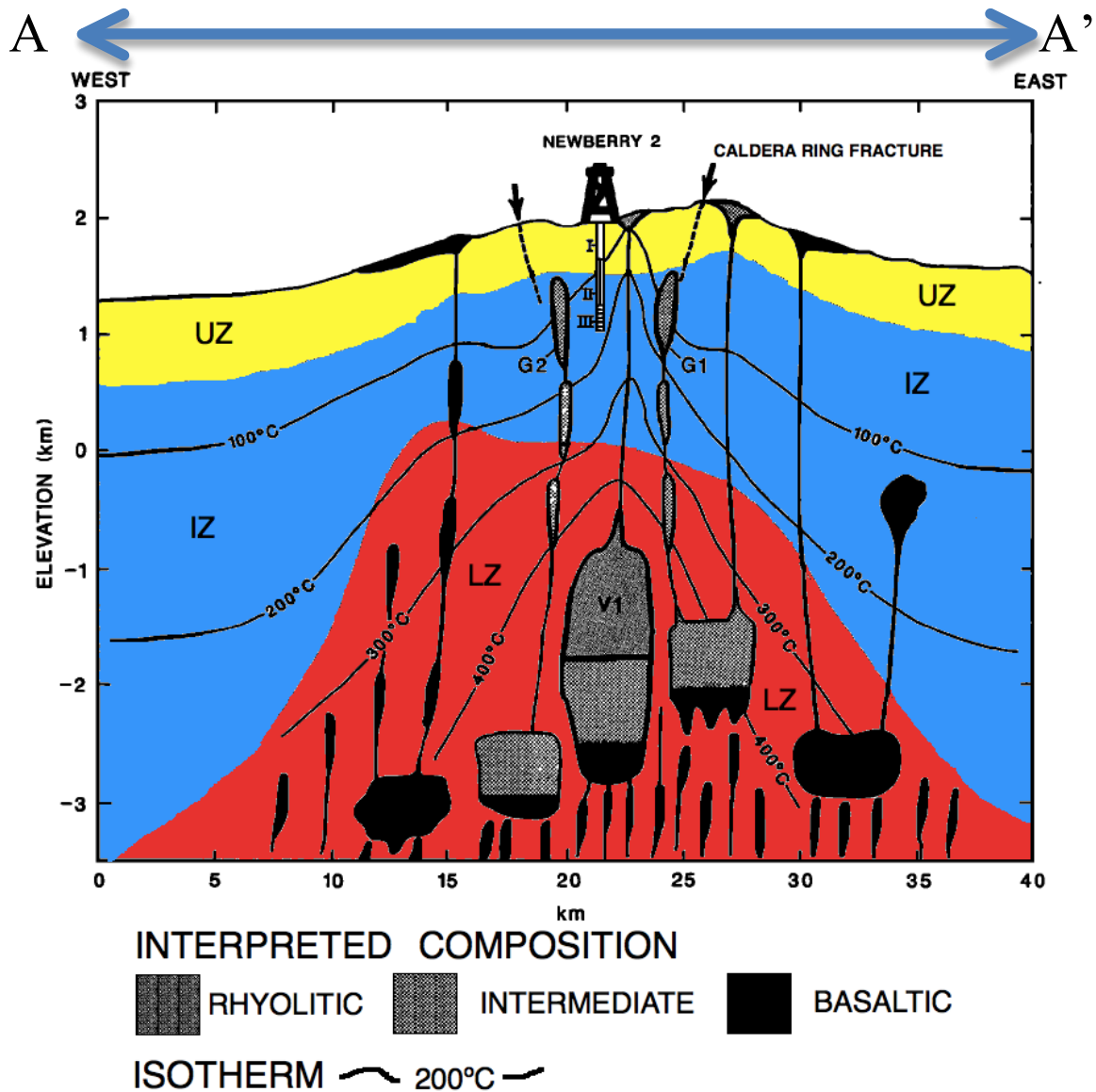


Figure 3: Illustration of three geophysically distinct layers under Newberry Volcano. The upper zone (yellow) has very high resistivity (100-10 $k\Omega m$), low velocity (1.6 $km s^{-1}$) and low density (1.3-2.2 $g cm^{-3}$). The intermediate zone (blue) has low resistivity (8-50 Ωm), intermediate velocity (4.1-4.7 $km s^{-1}$) and moderate density (2.2-2.5 $g cm^{-3}$). The lower zone (red) has high resistivity (300 Ωm), low velocity (1.6 $km s^{-1}$) and high density (2.5-2.8 $g cm^{-3}$). The large pod (V1), thought to be still molten, is inferred from a low-velocity seismic anomaly and the feeder dikes (G1 and G2) are inferred from seismic and gravity anomalies (modified from Fitterman, 1988).

This study will focus on the crystalline basaltic rocks from the interior of Newberry Volcano. Basalt at Newberry is distinguished from rhyolite layers by <52% weight percent SiO_2 (Bargar and Keith, 1999). Compared to basalt, the rhyolitic layers demonstrate a wide range of porosities and mineralogy. Since this study focuses on the evolution of porosity accompanying deformation and/or alteration, comparable initial porosity and mineralogy is preferable to provide a common starting point. Thus, basaltic rocks are preferable to sample over rhyolitic rocks. Vesicular basaltic rock ranges in total porosity, ϕ_{total} , from 5 to 35% (McWhorter and Sunada, 1977; Morris and Johnson 1967). If the

basalt is dense and crystalline, i.e. non-vesicular, the total porosity ranges from 0 to 5% (Freeze and Cherry, 1979).

The eight samples collected for this study were initially identified as basalt in the field. However, closer examination in the lab identified the protolith of the eight samples as ranging from basaltic to andesitic. This range of weight percent of SiO₂ was deemed as an acceptable constraint for this study.

1.5 Fracture Permeability

Fracture permeability is the primary control on the productivity of geothermal reservoirs. Once formed, the walls of fractures or ground rock within fractures can be hydrothermally altered and pore space generated by fracturing can be filled with secondary minerals. These processes change the permeability of the fracture by modifying the geometry and connectedness of pores and its potential for generating new porosity if reactivated. Once formed, fractures form a weakness in the rock mass exploited during subsequent deformations. Thus individual fractures can evolve into a network of interconnecting fractures ultimately leading to the development of larger fault zones comprised of many fracture surfaces and fault rock. As these fractures systems develop they can conduct larger volumes of fluid over distances of kilometers increasing the potential for alteration or precipitation. Thus conducting fluids in geothermal systems depends both on (1) mineralogy and pore structure and (2) this geometric maturation.

Once a host rock is fractured, its mineralogy can be changed in two ways. First, fractures can be sealed by precipitation, most commonly of calcite or silica (Davatzes and Hickman, 2010). Alternatively, fracture surfaces and gouge material within fractures resulting from abrasion of the fracture walls can be altered to phyllosilicates including smectite, illite, chlorite and others (in the order of increasing formation temperature) (Sibson, 2003; Schleicher, et al., 2006; Vrolijk and van der Pluijm, 1999). Such changes in mineralogy impact the strength of the fracture, its potential for reactivation, and its ability to regenerate porosity through dilation and thus permeability.

Mineral precipitation into fractured rock fills pore space generated by the fractures and reduces permeability. However, re-fracturing the rock can promote porosity through dilation, caused by slipping over the roughness along fracture walls (Brown, 1987). The mineralogy of the fracture zone in the host rock affects the amount of dilation that occurs. Calcites and silica precipitations tend to promote dilatancy while clays tend to minimize it (Davatzes and Hickman, 2010).

1.5.1 Calcite and silica healing in non-clay filled fractures

At pressures, temperatures, and strain rates in the shallow crust both silica and calcite tend to fail through brittle processes that involve micro-crack formation and linkage (Jaeger et al., 2007; Paterson and Wong, 2005; Davatzes and Hickman, 2010). Fault zone development associated with repeated shearing, associated brittle failure and healing by these mineral phases is shown in Figure 4. Intact host rock (Figure 4a) first undergoes micro-fracturing (Figure 4b), which eventually localizes into a rough discontinuity in the rock volume. Both micro-fracturing and slip on the rough surfaces defining the discontinuity produce dilation, increasing porosity (Figure 4c). In this example, porosity is reduced between shearing events as calcite fills the fractures and generated pores (Figure 4d). As stress is re-applied (Figure 4e) and shearing recurs calcite cement is broken,

providing evidence of new porosity generation (Figure 4f). Eventually, fracture-bounded volumes form that are free to rotate, defining a macroscopically mappable zone of connected porosity. Multiple cross-cutting cements in fault rock implies a history of porosity regenerating by recurrent fracture and porosity-loss through healing.

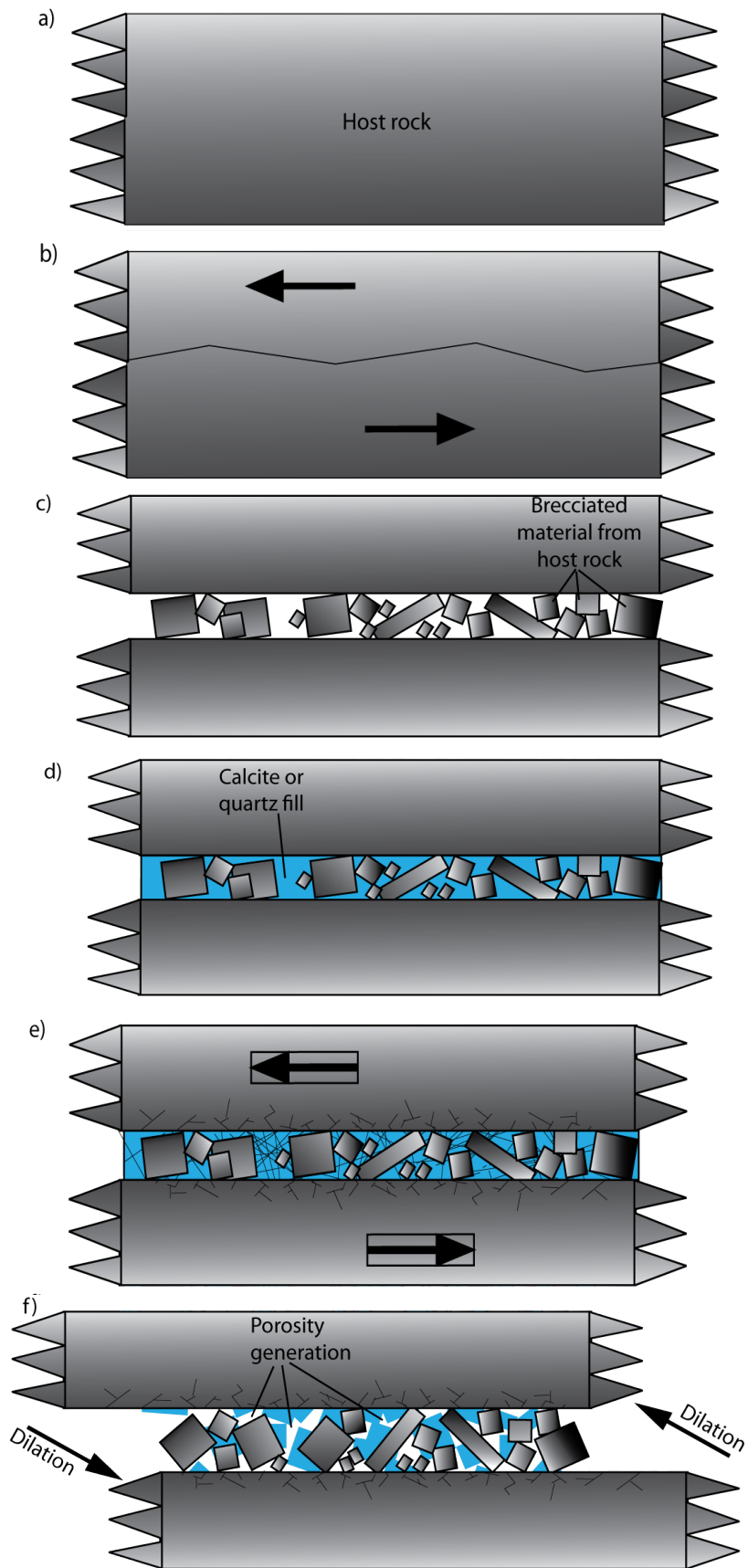


Figure 4: An idealized diagram of porosity development in calcite-healed fracture zones. Horizontal arrows represent shear movement of the host rock and diagonal arrows represent dilation.

1.5.2 Clay-lined fractures

Clay frictional coefficients range from 0.1 to 0.4, which is significantly weaker than those of cements or the quartzo-feldspathic host rocks (Lockner and Beeler, 2002). Small grain size and this weak contact strength increases the ductility of clay-rich fault rocks allowing them to flow into and plug pore space otherwise generated by slip of rough fracture walls (Figure 5). Shear tends to remain localized in the highly ductile clay-rich fault rocks, minimizing the dilation that accompanies slip if reactivated. In addition, the low strength also makes it much more likely to reactivate clay-lined fractures in preference to forming new fractures (Jaeger et al., 2007; Patterson and Wong, 2005; Davatzes and Hickman, 2010).

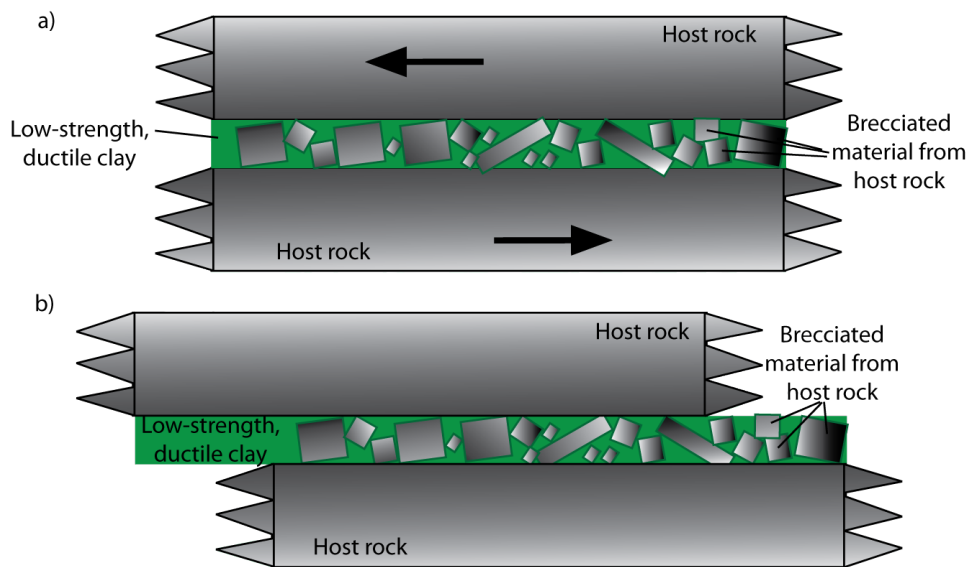


Figure 5: An idealized diagram showing how low-strength, ductile nature of the clay minimizes dilation during stress. The arrows represent shear movement.

Note that the path behavior distinguished in Figures 2 and 3 can apply to other minerals. Common hydrothermal minerals like pyrite would follow a path similar to calcite and silica/quartz. Similarly, low strength minerals such as talc, serpentine and zeolites could follow a path like that of clay enrichment.

1.6 Fracture Evolution

Because fractures tend to be reactivated, they develop through stages distinguishable by geometric characteristics. Generally, the evolution proceeds from small, single fractures that grow in aperture (width of crack) and length. As deformation increases, the fracture density increases. Once cracks are close together they interact through the distortion of the intervening intact rock causing these cracks to link and form larger discontinuities and networks of fractures. This process reduces the cohesiveness of the rock mass. Eventually fracture bounded volumes of rock form creating a zone of breccia. Throughout this evolution, the strength of rock decreases (Moore, et al., 2009). However, permeability peaks as the fracture density increases just up to the point of brecciation. After the rock loses cohesiveness, permeability decreases once again (Moore, et al., 2009) although it will

tend to be somewhat higher than the original, low porosity, crystalline host rock. In the presence of fluid flow, this process might be modified as the fresh crystalline surfaces interact with the flowing fluid. This process culminates in the formation of a distinct fault core of highly deformed, often altered rock, and a surrounding damage zone of fractured rock (Caine et al., 1996) (Figure 6).

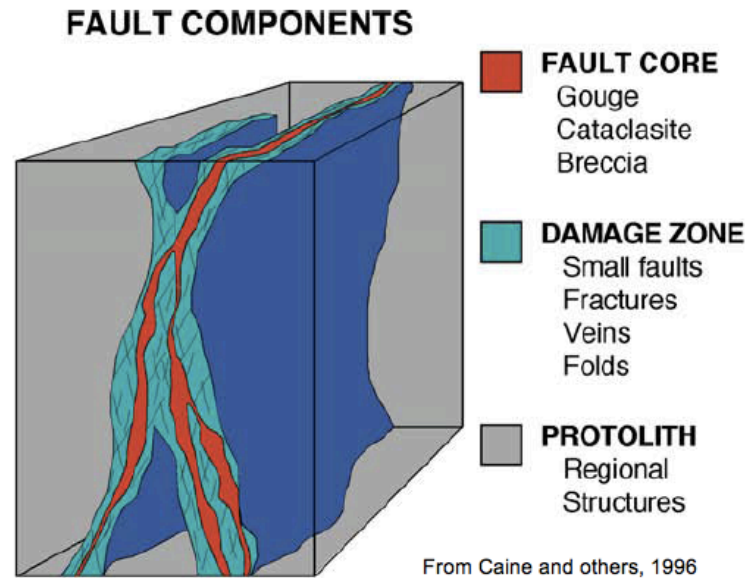


Figure 6: A conceptual model of a fault zone. The red inner fault core is highly deformed, associated with breccia and altered rock. The turquoise middle layer is less damaged and dominated by fractures and small faults. The grey outer layer is undamaged host rock (modified from Caine, et al., 1996).

In this paper, five fracture stages are defined in an attempt to categorize the evolution of a fracture system over time. The type of porosity generated by dilatancy that is measured in each of these stages implies a specific sequence of fracturing. Figure 7 is a visualization of how these concepts of time, fracture evolution, and porosity work together.

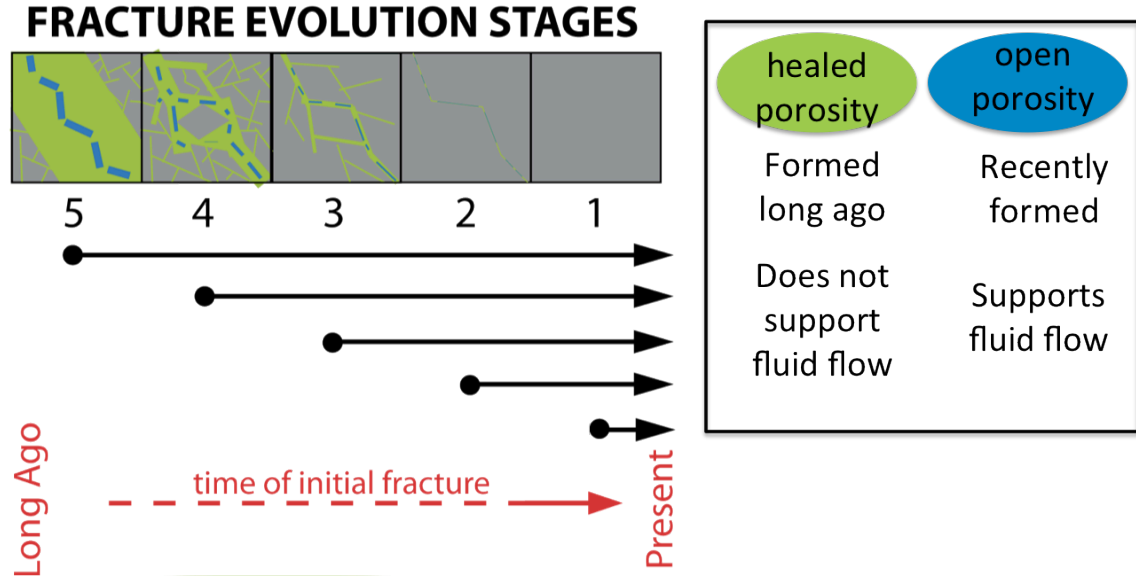


Figure 7: A schematic diagram illustrating how time relates the fracture stages and porosity types as defined in this paper.

Stage 1 represents unfractured rock, which therefore has no fracture history. Stage 5 represents the most fractured rock, implying that it has been undergoing fracturing for the longest amount of time. In other words, the initial fracture that developed into a stage 5 fracture system occurred before the initial fracture that developed a stage 4 fracture, and so on. This schematic also demonstrates how open and healed crack porosity fall into the timeline. Open porosity implies a fracture has recently occurred and has not yet been filled in. Healed crack porosity is the result of an open fracture that has, over time, been sealed with a secondary or alteration mineral. Both types of porosity may be found from stage 2 through 5, but the fractures that formed such porosity originate in different points in time.

A fracture system with only open porosity implies that it is very young. A fracture system with both open and healed crack porosity suggests an older system with both a history of shear strain as well as recently activated shear strain. A fracture system with only healed crack porosity suggests that it is old and but has no recent fracture development.

2 METHODOLOGY

The core samples used in this study were collected from the USGS core library maintained by the Energy and Geoscience Institute (EGI) of the University of Utah in Salt Lake City. The eight core samples representing fractures, as well as the corresponding hanging wall and footwall sections for each, were selected for this study based on the following criteria: 1) The core contained a fracture running through it distinct from the basaltic host rock, 2) The sample was primarily dominated by either calcite/silica precipitate that healed the fracture (Figure 8) or by clay alteration lining the fractures (Figure 9), 3) It matched the description of one of four distinct fracture evolution stages as distinguished here:

1. **Unfractured** – Cohesive basalt with no macroscopic, through-going fractures.
2. **Immature fracture** – A macroscopic structure representing a discontinuity in the rock defined by two distinct surfaces and lacking fault rock or associated macroscopic fractures.
3. **Simple fault** – A macroscopic structure with fault rock and/or vein material between the two contact surfaces which might be slickensided.
4. **Developing fault** – Macroscopic fractures forming a network of interconnecting cracks and breccia. Typically one of the suite of fractures accommodates the majority of shearing as evidenced by localized, often discontinuous fault rock development.
5. **Fault zone** – Extensive, continuous fractures with a center that is no longer clearly identifiable as fragments of host rock in hand sample forming a distinct fault core. Typically associated with a well-developed damage zone of macroscopic fractures.

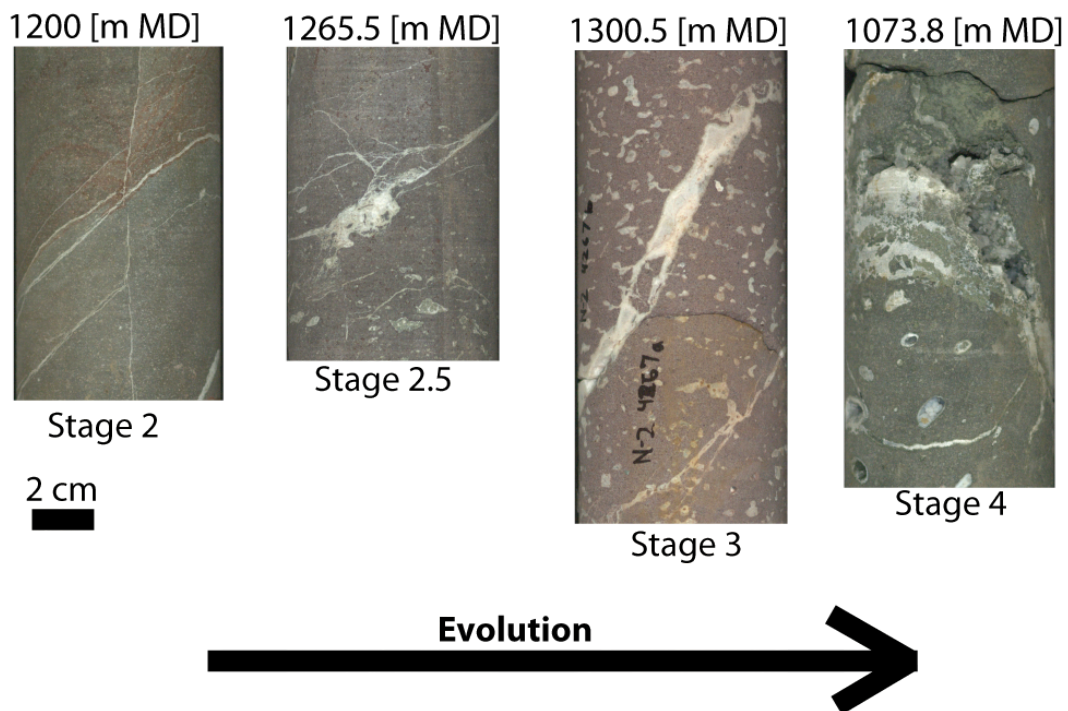


Figure 8: Progress of fracture evolution in basaltic rock dominated by calcite and quartz cementing. Samples are from Newberry Volcano well N2. Numbers along top of each sample are the depths from which the core was extracted. Note that no non-clay stage 5 example was found.

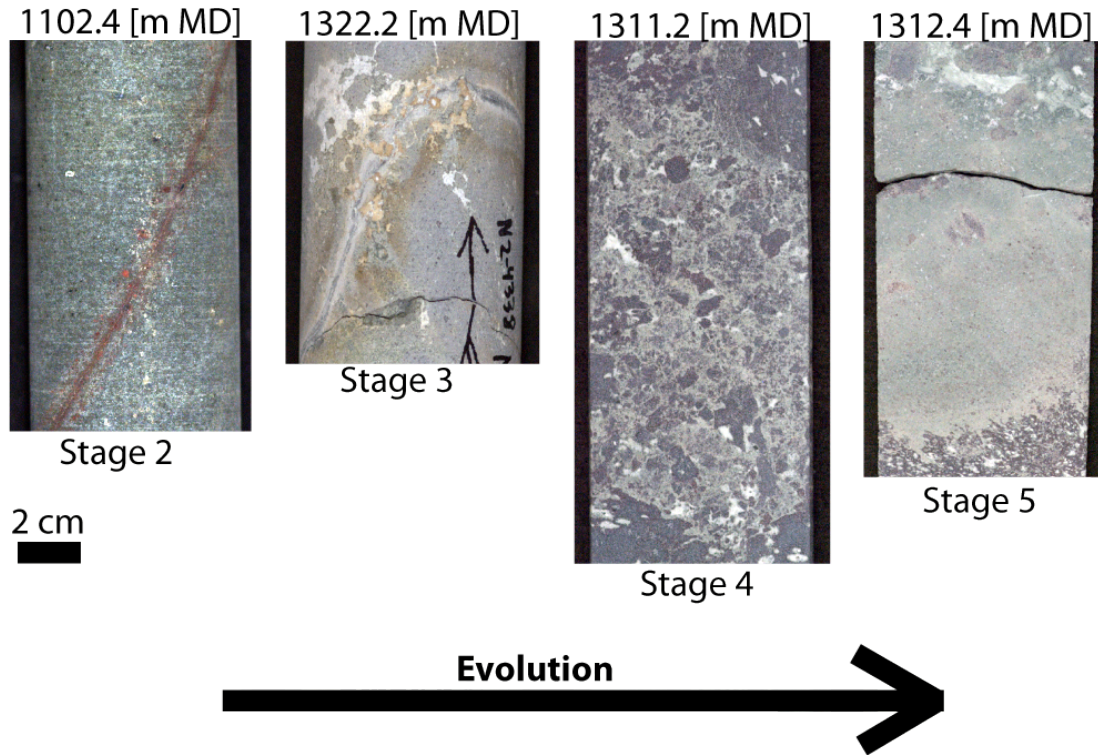


Figure 9: Progress of fracture evolution in basaltic rock dominated by clay alteration. Samples are from Newberry Volcano well N2. Numbers along top of each sample are the depths from which the core was extracted.

In this paper all work focuses on fracture stages 2-5. Table 1 lists all the core samples that were analyzed. For every core sample representing a fracture stage, the associated protolith was sampled to provide a means to measure background levels of porosity, chemistry and mineralogy. This unfractured protolith can be regarded as stage 1. In all samples, the protolith was either included in the same piece of core that held its surrogate fracture or was sampled from a separate piece of core immediately above and/or below the fractured core. The latter case specifically applied to stage 4 and 5 fractures that occupied the entire length of a single piece of core.

Originally, over 20 core pieces representing three different wells, the GEO N2, the GEO N1, and the SF NC72-03 (Figure 10), were sampled. However, for this study, only the cores from the GEO-N2 well were selected for data processing. All data in this report will come from cores spanning the depths of 3617 to 4339 feet (1102 to 1322 meters) from the surface of the well. All core from these depths has a diameter of 3 inches (7.6 centimeters).

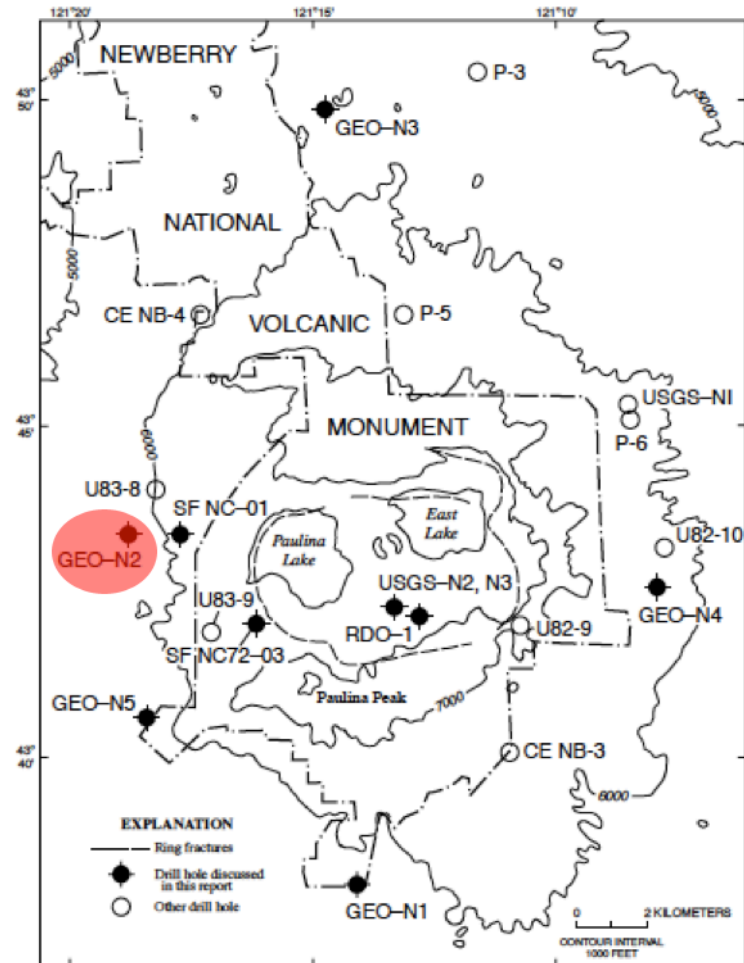


Figure 10: Map detailing the drilling wells around Newberry Volcano. The well selected for this study is highlighted in red (image modified from Bargar and Keith, 1999).

2.1 Trace Mapping

Trace maps of the cores were prepared to determine the three dimensional distribution of structures, their relative attitudes, and the related mineralogy. To accomplish the tracing, plastic transparency sheets were wrapped around the cores and surface features were mapped using a uniform color scheme. Macroscopic *primary porosity* and *secondary porosity* became distinguishable once these features were identified as were their association with discrete geologic structures.

The transparencies were then unwrapped, laid flat and digitized into computer picture files using a flatbed scanner. The digitized images were imported into Adobe Photoshop where the color-coded features could be isolated and grouped and assigned index colors. The total number of pixels of a given color relative to the total number of pixels in the scan quantified the 2-D macroscopic porosity mapped on the surface of the core. Both *open porosity* and *healed crack porosity* were quantified using this technique. All features contributing to open porosity were mapped as blue, and all features contributing to healed crack porosity were mapped as green. Along a transect across each core that ensured representation of the host rock and the fracture (including any fault rock), a 2-cm wide

strip of this surface map was isolated to measure variation in macroscopic porosity as a function of position relative to the fracture.

2.1.1 Macroscopic porosity measurement

Open (mapped as blue) and healed porosity (green) were measured as the percentage of total area covered within the maps. To capture spatial variation in porosity and to allow comparison among cores and structures of different lengths, sub-areas of each map were defined in which to make this calculation. This measurement was repeated in overlapping 2 cm x 2 cm squares distributed in 1 cm increments along a transect to provide representative measurements of porosity variation associated with the fracture zone, the damage zone immediately surrounding it and the background host rock.

A 2 cm x 2 cm sides of these squares are greater than approximately ten times the grain size and several times the size of vugs in the core to ensure representative, repeated estimates of the two-dimensional porosity. The fractures themselves are significantly larger, and thus this resolution still allows mapping of variations in porosity that can be attributed to these structures by the distance of the porosity measurement from the fracture. In addition, given that the average length of each piece of core being measured was roughly 30 cm, this provided both a balance in the number of measurements between the practicality necessary to complete the study and a sufficient number of observations to satisfy statistical significance.

However it is important to realize that the porosity measured is an average of the 2 cm x 2 cm area, and the porosity of individual structures can be lower or high than this average. For instance both vugs and fractures can represent 100% porosities at lengths scales smaller than these features if they are completely open. These percentages were plotted and show porosity as a function of distance from the center of the primary fracture on the core, where positive distances correspond to increasing depth below the primary fracture.

Since the same procedure was applied to all cores, these porosities are comparable for the purpose of evaluating the evolution of porosity with increasing structural complexity and across both systems of faults, non-clay versus clay-dominated healing and alteration. Two limitations of this data set are critical to recognize: (1) these represent only macroscopic porosities greater than approximately 0.5 mm and thus neglect smaller pores which are documented by the thin sections; (2) these are 2-D estimates of porosity. Furthermore, the porosity measures in themselves do not distinguish the connectedness of this pore space or the tortuosity (length of connected path divided by the straight-line length between two points) critical to correlating porosity to permeability. Given that these maps are two-dimensional this would only be an approximation in any case, but within this limitation, the basic parameters could be evaluated from the existing maps.

2.2 Petrographic Microscope Analysis of Representative Thin Sections

Pore sizes exist across a range of length-scales, many of which cannot be measured using the naked eye. This is true of the Newberry core. This microscopic porosity must be measured using petrographic microscope analysis. To obtain thin sections representative of the features of interest, as well as of each core as a whole:

1. Each core was cut lengthwise into three parallel slabs. One slab was archived, one slab was saved for porosity measurements in future studies and a final slab (the center piece) was designated for thin section production.
2. Portions of the core slab representing the protolith, damage zone, and primary fracture were designated for production of 20 mm x 30 mm thin sections. Specific structures of interest included fractures, vugs, and zones of representative host rock not affected by fracture or alteration.
3. The 20 mm x 30 mm blocks were cut out using a tile saw and sent to National Petrographic Service, Inc in Texas for final cutting, mounting, and polishing. The samples were injected with blue-dyed epoxy to fill any open pore space and make them readily amenable to image analysis.

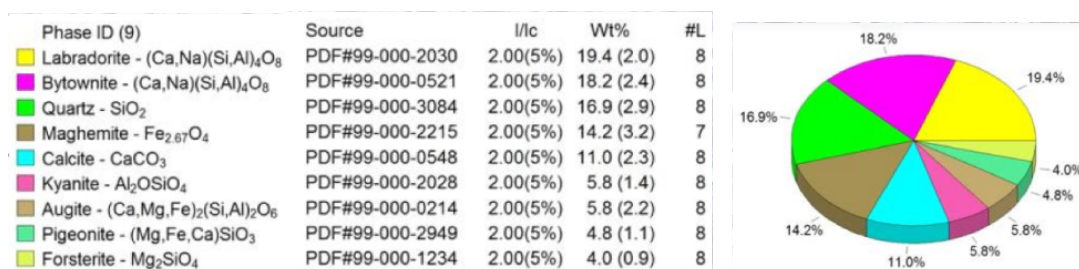
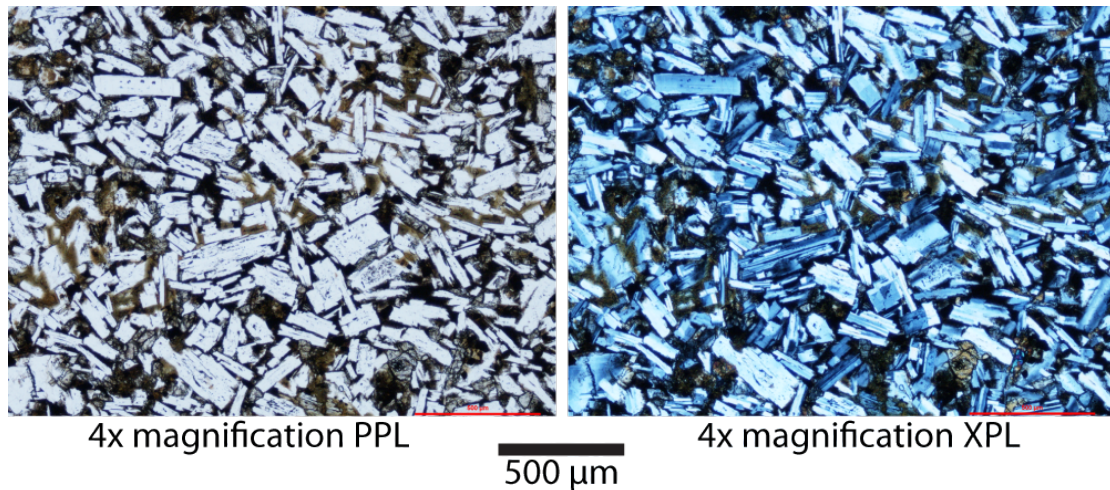
2.2.1 Microscopic porosity measurement

The key to identifying microscopic porosity was identifying area in the thin section that was not occupied by original host rock or by host rock that was replaced by alteration minerals. Porosity in this paper is defined as new volume generated within the protolith through fracturing or dissolution of original rock forming minerals (secondary) or as open space remaining from the original formation of the rock (primary).

The thin sections were magnified 4 times on a Nikon Eclipse LV 10 petrographic microscope with a high resolution digital camera attachment. Using the software program NIS Elements, the digital camera took pictures of the thin section under magnification at a 2560x1920 pixel resolution and show approximately 2 mm x 2.5 mm of the thin section. Every picture taken was photographed in both plane-polarized light and crossed-polarized light. Also, every picture was taken in the correct orientation so that the top of the photograph was true to the up-well direction of every core sample. Using a thin section mount, the thin section was moved in roughly 1 mm increments across the microscope stage and a picture was taken at every increment. The resulting photomosaics define transects that crossed the major fractures in each sample. Some samples had individual fractures or fracture-rich zones that were wider than a single thin section. In these cases the thin section was chosen to encompass the border between the fracture zone and the adjacent damage zone, and the transect of digital photographs captured as such. In some samples, single photographs were taken of the hanging wall and footwall thin sections to portray the mineralogy and background porosity of the host rock.

Once the photographs were obtained, they were stitched together into long vertical (and in the one sample, horizontal) strips digitally using Adobe Photoshop. Once the strips were created, open porosity created by vugs or fractures was identified by any blue-dyed epoxy present in the plane polarized light pictures. Healed crack porosity was mapped as any area within the thin section strip that was not host rock, altered host rock or open porosity.

To create a consistent method of identifying healed crack porosity in thin section, the protolith rock was identified in each sample. All samples exhibited a fine-grained texture containing abundant mafic minerals consistent with massive basalt, massive andesite and vesicular andesite. Key minerals identified included plagioclase, quartz, pyroxene, and traces of oxide minerals like magnetite and hematite. The most recognizable identifier of the mafic host rock was the prominent plagioclase grains with characteristic albite twinning (Figure 11).



Clay Stage 2 Protolith Footwall

Depth: 3617 feet/1102.4 meters

Figure 11: Protolith footwall from the clay stage 2 fracture and associated XRD analysis. A typical example of the fine-grained mafic host rock found in all samples measured. Note the prominent plagioclase grains in thin section.

If minerals in the host rock were replaced with an alteration mineral but the outline of the grain remained the same, this was not considered porosity generation. Snaking pathways of secondary minerals that cut through the host rock and left no trace of protolith mineral grains were generally counted as healed crack porosity. In Figure 12, the calcite sample has porosity generation that is easily distinguishable from the host rock. The clay sample's generated porosity is more difficult to distinguish.

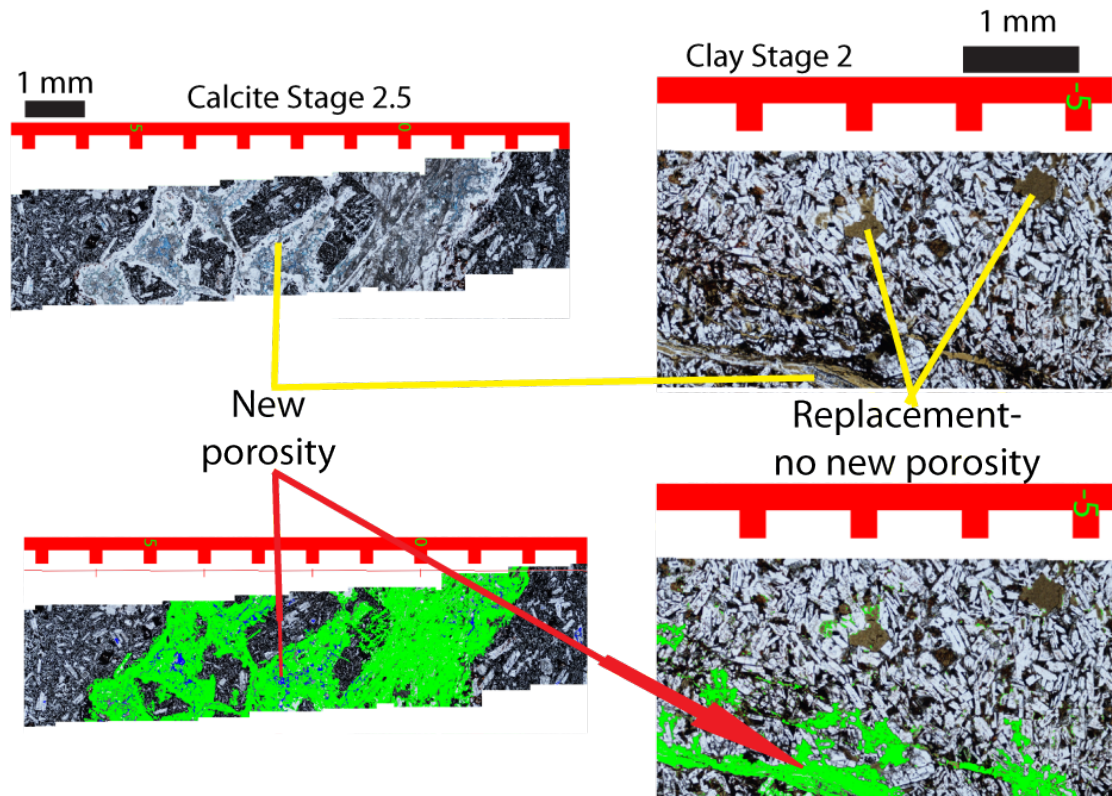


Figure 12: Two examples of thin sections that represent the decision making in highlighting healed crack porosity. Note: Images have been rotated 90° clockwise from the normally vertical orientation. Each red tickmark represents 1 mm.

These constraints define the microscopic healed crack porosity as any pore space, either originating from the rock's formation or created by dilation during fracturing, that was filled in by secondary minerals. To be consistent with the macroscopic porosity analysis, the open porosity was colored blue and the healed crack porosity was colored green.

Similar to the macroscopic porosity analysis, the 2.5 mm-wide photographic strips of thin section were broken down into overlapping individual squares measuring 2 x 2 mm. This box was sufficiently large to contain many mineral grains and produce repeatable porosity values in the host rock excluding regions with vugs, and thus defining a representative area from which to identify departures in porosity due to secondary porosity development. Each square was spaced 1 mm apart. Again, the percentage of green and blue surface area of each square divided by the total surface area of each square represented the percentage of healed crack porosity and open porosity, respectively. These percentages were then plotted on a two-dimension chart with porosity as a function of distance from the center of the fracture being mapped. This approach is essentially subject to the same 2-D assumptions as the macroscopic porosity mapping as are the potential implications of this measurement for permeability.

2.3 XRF Analysis

In addition to measurements of porosity, the cores were measured for their elemental signatures as a function of distance along the length of the core using x-ray fluorescence.

To achieve this, a hand-held Thermo Scientific Niton xl3t XRF analyzer was used. This analyzer operates on unprepared core surfaces, and in the presence of helium effectively measures elemental concentration upwards of a few tens of ppm from phosphorous through lead and also including thorium and uranium. The elemental composition measured was an average of a 1 cm x 1 cm area. Multiple measurements distributed in 1 cm steps were measured across the core parallel to the core axis for its entire length to define transects comparable to macroscopic porosity analysis.

2.4 XRD Analysis

In addition to determining the mineralogy of the thin sections using petrographic analysis, x-ray diffraction analysis was applied to corresponding representative portions of the same core slab used for thin section production. The following steps were applied to all samples:

1. ~1 cm³ cubes of core slab were cut out from the remaining rock directly adjacent to each thin section cutout.
2. The cubes from each sample were crushed 30 seconds to 1 minute of time into a fine powder with a rock-crushing machine.
3. The powder from each sample was sieved through a 500 micron mesh to eliminate large particle sizes.
4. The powder from each sample was further crushed for 3 minutes in a McCrone micronizing mill to guarantee a particle size of 5-10 microns.
5. The powder from each sample was pressed at a pressure of 4000 lbs (1814.4 kg) into a stainless steel ring.
6. Each sample-containing ring was run through the Temple University Rigaku D-Max B X-ray Diffractometer for crystallographic structure analysis.
7. The data was processed using the JADE software, with Reitveld Refinement module and a library of over 200,000 mineral x-ray diffraction patterns and lattice characteristics parameters in the MDI minerals database.

The XRD analysis provided relative weight percentages of minerals present within the bulk sample specifically chosen to be adjacent to the thin sections examined and containing the same salient features. The change in each mineral's weight percentage in the fracture relative to the host rock was calculated as:

$$\% \Delta \text{wt}(\text{mineral}) = \frac{\% \text{wt}(\text{mineral_in_fracture_zone}) - \% \text{wt}(\text{mineral_in_host_rock})}{\% \text{wt}(\text{mineral_in_host_rock})}$$

The formula gives a positive number for a relative increase in the mineral and a negative number for a relative decrease in the mineral.

In some fracture stages, there were multiple XRD samples representing multiple thin sections. In addition, XRD samples were run on both the hanging wall and footwall protolith sections for some fracture zones (i.e., host rocks from both sides of the fault) and thus representing the complete range of minerals that might have been mechanically incorporated into fault rock within the fracture. As a result, some fracture stages have multiple XRD results to choose from for its fracture zone and host rock zone.

The most representative sample for each stage's fracture zone and host rock were chosen by applying the following criteria: The fracture zone rock was designated by the XRD sample taken adjacent to the thin section used for that fracture stage's microscopic porosity analysis. The host rock was designated by the XRD sample chosen from the protolith exhibiting the least amount of alteration. The least amount of alteration defined visually as the hanging-wall or footwall protolith with the least amount of mineral-filled vugs, hairline fractures, or discoloration by alteration. The host rock was always within two feet (0.6 meters) of a fracture zone.

3 RESULTS

The main goal in analyzing the data generated by the four methods described above is threefold. (1) To quantify trends in porosity over distance from fracture zone, as well as to find any patterns associated between porosity and mineralogy distribution evident from single core. (2) From the comparison of core representing increasing structural development map the ability of fractures to continue to regenerate porosity if the fracture is reactivated. (3) Determine the effects of mineralogy on the potential for porosity regeneration. To accomplish this, four critical types of data are evaluated in this section:

1. Mineralogy end member groups; clay-dominated vs. non-clay fracture zones
2. Fracture stages; divided into stages 2, 2.5, 3 and 4 for non-clay fracture zones and stages 2, 3, 4, 5 for clay-dominated fracture zones
3. Types of porosity; open porosity, which is any open-air pore space, healed fracture porosity, which is any open pore space that has filled in by secondary minerals, and skeletal porosity, which is the sum of open air and healed fracture porosity
4. Scale of measurement; microscopic scale, performed on a millimeter scale on thin sections under petrographic microscope, and macroscopic scale, done on a centimeter scale in hand sample.

3.1 Macroscopic Porosity Results

3.1.1 Photos and maps of macroscopic structures and related healing and porosity characteristics

In figure 8, four examples of fractures in core from well N-2 illustrate the evolution of a non-clay fracture system. In the following figures, each stage is individually analyzed through transparency mapping to label distinct characteristics of each fracture stage. The color and labelling scheme in Figure 13 applies to all transparency maps. The natural, healed fractures in some of the samples were cross-cut by open fractures. Since these open fractures are nearly perfectly preserved and not mineralized they are most likely caused by handling post-coring. Any post-coring handling fractures found in the following samples will be identified as such.

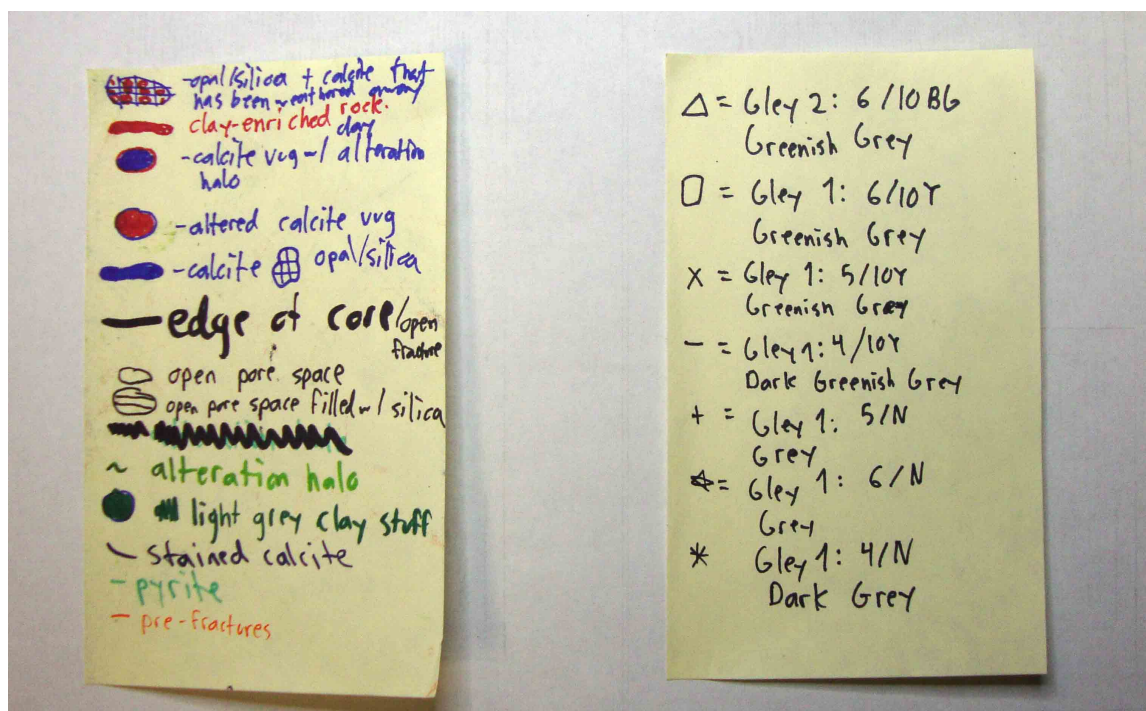


Figure 13: The colors used in identifying different minerals and surface features are shown on the left. On the right is the symbology for the associated Munsell color chart labels used to identify the color of the core's basaltic host rock.

Non-clay stage 2 (Figure 14) exhibits multiple 1-2 mm wide immature fractures with normals that are at $\sim 45^\circ$ angles from core axis in non-vesiculated andesite. Calcite and quartz have healed the fractures. The thickest of these fractures bisects a nearly vertical fracture running along the length of the core. Some of the smaller fractures at the 45° angle terminate at this vertical fracture, suggesting they are younger. The main fracture also separates unaltered host rock below the fracture from a slightly discoloured and altered host rock from above the fracture, suggesting that the fracture acts either as a barrier to fluid flow or a highly permeable drainage conduit from which fluids infiltrated the host rock. Given that the discoloration occurs on only one side of the fracture, it is most likely it acted as a barrier or baffle to flow across the fracture. The discoloration is also most intense at the fracture and decreases at larger distance from the fracture suggesting that either the fluid interacted with the minerals in the fracture or that increased time in this region do to restricted flow enhanced mineralization. These fractures have simple planar geometries, lack fault rock and have not interacted to fully isolate protolithic blocks and allow their rotation characteristic of breccia. Thus, this sample exemplifies a relatively young fracture system with limited amounts of re-fracture.



Figure 14: Non-clay stage 2 transparency map and panoramic core photo. The arrows in both photos point upwell. Brown tickmarks on transparency photo equal 1 cm.

Non-clay stage 2.5 (Figure 15) is an intermediate stage because it exhibits regions of simple planar fracture, but also shows fracture interaction and linkage that produce a fracture network and localized large open spaces thus has characteristics of both stage 2 and stage 3. The main fracture normal is angled at $\sim 45^\circ$ to the core axis. It and a few branching fractures are immature, with 1-2 mm of thickness and two distinct surfaces. However, the main fracture also exhibits a zone of thickening to roughly 1 cm of thickness with inclusions of host rock incorporated within the cementing mineral (mostly calcite). Together, the fracture system isolates volumes of the protolith as an incipient stage of breccia formation and damage zone development. Similar cements in these fractures suggest they were open at the same time and thus operated as an interacting system. Its protolith is massive andesite above the fracture and vesiculated andesite below the fracture.

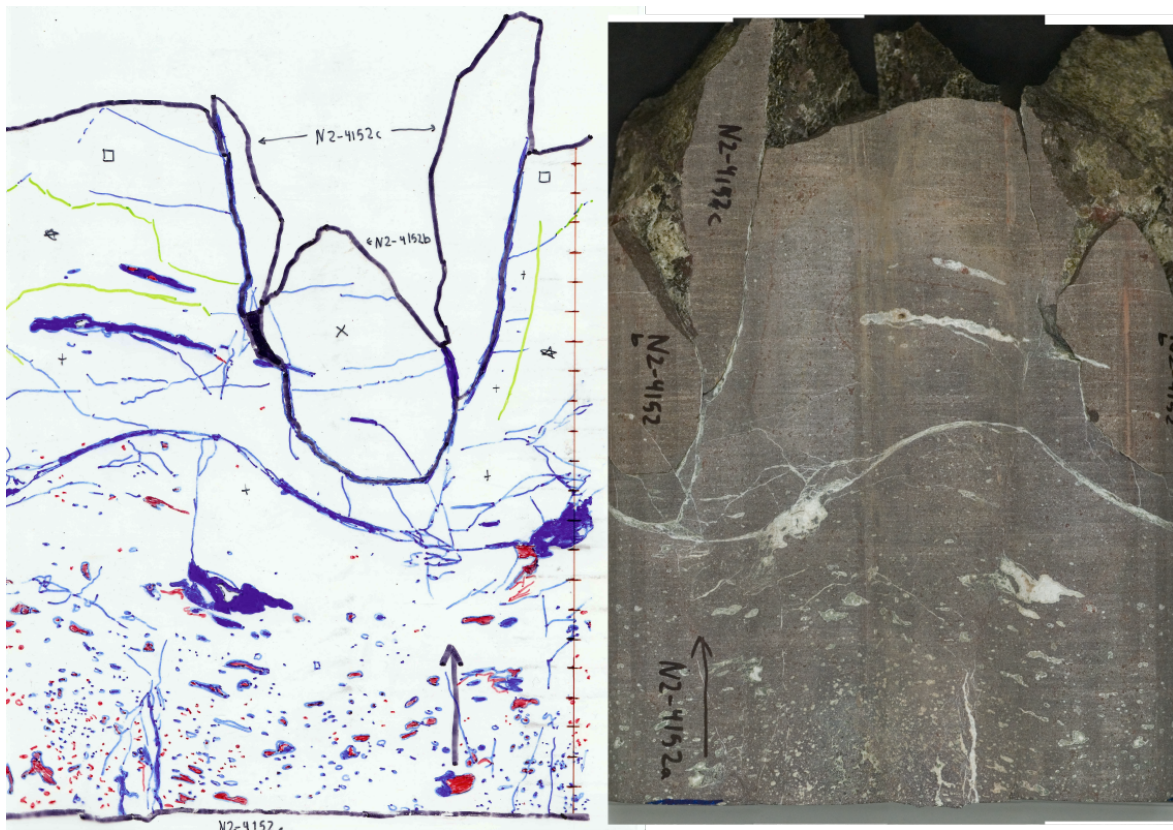


Figure 15: Non-clay stage 2.5 transparency map and panoramic core photo. The arrows in both photos point up well. Brown tickmarks on transparency photo equal 1 cm.

Non-clay stage 3 (Figure 16) has a developed a mature fracture with isolated volumes of host rock incorporated into the fracture cement that show translation and rotation from their original positions. Multiple layers of a mixture of quartz and calcite cements are consistent with repeated opening. The fracture normal is oriented at an angle of $\sim 60^\circ$ to the core axis. The fracture resides in a highly vesiculated andesite protolith. The vugs are also filled with quartz and calcite. Quartz primarily lines the center of the main fracture while calcite lines both surfaces of the fractures suggesting the calcite formed prior to the quartz. This, along with the inclusion of host rock in the fracture, suggests multiple fracturing and healing events. This sample has an open, post-coring handling fracture along the main calcite-filled fracture.

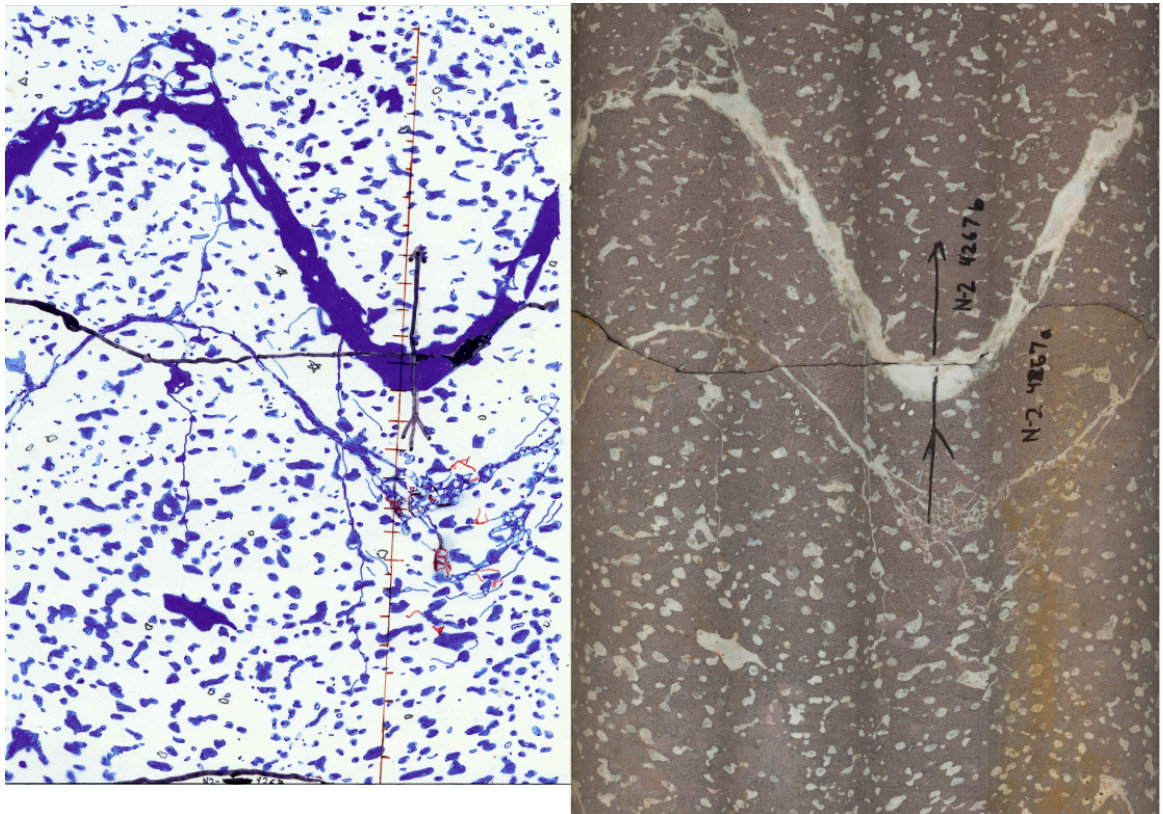


Figure 16: Non-clay stage 3 transparency map and panoramic core photo. The arrows in both photos point up well. Brown tickmarks on transparency photo equal 1 cm.

Non-clay stage 4 (Figure 17) is characterized by an extensive network of open, partially healed, and healed fractures with discontinuous fault rock. The host rock is a vesiculated andesite. The quartz and calcite-lined fracture is over 5 cm wide at its thickest point although its thickness is highly heterogeneous. Unlike stages 2 and 2.5 it is not bounded by relatively planar, sharp fracture surfaces. It is the only non-clay example to exhibit macroscopic open porosity. Multiple fracture-bounded volumes of host rock enveloped by several layers of calcite demonstrate repeated fracturing and rotation within the zone of breccia. The open porosity suggests that repeated fracturing outpaced healing by mineral precipitation. Curing sample collection at the sample fractured just above the main calcite and quartz-lined portion of the fracture.

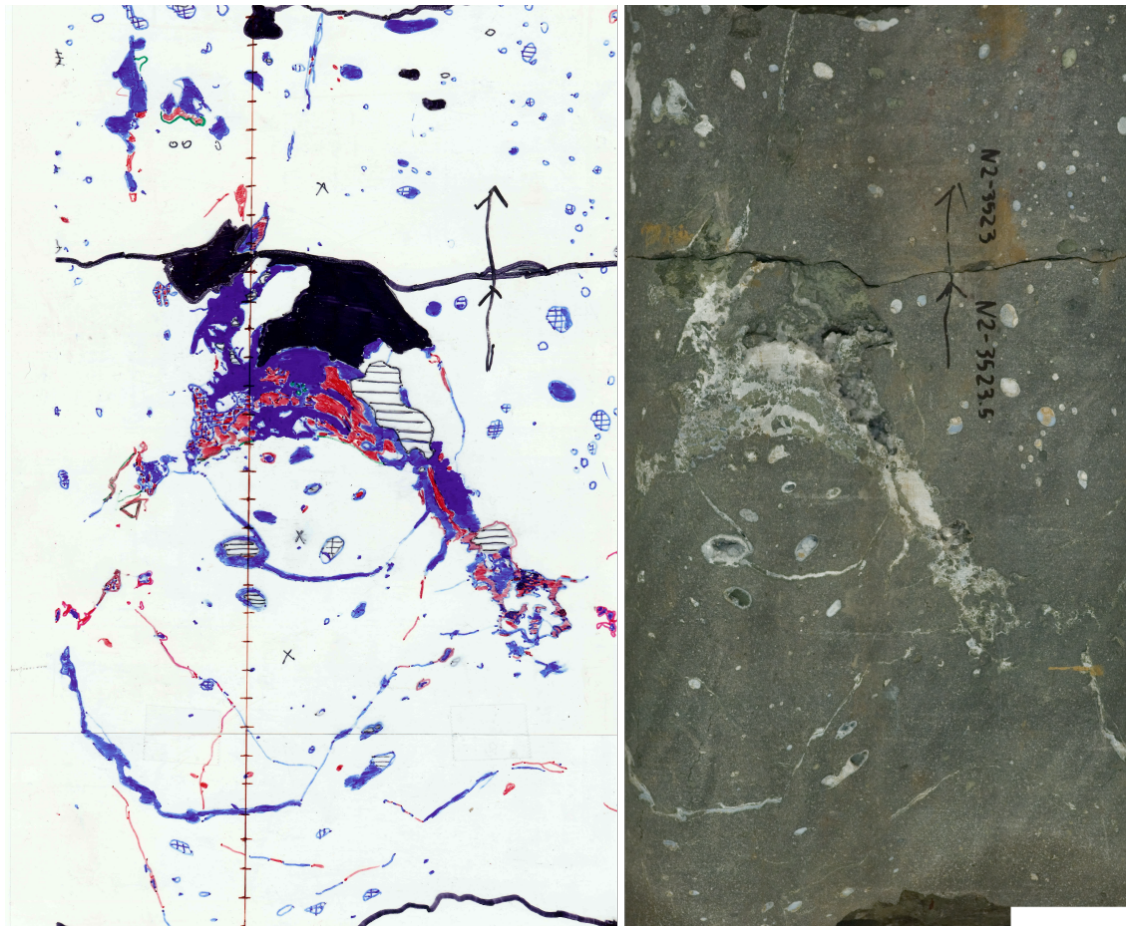


Figure 17: Non-clay stage 4 transparency map and panoramic core photo. The arrows in both photos point up well. Brown tickmarks on transparency photo equal 1 cm.

No stage 5 example of a non-clay fracture system was found within the 1000 feet (305 meters) of continuous core from N2 well that was examined, or from the 2000 feet (610 meters) of continuous core examined from the N1 and NC-72-03 wells. This is consistent with the low-permeability of the Newberry Volcano geothermal field evidenced to date by the inability to successfully drill into high permeability rock amongst 18 boreholes in the caldera and surrounding volcanic edifice, as well as a general lack of surface hot springs (only one is known and occurs in the caldera).

Figure 9 shows examples of fractures that outline the evolution of the clay-lined fractures. Clay stage 2 (Figure 18) has a very immature main fracture with two sharply defined surfaces lined by roughly 1 mm of iron-rich minerals like maghemite, according to the XRD results. The host rock is basalt. The fracture normal oriented $\sim 60^\circ$ from core axis. There are some thinner fractures that branch from it at the lowest point in the sinusoidal curve around the circumference of the core. The distinct contact surfaces on either side of the fracture and limited branching of fractures suggest they formed in as little as one event. Much like the non-clay stage two, this fracture is associated with discoloration of the surrounding protolith. Unlike, the previous example in the non-clay stage 2, this example alteration of the protolith associated with this example is symmetric. Given that both the fracture filling and the host rock appear to share similar mineral filling, i.e., reddish, oxidized iron-rich mineralization, this symmetry suggests that prior to mineralization the fracture was a preferred fluid conduit and that fluids diffused through the fracture walls into the host rock leading to a chemical alteration. This interpretation is also consistent with the oxidizing nature of such fluids indicated by the red colouring suggesting penetration oxygen-rich fluids from shallow depths to nearly 1 km. Note that penetration of such fluids from the fracture into the wall rock over a narrow zone suggests some background permeability and porosity at least in the vicinity of the fracture. The narrow zone of alteration is also consistent with either very low permeability or spatially limited permeability and limited fluid flow. Since the fracture is currently fully mineralized with no clear evidence of multiple mineralizations, this suggests that the porosity and permeability of the fracture is associated with its initial formation and was not a long-lived or recurrent characteristic.

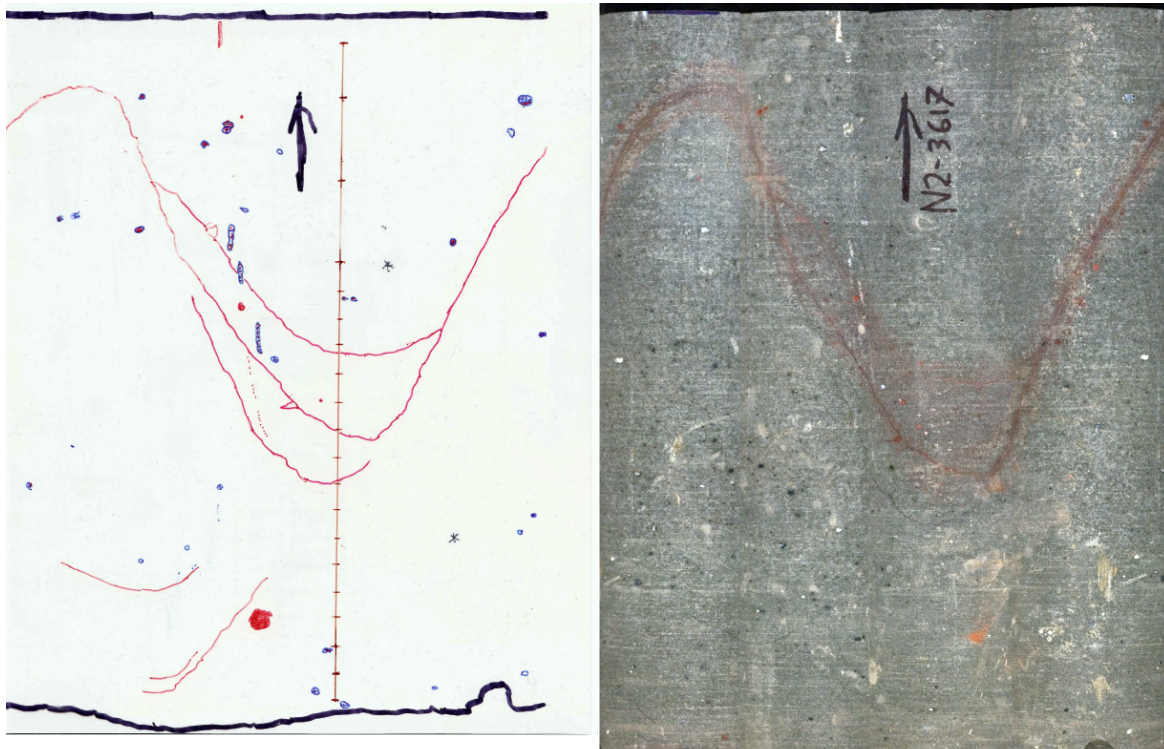


Figure 18: Clay stage 2 transparency map and panoramic core photo. The arrows in both photos point up well. Brown tickmarks on transparency photo equal 1 cm.

Clay stage 3 (Figure 19) has a mature fracture incorporating some small volumes of host rock near the top of its sinusoidal trace but still retains large portions defined by sharp fracture surfaces. At its thickest the fracture is roughly 1 cm wide and its normal is oriented at $\sim 55^\circ$ to the core axis. The host rock is basalt. Along with the clay lining, the mineral filling also contains some discontinuous calcite, making this sample's fracture-filling cement a bi-modal system. Also noteworthy is the thickness of the clay-filled fracture increasing to 1 cm wide near the zones of calcite, and reducing to 0.25 cm in zones of pure clay. The presence of the calcite is associated with increased dilatancy and porosity generation as demonstrated in Figure 4. This is especially apparent in the calcite, which occurs off the main fracture trace. Conversely, the zones composed solely of clay are the flattest and thinnest portions of the fracture, suggesting an associate of clay and the minimization of dilation during slip (consistent with the conceptual model of Figure 5).

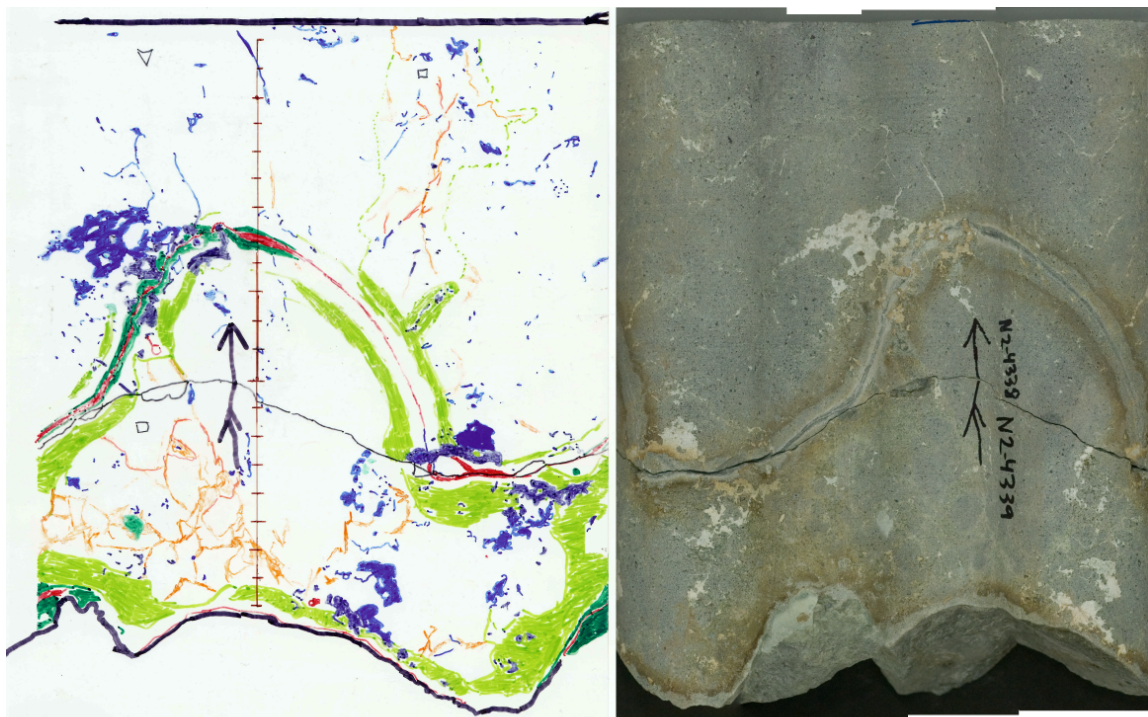


Figure 19: Clay stage 3 transparency map and panoramic core photo. The arrows in both photos point up well. Brown tickmarks on transparency photo equal 1 cm.

The fracture of clay stage 3 is filled with mostly chlorite, illite and kyanite in descending order of weight percentage as shown by bulk XRD analysis. However, the clay tended to swell heavily when exposed to water, suggesting the presence of smectite-group clay (finer distinctions would require clay-separate XRD analyses which were precluded by time constraints). Surrounding the fracture is a region in which the protolith is discoloured symmetrically about the fracture zone suggesting alteration as in clay stage 2. An open handling fracture bisects the very weak clay-filled fault.

Clay Stage 4 (Figure 20) demonstrates an advanced fracture with a well-developed breccia zone. Primarily clay fills the spaces between breccia clasts and along the margins of the zone. Some calcite is also locally developed along the edges of individual breccias clasts. Some breccia clasts show minor alteration along their rims suggesting their alteration has contributed to formation of the fault rock, which is also consistent with the matrix support of the clasts. The fracture zone is about 12 cm wide and is so irregular that there is no discernable attitude to fracture at the scale of the core. The protolith clasts have been rotated, indicating large shear strains and foliation and complex layer of cement in the matrix suggest many periods of fracturing and healing. The ratio of calcite to clay in this fracture system appears to be smaller than in clay stage 3, suggesting that while calcite continues to play a role in this type of fault, that role diminishes with increasing fault development. Further studies quantifying the exact ratio using the mineralogy maps shown in figures 14-21 but not presented here could address this issue and should be pursued.

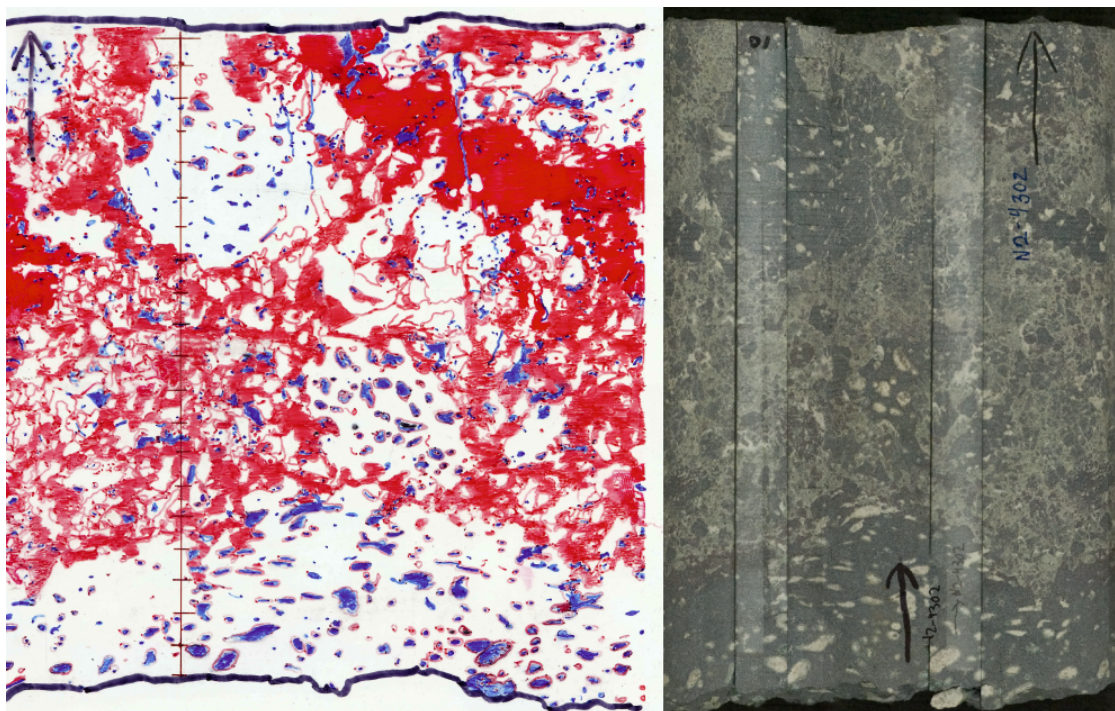


Figure 20: Clay stage 4 transparency map and panoramic core photo. The panoramic photo of the rock core is slightly distorted because the core was cut before the picture was taken. The arrows in both photos point up well. Brown tickmarks on transparency photo equal 1 cm.

Clay stage 5 (Figure 21) demonstrates the most advanced state of fracture development. The center of the fracture contains volumes of host rock so altered and ground so small that it has become a continuous layer of fault rock, an entirely distinct rock unit within the core of the fault. There is some less altered breccia above the gouge but below the gouge the rock quickly transitions into damaged but unbrecciated host rock. During handling, the core broke along the interior of the clay gouge along a surface that showed slickensides. This reveals the presence of cohesive, but very weak slip surface within the gouge zone that are roughly parallel to the irregular margins of the fault core. This advanced stage of fracture development is characterized by a distinct fault core comprised of fault rock and a damage zone in which breccia and intense fracturing are enhanced surrounding the core.

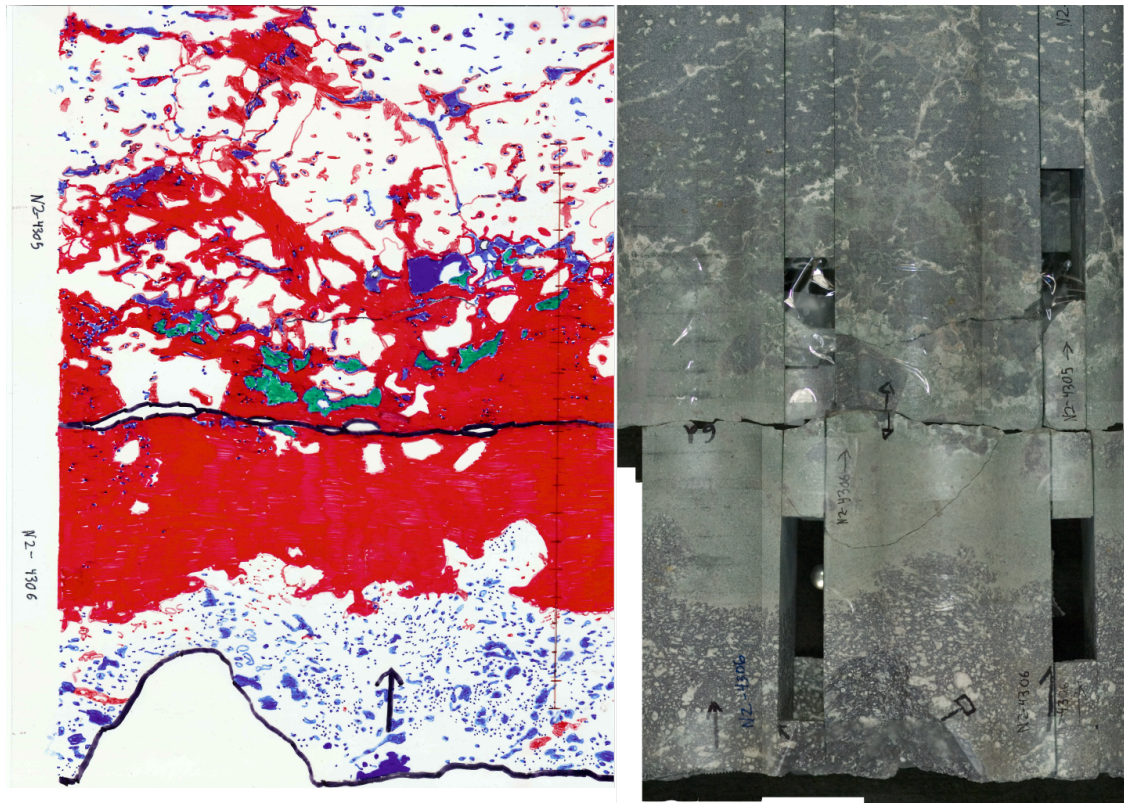


Figure 21: Clay stage 5 transparency map and panoramic core photo. The panoramic photo of the rock core is distorted because the core was cut before the picture was taken. The arrows in both photos point up well. Brown tickmarks on transparency photo equal 1 cm.

There is a lack of any discernable calcite or quartz in the gouge zone and a small amount of calcite and/or quartz in the breccia system above the gouge. However, the relative age of the calcite relative to the clay gouge is uncertain, so it is not possible to determine whether this is a relic feature one concurrent with the clay-gouge. Nevertheless, the comparison of stages 3, 4, and 5 suggest a natural progression of the bi-modal system in which clay eventually replaces calcite in the most advanced zone of fracture evolution, i.e the zone with the most slip, as the fracture progresses through stage 5.

The porosity maps of these fractures are shown in figures 22 and 23. These maps demonstrate the widening of the both the non-clay (Figure 22) and clay (Figure 23) fracture systems as they advance through each stage, from less than 1 cm wide in stage 2 to more than 5 cm wide by stages 4 and 5. They also suggest that the porosity increases are sporadically distributed in initial stages and become far more continuous with continued fracture development. More advanced stages in both cases show clear evidence of multiple reactivations absent in the simplest cases and larger strains and chemical/mineralogical change from the host rock. The maps show limited amounts of open porosity, defined as blue areas, in either fracture group with the exception of non-clay stage 4. The widening of the fracture zone in the non-clay group is attributed to the dilation process demonstrated in Figure 4 as volume must be added to accommodate the precipitation of calcite, and there is little or no evidence for large dissolution as a means of making space for the calcite or quartz.

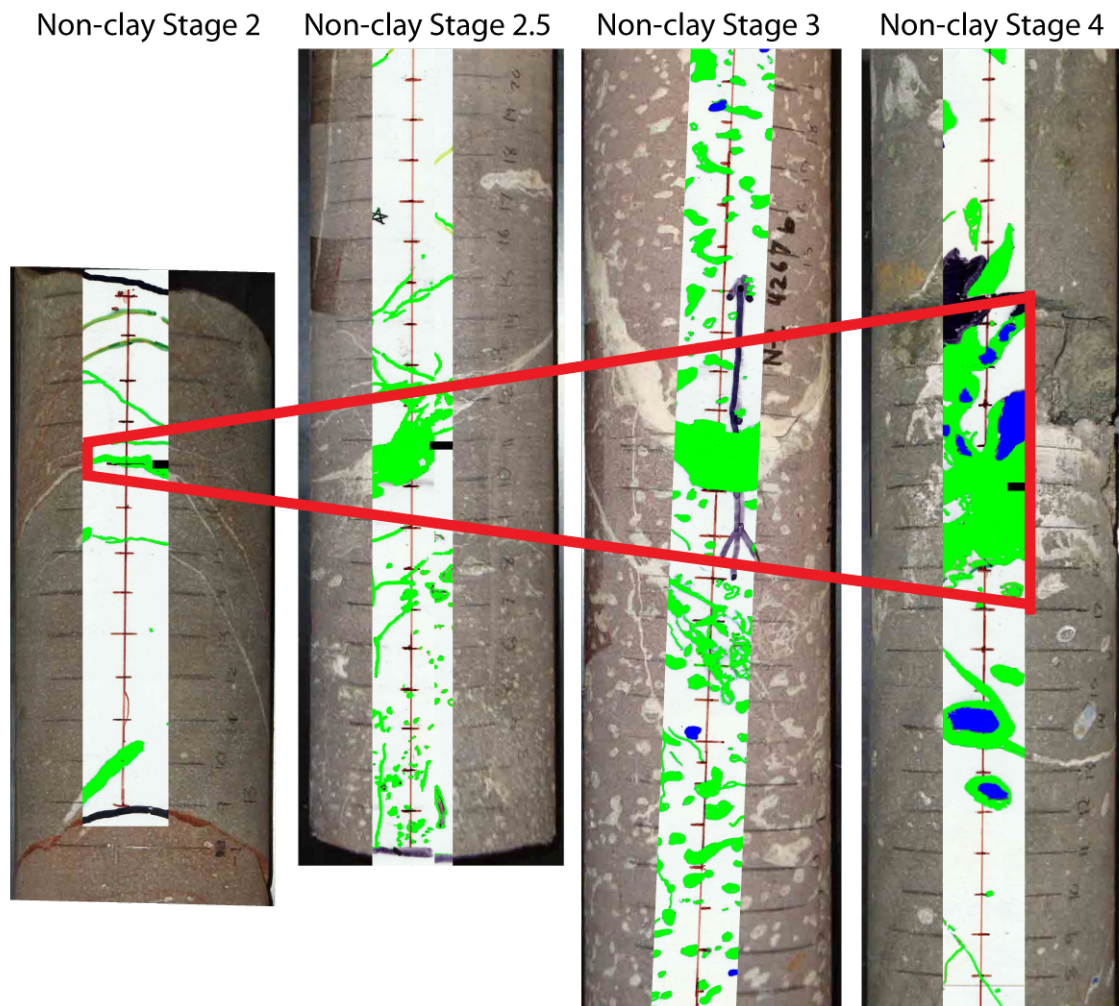


Figure 22: Macroscopic porosity mapping of the non-clay stages via 2 cm-wide transect of cores. The red polygon outlines the width of the main fracture in each stage. Green solid color denotes healed crack porosity, and solid blue represents open porosity. The arrows in all photos point up well. Brown tickmarks on transparency photo equal 1 cm.

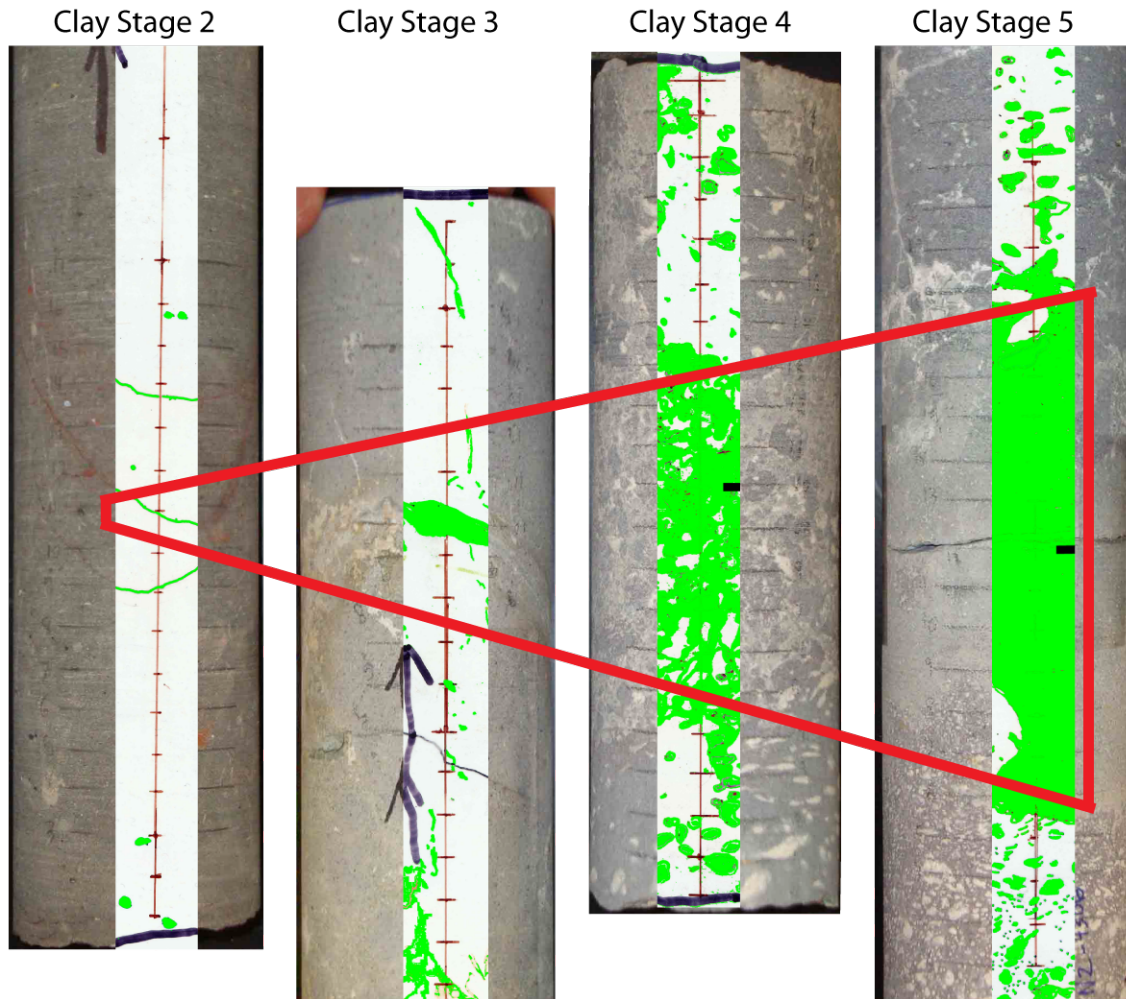


Figure 23: Macroscopic porosity mapping of the clay stages via 2 cm-wide transect of cores. The red polygon outlines the width of the main fracture in each stage. Green solid color denotes healed crack porosity, and blue represents open porosity. The arrows in all photos point up well. Brown tickmarks on transparency photo equal 1 cm.

The process behind the widening of the clay system seems to employ both dilation and mineral replacement. In early stages dilation and related fluid flow are clearly evident from fracture filling including calcite and alteration of the surrounding host rock. At later stages, in-place alteration, and dissolution and replacement clearly continues to play a role, but dilatant regions within the fault rock are not clearly discernable as in earlier stages (3-4) in which rotation of breccia clasts and associated calcite precipitation provided a mechanism for dilatancy. In fact, stage 3 suggested minimal dilation of the fracture walls in locations filled with clays. Both mechanisms add pore space to allow the formation of new mineral phases however, the continuity of such pore space is likely to be very different. In the case of replacement no continuity is required and thus any correlation to an increase in permeability is unclear. In the case of the dilation associated with slip, continuity of pore space is more likely because the dilation is caused by asperities or breccia clasts which force the walls of the fracture apart, and that forcing must extend along large portions of the fracture wall. Thus while, the presence of the clay constitutes part of the skeletal porosity, it does not easily distinguish the source of the porosity and its implications for permeability and fluid flow history. Insight from other measurements including thin

section textural analysis and XRF mapping of elemental composition is required to distinguish the role of the two mechanisms.

3.1.2 Macroscopic skeletal porosity

The transects of macroscopic porosity quantify the impact of fractures, their stage, and associated alteration on porosity structure of rock at Newberry. By comparing open and skeletal porosity, I reconstruct elements of the porosity history. Furthermore, the correlation of skeletal and open porosity to fracture stage, structural position (i.e., fracture, breccia, fault rock, altered region, host rock) also provide insights into the longevity of fracture porosity, which is critical to both the life cycle of hydrothermal systems and to enhanced low permeability geothermal systems. In the following section I quantify these associations. Note that these porosities have a resolution of 2 cm, which means that even fractures that contain 100% porosity will plot with lower porosities unless the fracture is more than 2 cm wide, and even sharp boundaries in porosity visible in the maps and core images will appear sloped in the porosity profiles.

At a macroscopic length-scale from mm's to 10's of cm's, both the clay and non-clay fracture groups demonstrated an overall trend of increasing healed fracture porosity and skeletal porosity with each successive fracture stage. The skeletal porosity most clearly demonstrates this trend in both non-clay and clay groups (Figure 24). In both groups the skeletal porosity peaks at the center of the main fracture zone, and in successive measurements away from the center it tapers to the background primary porosity level present in the host rock. However there are clear differences between the two systems.

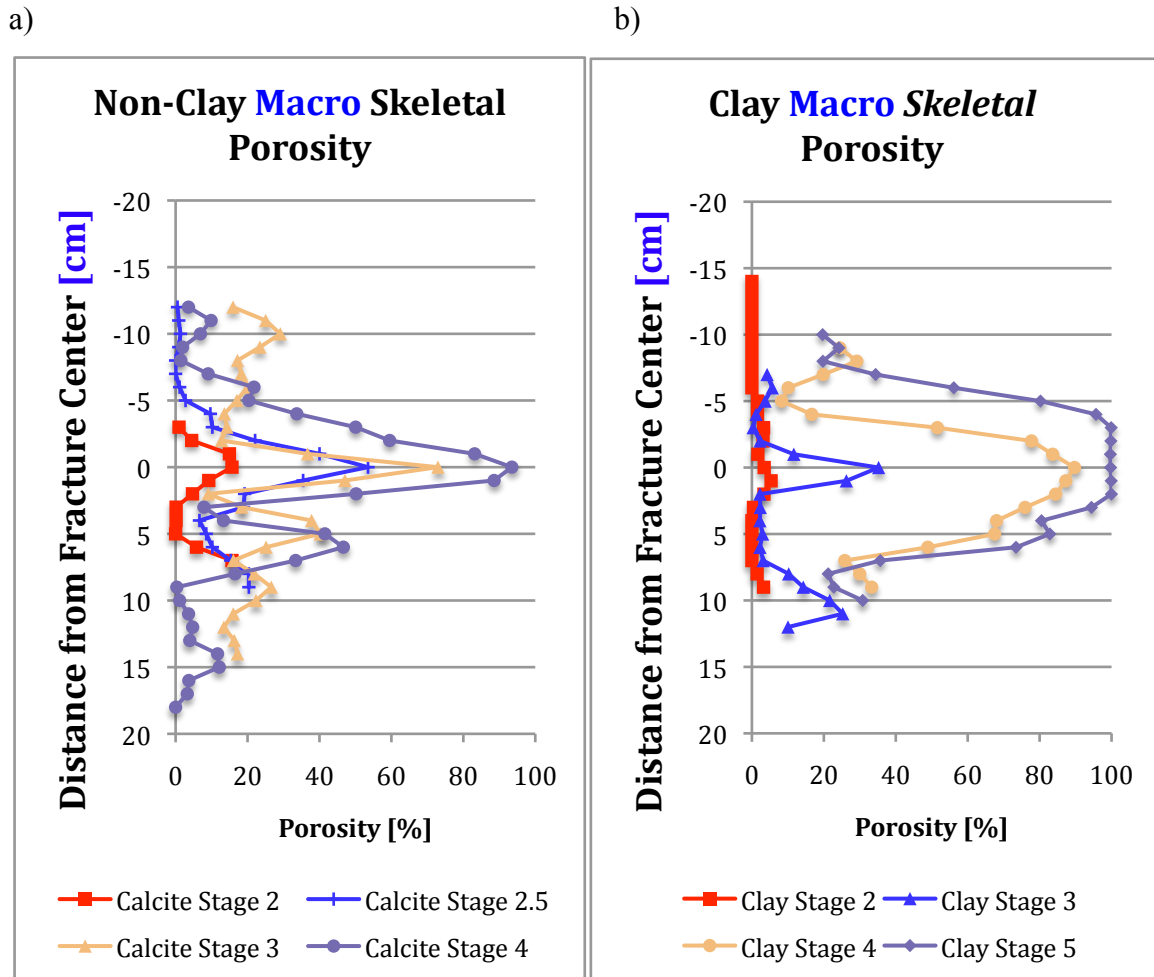


Figure 24: Figures showing the measured skeletal porosity along the length of cores for the a) non-clay group and the b) clay group.

The skeletal porosity in the non-clay fractures shows sharper peaks at all stages of development with only modest gains if any outside the main fracture. The porosity is quite high on individual structures and approaches 100% of the 4 cm² areas of large fractures that exceed to 2 cm length of the sample area. Porosity remains consistently high across the entire fracture. The clay-filled fractures show more gradual increases in porosity and broader zones of porosity increase across the fracture surfaces and are heterogeneous within the fracture.

Thus the non-clay fractures have higher porosity than their clay stage equivalent. This reflects the highly localized porosity of non-clay fractures, especially at early stages of development, which have very little macroscopic damage at the margins. The clay groups exhibit more of a gradual transition from fracture zone to protolith, coincident with their damage zone and the alteration of the surrounding host rocks. Here the porosity falls between that of the fracture zone and that of the protolith even when considering the limits on the analysis due to the 2 cm resolution. Comparing the porosity against distance from the center of the fracture in the clay and non-clay group in stage 4 demonstrates this difference most clearly (Figure 25d).

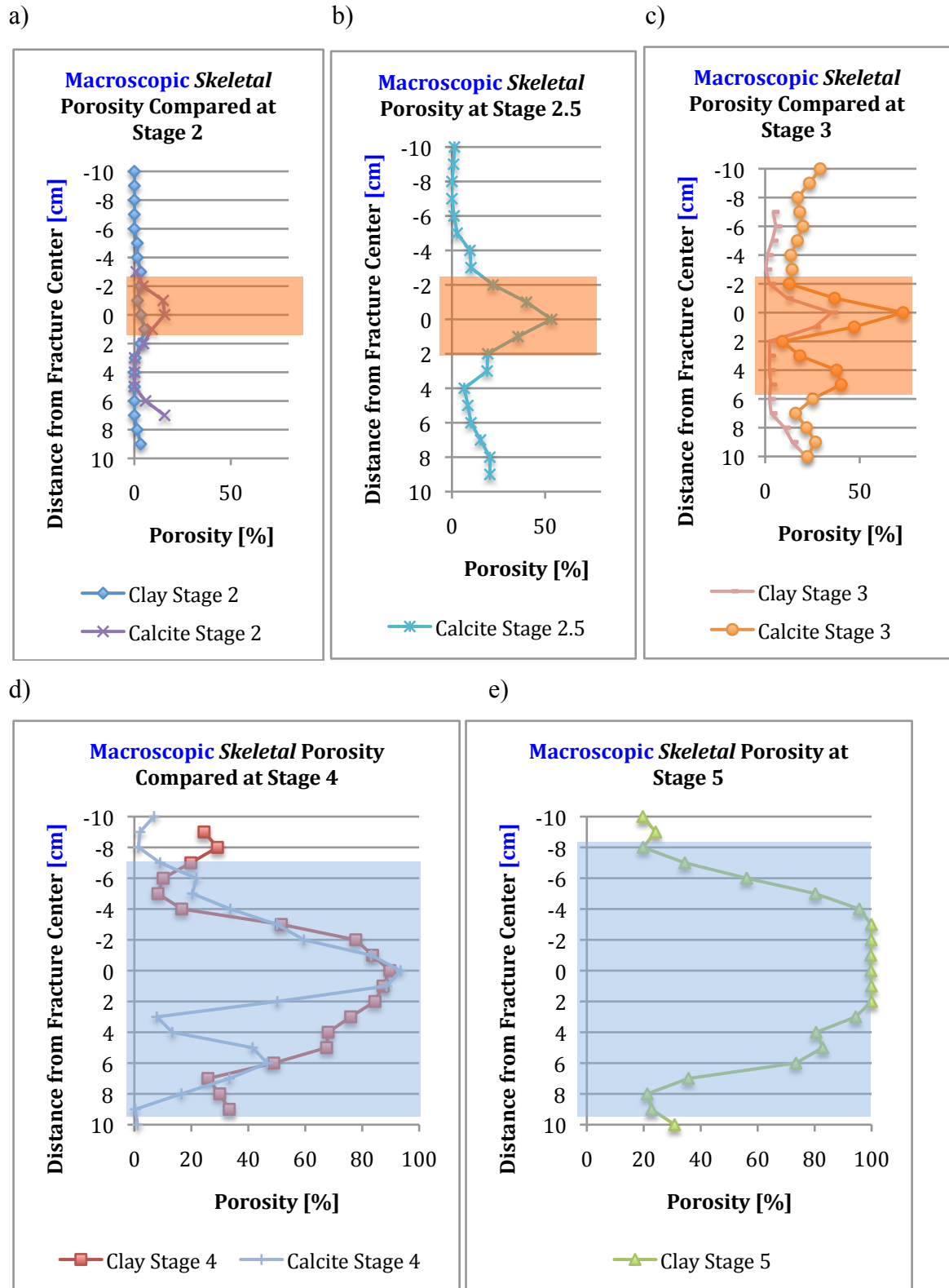


Figure 25: Figures comparing the measured skeletal porosity along the length of cores presented by stage. The red shaded area represents the width significant skeletal porosity from the center of the fracture in the pre-brecciation stages. The blue shaded area represents the width significant skeletal porosity from the center of the fracture in the post-brecciation stages.

A comparison of the porosity of the non-clay and clay groups at corresponding stages shows relationship between fracture width and stage of fracturing. Stages 2 through 3 in both the clay and non-clay groups show a reach of skeletal porosity within 2-6 cm of either side of the main fracture (Figure 25a, 25b, 25c). At stages 4 and 5 the reach of skeletal porosity increases to 6-9 cm on either side (Figure 25d, 25e). This sudden increase highlights the transition from the single-fracture system of stage 3 to the multiple-fracture, brecciated system of stage 4.

3.1.3 Macroscopic open porosity

In most hand samples macroscopic open porosity was not present. Only in non-clay stages 3 and 4 was there any measureable open porosity, at 3.5% and 23% open porosity, respectively (Figure 26a). The open porosity generated in non-clay stage 3 primarily reflects the presence of empty vugs, not a result of fractures (see Figure 16 and Figure 22). The microscopic porosity data shows that open porosity is generated in the fracture zone in all stages of non-clay fractures, but that it does not last within the Newbery geothermal system due to healing by mineral precipitation. However, large, more developed fractures stages including stage 4 and beyond might be able to retain porosity for long periods, in part due to large porosity production.

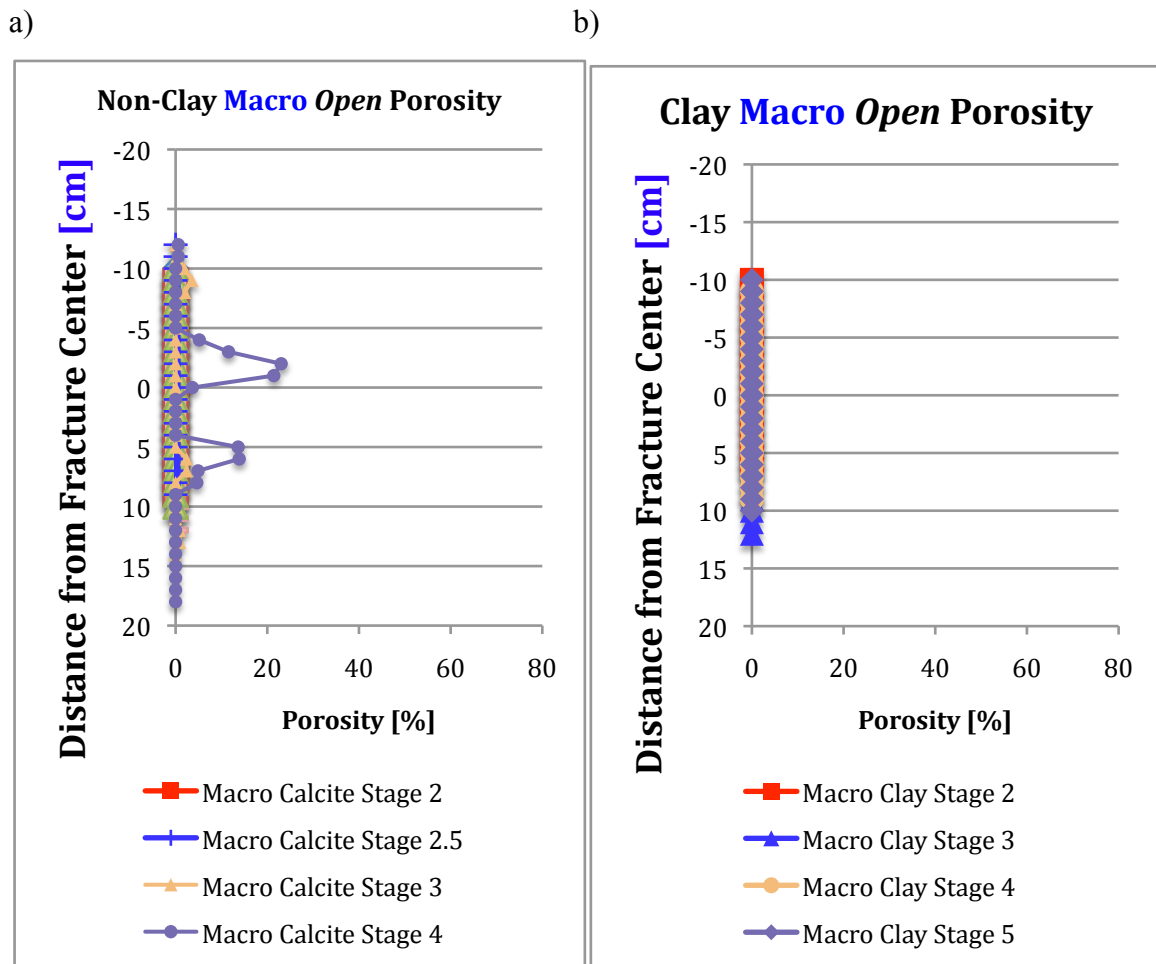


Figure 26: Figure comparing the measured macroscopic open porosity along a common axis for a) the non-clay group and b) the clay group.

There was no measureable macroscopic open porosity in any of the clay samples (Figure 26b). This is consistent with the conceptual model that clay systems do not create dilation that leads to the generation of open porosity, as outlined in Figure 5. However, the meaning of the widening of the zone of skeletal porosity must still be considered.

3.1.4 Macroscopic maximum porosity trends

The results of the macroscopic porosity analysis show an overall trend of increasing maximum porosity with each developmental stage, peaking in the non-clay group at stage 4 and in the clay group at stage 5 (Figure 27). The non-clay group demonstrates increasing skeletal porosity accompanied by increasing open porosity. The clay group demonstrates a noticeable lack of open porosity growth to accompany the skeletal porosity growth.

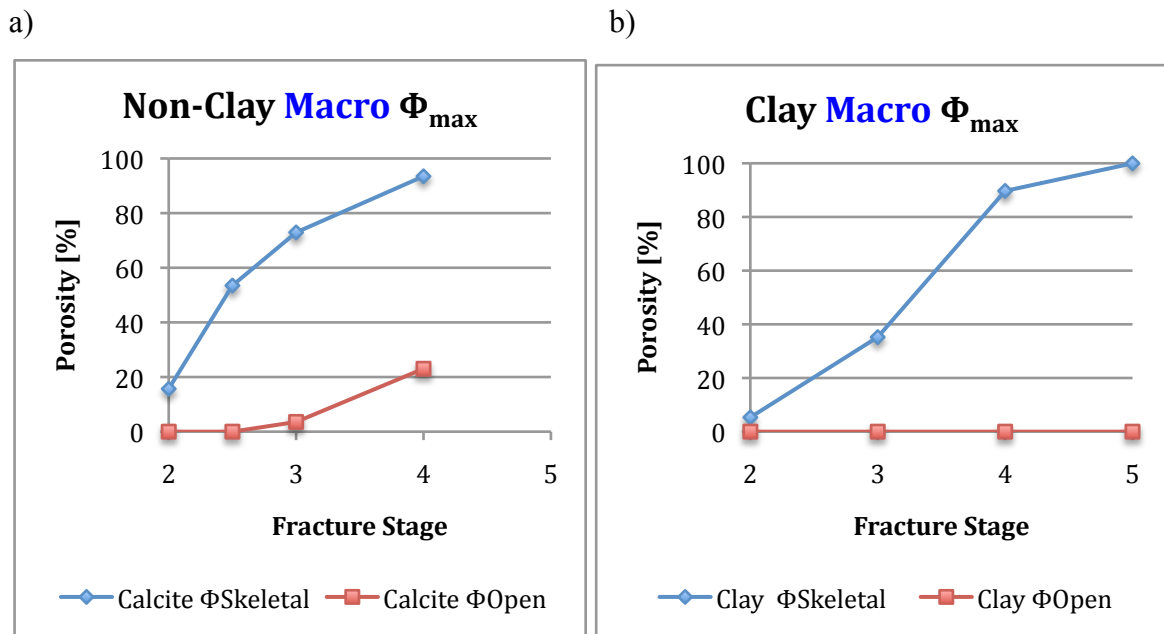


Figure 27: Figure presenting the maximum skeletal and open porosity measurements, by stage for the a) non-clay group and the b) clay group.

Although the shape of these curves are constrained by very few data points and the stages are largely qualitatively making them imprecise, the non-clay system is characterized by a very steep increase in skeletal porosity, consistent with large porosity gains in the early stage of fracture development. This is followed by a pronounced reduction in slope at over the successive stages. The clay group shows the same rollover in skeletal porosity at later stages of development, but the initial apparent rate of porosity gain is much lower at the initial stages. The transition from stage 4 to 5 in the case also coincides with the loss of breccia in the fault core. To determine if these are characteristic shapes, and not an artefact of sampling will require better constraints on the x-axis, such as slip or shear strain, which are not available in this study and more examples. Certainly a high degree of scatter should be expected that is not captured by the eight examples analyzed here. Nevertheless, these trends suggest that as a fracture continues to develop in response to repeated shearing porosity is increased but will achieve some maximum stable value associated with fault rock development.

3.2 Microscopic Porosity Results

3.2.1 Maps of microscopic structures, fault rocks and related porosity

The microscopic examination of the thin sections reveals open and healed crack porosity at a sub-millimeter scale that was not apparent in macroscopic length-scale. Figures 26 and 27 compile the photographs of each thin section sample in plane polarized light and select samples in crossed polarized light. Figure 28 shows the mapping of porosity assigned to each sample.

The non-clay stage 2 (Figure 28) thin section shows a sub-millimeter thick fracture bordered by two smaller fractures on both sides of it. In contrast to the clay-stage 2 there is a sharp, narrow transition from fracture to host rock, with very little damage zone apparent.

The thin section for non-clay stage 2.5 (Figure 28) shows a fracture zone roughly 7 mm wide. The fracture is primarily filled with calcite and quartz. Some mm-sized host rock clasts are incorporated within the fracture zone. These clasts scale with the roughness of the fracture, indicating they might have been derived from erosion of asperities on the fracture surface during slip. Some open porosity can already be distinguished in this stage running through the middle of the quartz and calcite cement between the clasts. Like stage 2, stage 2.5 shows a minimal amount of damage zone between the fracture and host rock.

In non-clay stage 3 (Figure 28), the fracture zone is 11 mm wide. The cross polarized photomicrograph shows quartz, identified by undulating extinction, lining the border of the fracture while calcite, characterized by low-birefringence, fills the center. A fracture containing open porosity cuts across the width of the transect in the middle of the fracture. The border between the protolith and the fracture is very sharp similar to the non-clay stage 2 example, showing minimal development of off-fracture damage.

In stage 4 (Figure 28) the fracture zone is 2 cm wide. The number of distinct quartz and calcite deposits within the fracture-filling cement is higher than in non-clay stage 3, suggesting a history of repeated fracturing and healing. A damage zone is also evident at the margins of the large pores, and is associated with minor alteration to the host rock directly adjacent to the fracture zone. A very large open pore resides in the center of the fracture. The quartz-calcite filling encompasses volumes of gouge, indicating dilation was concurrent with some alteration and gouge development.

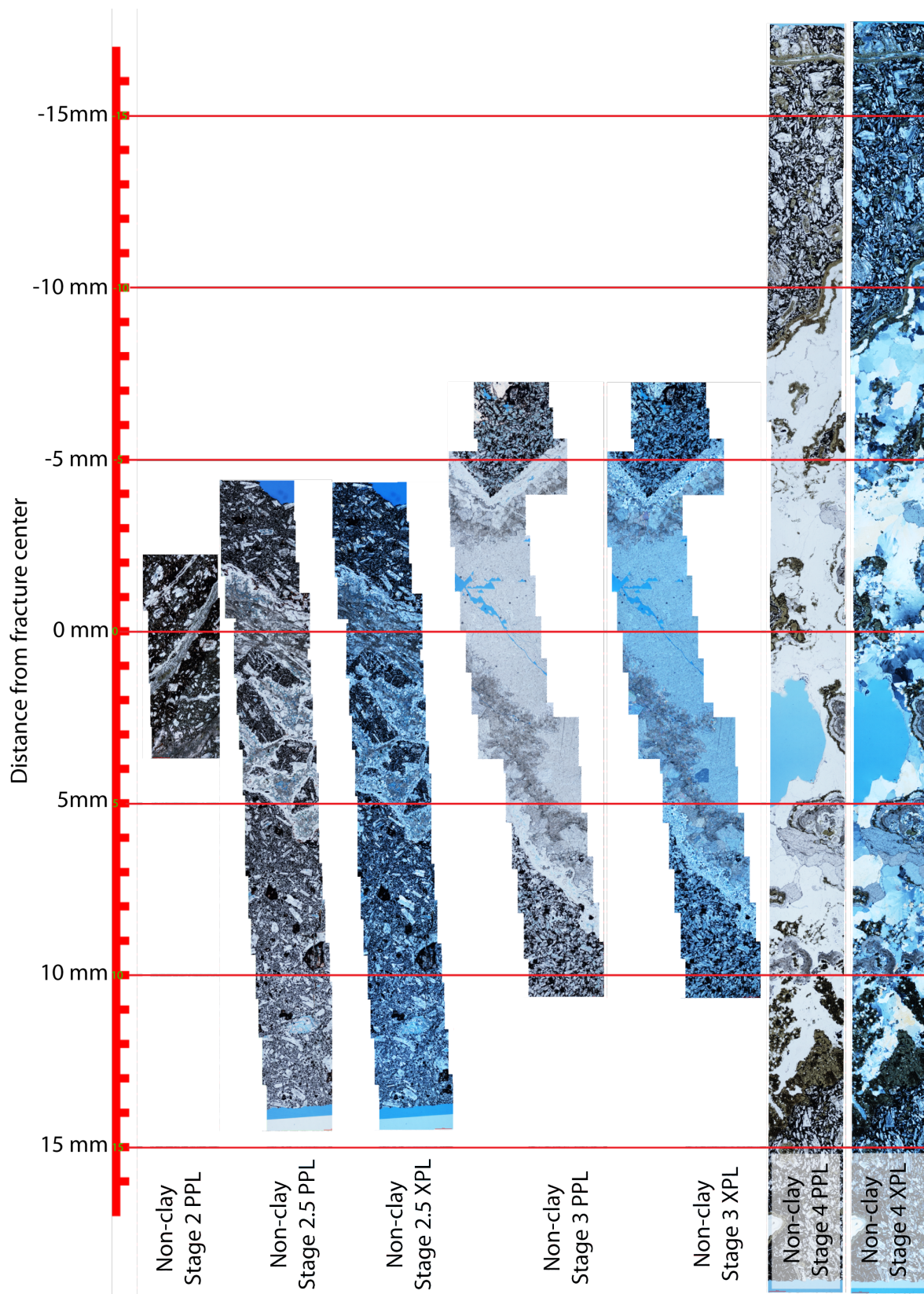


Figure 28. Photographic transects of non-clay thin sections. 0 mm is calibrated at the center of the fracture for all stages. Positive values indicate downwell distance, negative numbers indicate up well distance. PPL stands for plane polarized lens, XPL stands for crossed polarized lens.

Under the microscope, clay stage 2 (Figure 29) contains an immature fracture <1 mm wide which is bordered by a damage zone extending ~1 mm to either side of the fracture comprised of grain scale fractures. The fracture zone is associated with green tinged alteration mineral and a white minerals, either calcite or quartz, cutting through the plagioclase-dominated host rock. This is evidence that in the clay-dominated fracture systems: (1) micro-cracking forms around even the simple fractures and is associated with the extent of alteration into the host rock bordering the fractures surfaces, (2) these microcracks represent small-scale dilation that is subject to healing by high-strength minerals as well as phyllosilicates.

In clay stage 3 (Figure 29) the fracture zone has widened to approximately 5 mm and shows trace amounts of remnant open porosity in the very center of the fracture. The fracture has significant calcite deposits, which can be identified by low birefringence in the crossed-polarized (xpl) view of the slide. The edge of the fracture is more difficult to define in this sample because the damage zone bordering the fracture has been heavily altered and preferentially depleted of identifiable plagioclase crystals. The damage zone includes many calcite and quartz inclusions, some of which show evidence of being altered to chlorite. The boundary of this fracture is associated with a transition from darker-colored background matrix to a lighter-colored background matrix. Note that there are more quartz and calcite filled cracks in the damage zone than in the fracture itself, giving the damage zone a higher healed crack porosity and distinct mineralogy. In this example, the clay-filled fracture exhibits lower skeletal porosity than the surrounding damage zone. The decrease in skeletal porosity in the clay-filled fracture points to a lack of dilation during fault slip. The increase in skeletal porosity in the damage zone relative to the fracture core suggests a shift of dilatancy and fluid flow away from the fault core and into the damage zone. In stage 3 the clay fracture begins to act as a barrier to fluid flow, forcing incoming geofluids to flow parallel to the fracture and further extending the damage zone through alteration.

Stage 4 (Figure 29) provides a detailed view of the brecciation associated with the later stages of fracture evolution. Fracture-bounded volumes of altered but relatively intact host rock are bordered by a filling of clays and some high quartz. XRD analysis shows the clay minerals are mostly chlorite and illite. The clasts still retain some sharp corners and edges. This suggests relatively little transport or alteration since its formation, both of which would preferentially degrade such sharp corners. The presence of both fresh and altered clasts suggests continued breccia formation.

The thin section for clay stage 5 (Figure 29) is positioned at the border between the gouge in the fracture core and the damage zone defined by high fracture density. The gouge at the top of the transect shows complete alteration and replacement of host rock mineralogy in contrast to the damage zone below it. XRD analysis indicates the clay minerals in the gouge are mostly chlorite and illite. The damage zone in stage 5 shows multiple calcite and quartz-filled fractures at the transition between the gouge and damage zone indicating some dilation plays a significant role at this boundary. However, this dilation lacks the sharp boundaries characteristic of fracturing often possessing rounded edges to the pores. These pores are often lined with either quartz or calcite suggesting some dilation in which to allow the precipitation. This is somewhat distinct from earlier stages of the clay-filled fracture development in which zones of clay showed the least dilation (e.g., stages 2 and 3).

The damage zone in clay stage 5 is similar to the breccia of the fracture zone in stage 4 and breccia is currently evident at the upper margin of the fault rock, as evidenced in the macroscopic scales shown in figures Figure 20, Figure 21 and Figure 23. This similarity in conjunction with the on-going dilation along the contact between gouge and host rock suggests the fracture formation in the damage zone and eventually brecciation continues at this stage of fault development.

This is the only clay stage to exhibit open porosity on the >1 mm scale. However porosity development at this stage is heterogeneous and anisotropic. It only occurs in the host rock at the margins of the fault core and does not cross the fault core, thus producing extensive zones of porosity parallel to the fault core.

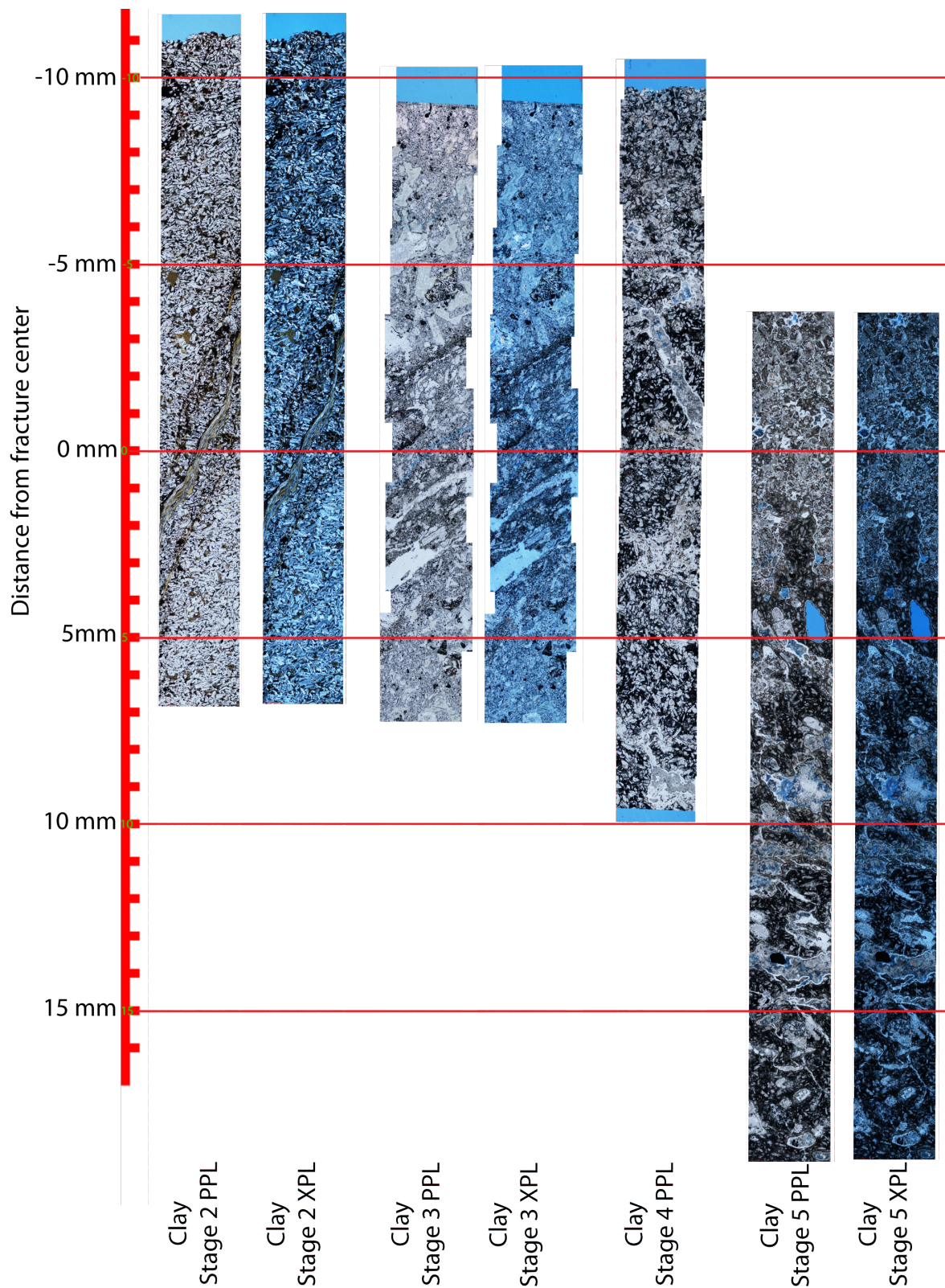


Figure 29: Photographic transects of clay thin sections. 0 mm is calibrated at the center of the fracture for all stages. Positive values indicate downwell distance, negative numbers indicate up well distance. PPL stands for plane polarized lens, XPL stands for crossed polarized lens.

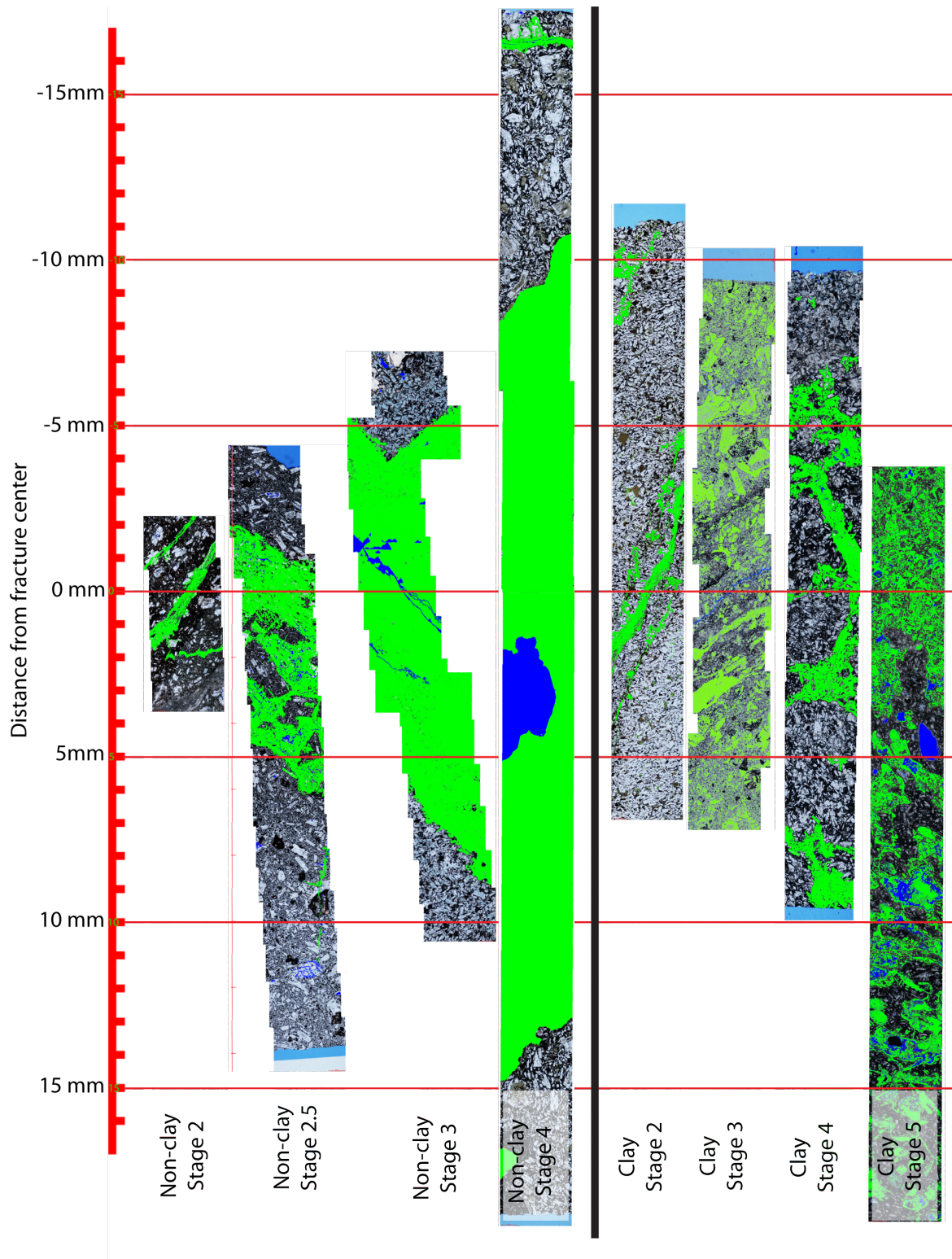


Figure 30: Porosity maps of all thin section transects. 0 mm is calibrated at the center of the fracture for all stages. Positive values indicate downwell distance, negative numbers indicate up well distance. Solid blue color marks open porosity, solid green marks healed crack porosity.

3.2.2 Microscopic skeletal porosity

Microscopically, the clay-dominated and non-clay fracture groups each display distinct trends in skeletal porosity development throughout the fracture evolution (Figure 31). The non-clay group displays a trend of increasing skeletal porosity and increasing width of the main fracture zone in each successive fracture stage (Figure 31a). The skeletal porosity maps are distinguished by sharp drops in porosity at the edges of the fracture zone, signalling that the porosity is limited to the fracture zone. None of the stages demonstrated the development of a damage zone characterized by skeletal porosity levels intermediate between that of the fracture zone and the protolith. Stage 4 of the non-clay group had a damage zone characterized only by minor mineral alteration (Figure 32d).

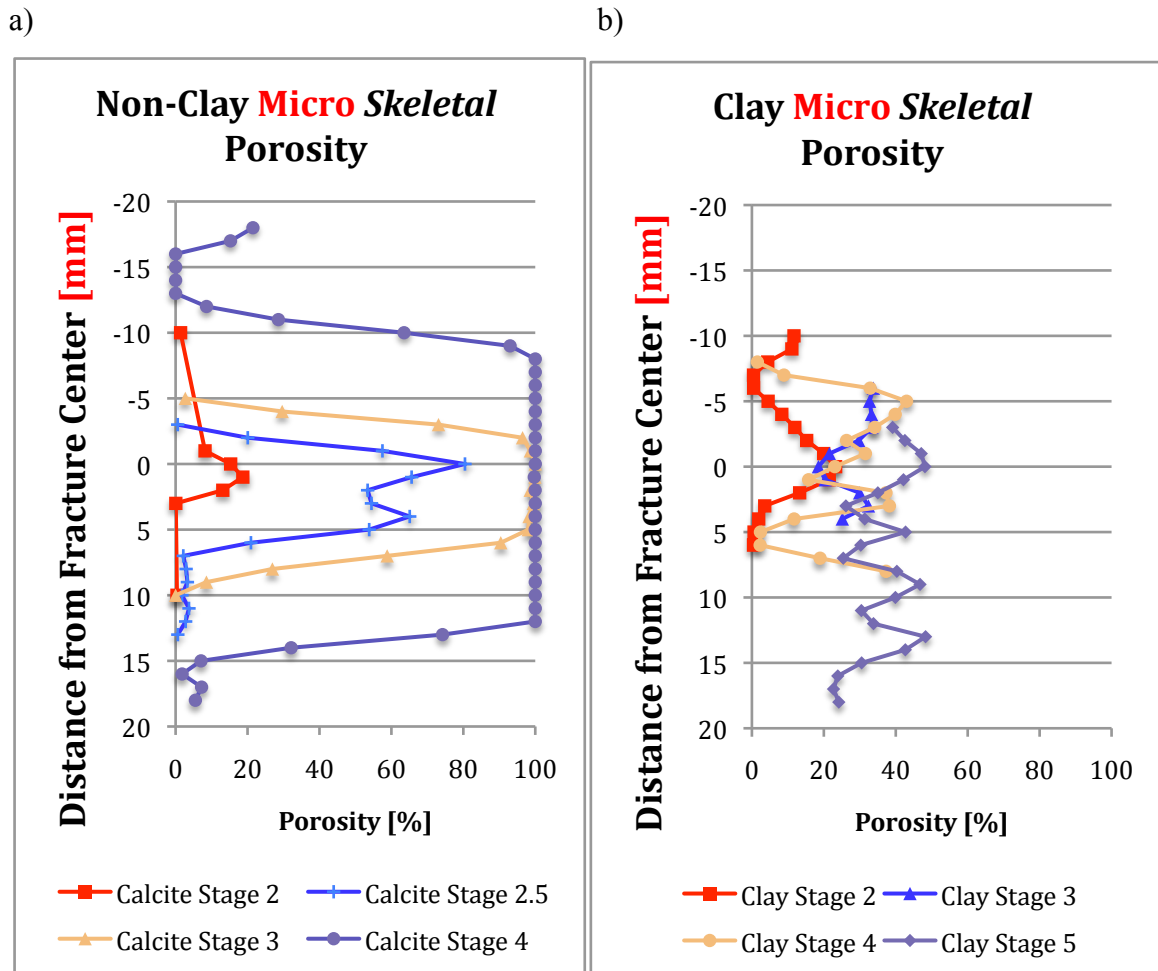


Figure 31: Figures showing the measured microscopic skeletal porosity along the length of cores for the a) non-clay group and the b) clay group.

After reaching 25% skeletal porosity in stage 2 the maximum porosity level in the clay group appears to asymptotically approach 50% by stage 5 (Figure 31b). In stage 2 the high porosity zone is focused around a 5 cm wide width (Figure 32a). At stage 3 of the fracture zone becomes essentially clogged with clay, reducing skeletal porosity in the fracture relative to the damage zone (Figure 32c). In clay stages 4 and 5 the skeletal porosity in the fracture zone is no longer distinguishable from the damage zone (Figure 32d, Figure 32e). In clay stage 4 this is due to the thin section not being wide enough to capture the entire width of the core's macroscopic fracture zone. However, the data for clay stage 5 includes

the fracture-damage zone boundary and it does not show a distinguishable difference in porosity between the two. By stage 5, the width of the high porosity zone has extended to the entire width of the thin section, roughly 2cm. The clay group is characterized by an overall widening of the fracture zone without a substantial increase in skeletal porosity beyond stage 3. In both cases, the trends mimic the behavior recognized in the macroscopic porosity data.

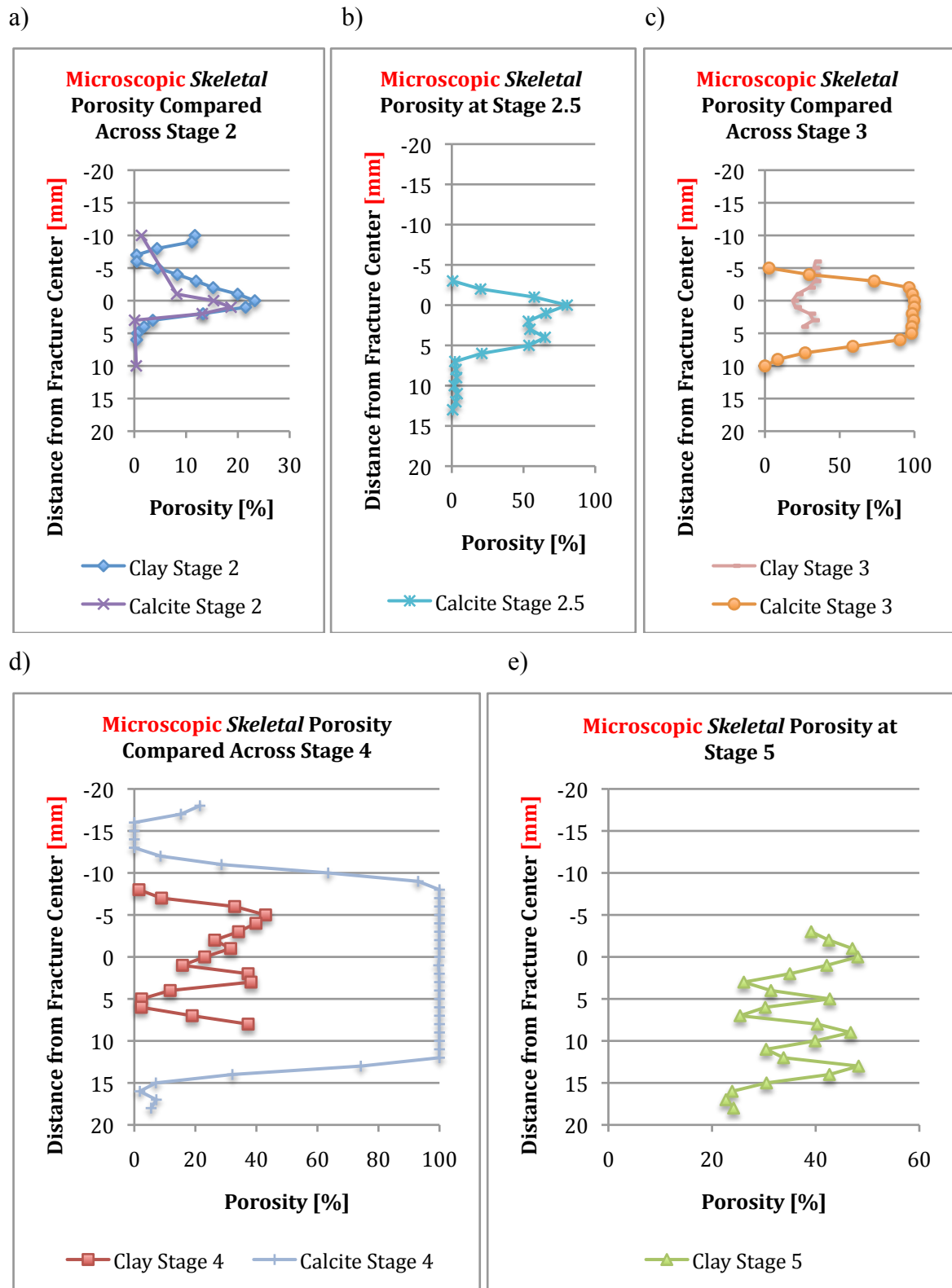


Figure 32: Figures comparing the measured microscopic skeletal porosity of the clay and non-clay groups along the length of the cores at each stage.

3.2.3 Microscopic open porosity

Microscopic porosity was detectable in every stage in both the clay and non-clay groups. However, in the non-clay group, the open porosity levels did not rise above 5% until stage 4 (Figure 33a) although a rising curve is recognizable across the stages. In the clay group, only stage 5 showed a significant increase and in previous stages no increase in porosity was discernable (Figure 33b). This data shows continuity with the macroscopic non-clay group measurements, which also showed the only significant increase in open porosity at stage 4. This data also proves that open porosity did develop by stage 5 in the clay group even if it was not macroscopically measureable.

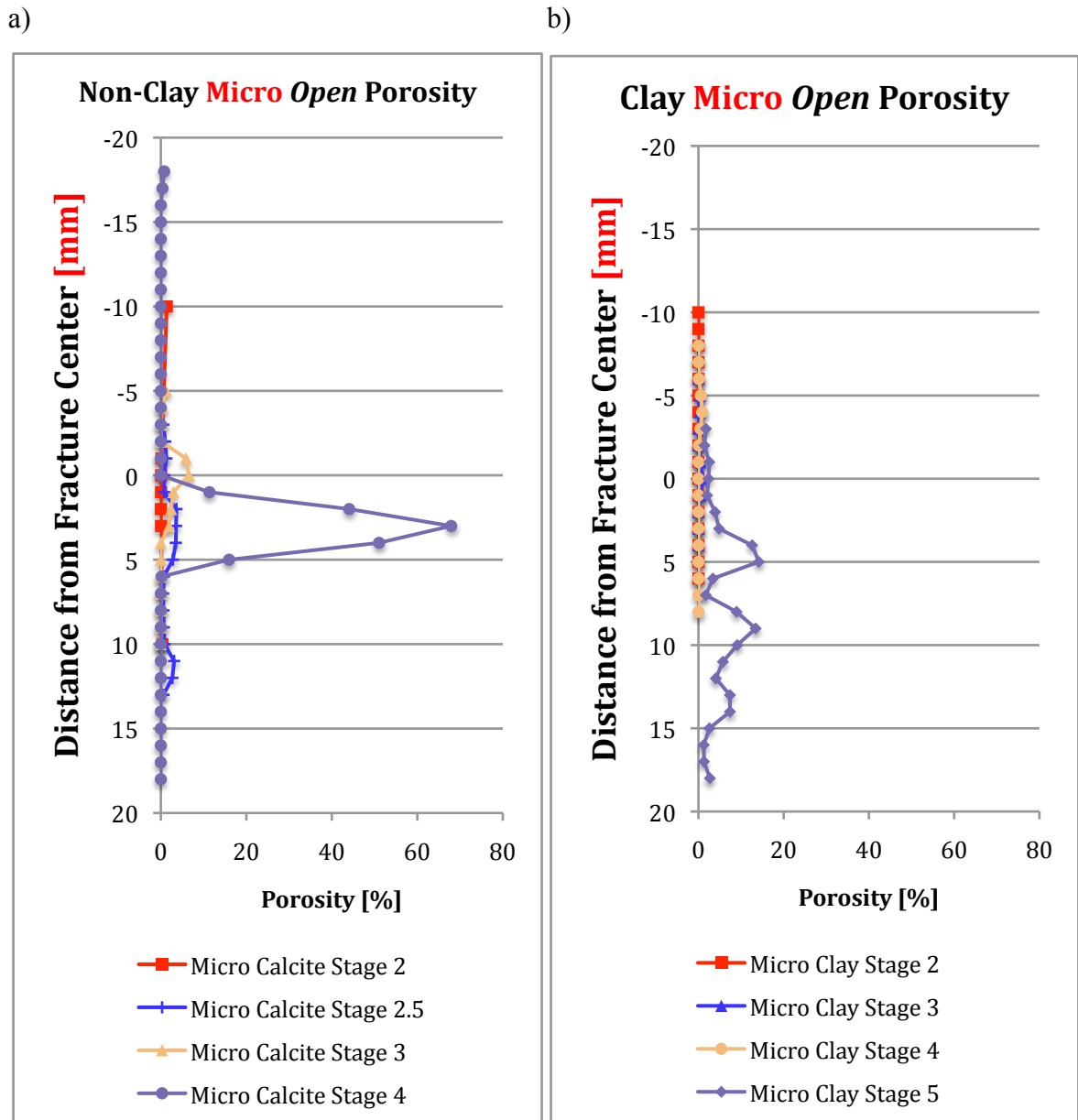


Figure 33: Figures showing the measured microscopic open porosity along the length of cores for the a) non-clay group and the b) clay group.

3.2.4 Microscopic maximum porosity trends

The results of microscopic porosity analysis show an overall trend of increasing maximum porosity with each developmental stage, peaking in the non-clay group at stage 4 (Figure 34a) and in the clay group at stage 5 (Figure 34b). This trend matches the trend found in the macroscopic maximum porosities. However, as compared to the macroscopic trends, the microscopic trends show a sharper increase in porosity from non-clay stage 2 to 4 and show a shallower increase from clay stage 2 to stage 5.

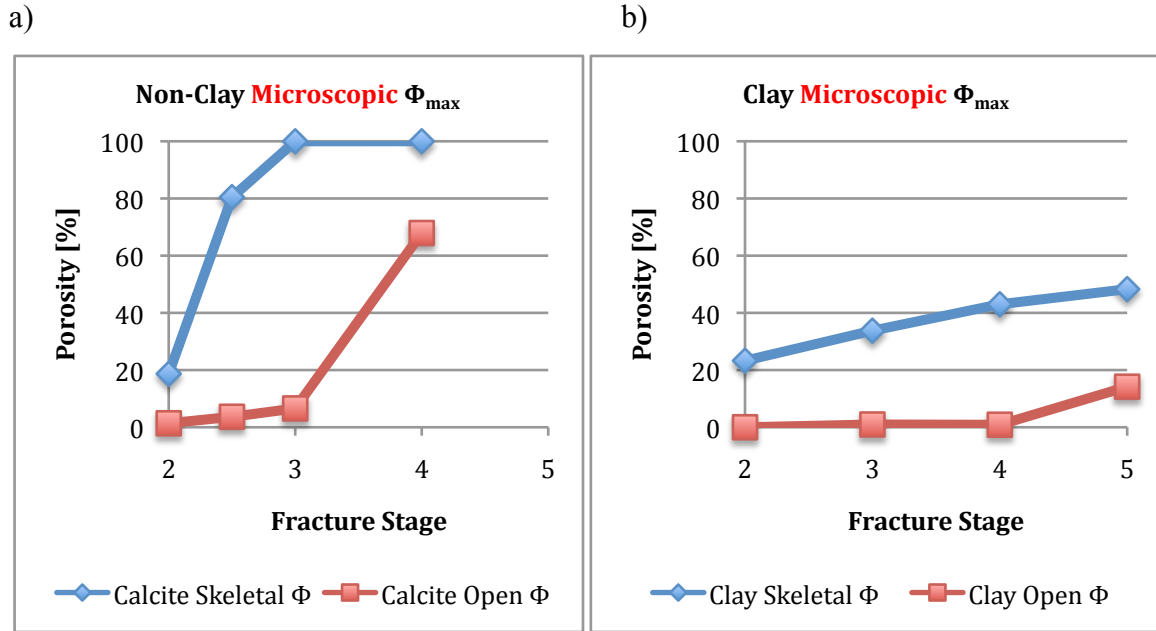


Figure 34: Figures showing the maximum value measured for microscopic skeletal and clay porosity at each stage for a) the non-clay group and b) the clay group.

3.3 XRF Analysis: Independent Evidence of Fluid Flow

In Figure 35 and Figure 37 the immobile elements Ti and Zr are plotted against each other for each sample. A strong linear correlation or dense grouping in the cross plot helps to confirm that they both behave as relatively immobile elements, without their concentration subject to extensive change due to solution mass transfer. As a result comparison of the ratio defined by other elements to these immobile elements, solution mass transfer can be detected.

In the non-clay group, stage 2 (Figure 35a) shows the rock from the fracture center and protolith plot closely together, with a few vesicles as outliers. In stages 2.5, 3 and 4 the fracture center becomes very depleted in Ti and Zr relative to the protolith (Figures 35b, c and d). This signals an introduction of material into the fracture not originating from the host rock, but an outside source of fluid transported ions which should contain very low concentrations of Ti and Zr.

Another trend emerges in the non-clay group's damage zone. In stages 2-3 the damage zone plots within the protolith cluster, implying the damage zone is isolated from the fluid and that changes in mineralogy in this region occur without the influence of far-traveled geofluids. By stage 4, the damage zone plots between a two-end member line, between

host rock and fracture center. This implies that the geo-fluid has penetrated the damage zone and has filled it with Zr and Ti-depleted minerals.

All the Ti/Zr data for the non-clay systems plot to form a line representing a bi-modal system. The exotic material depleted in Ti and Zr (fracture center, veins, etc) at one end, host rock with relatively higher Ti and Zr concentrations at the other, and damage zone rock plotting somewhere in between. The trend is that this line becomes "stretched" out in each progressive stage. Because 1) the fracture zone becomes increasingly depleted in Ti/Zr relative to the host rock and 2) the damage also becomes increasingly depleted in Ti/Zr relative to the damage zone, but not as much as the fracture zone. The three zone types plot closer to each other along the bi-modal line in stage 2 than they do in stage 5.

Figure 36 plots the mobile element Ca against the immobile element Ti in the non-clay samples to track the movement of Ca-rich fluids necessary for the precipitation of calcite. In stage 2 the fracture rock plots more or less within the protolith cluster, implying low amounts of outside material injected into the fracture zone. In stages 2.5-4 the fracture center is Ca-enriched clearly beyond the levels of the host rock, signalling an increase in outside material filling the fracture zone. In stage 4 the damage zone rock has fallen into a range between the Ca-enriched fracture rock and Ca-poor host rock, giving another indication that the damage zone has been infiltrated by an outside fluid. The Ca/Tr plots confirm the trends in the Ti/Zr plots.

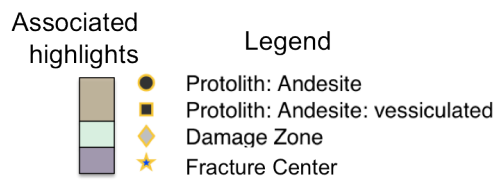
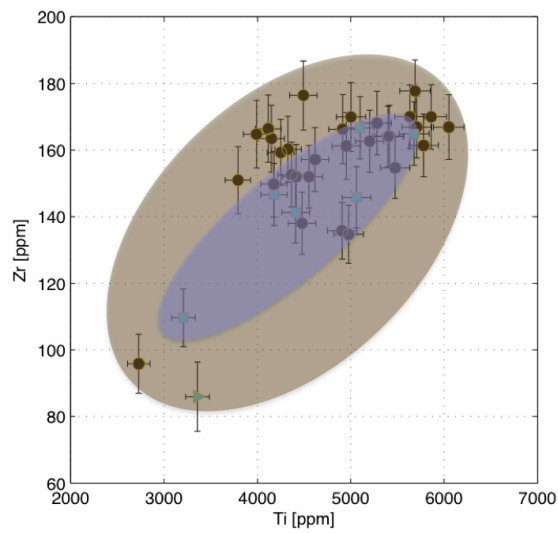
For the clay groups, Figure 37 reveals a different kind of bi-modal system emerging. In a Ti-Zr plot, stage 2 clay shows a distinction between the fracture zone (labelled here as clay gouge) and the basaltic protolith. In stage 3 this distinction still remains. The first two stages show a distinctly different element source entering the system at the fracture zone. In stage 4, the single host rock measurement plots within the fracture zone group (labelled breccia in phyllosilicate). The fracture zone and the damage zone are still somewhat distinct from each other, but some overlap between them occurs. In stage 5, any distinction between host rock, fracture center and damage zone is lost. All the data plots along an approximately straight line. In this stage the host rock plots as end members, between which plots all the fracture and damage zone material, if we discount the outlying vesicle plots.

Like the Ti/Zr plots for the non-clay systems, the bi-modal line in the clay systems becomes "stretched out" as the fracture progresses. Also like the non-clay system, the clay system follows a [fracture center]/[host rock] end-member model of this line up until stage 3. Then during stage 4 and 5 the clay system shifts to a [host rock]/[host rock] end-member mode. In stages 4 and 5 exotic ions are no longer being brought into the system. Rather, ions are being exchanged between rock already present. This implies alteration replaces fluid injection as the primary transporter of ions. The evidence suggests that at stage 4 the clay-dominated fractures become "clogged" with clay and dilation stops occurring.

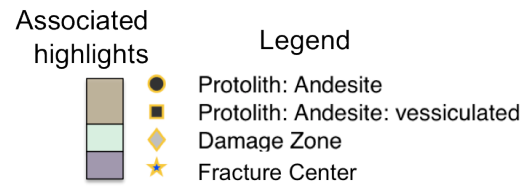
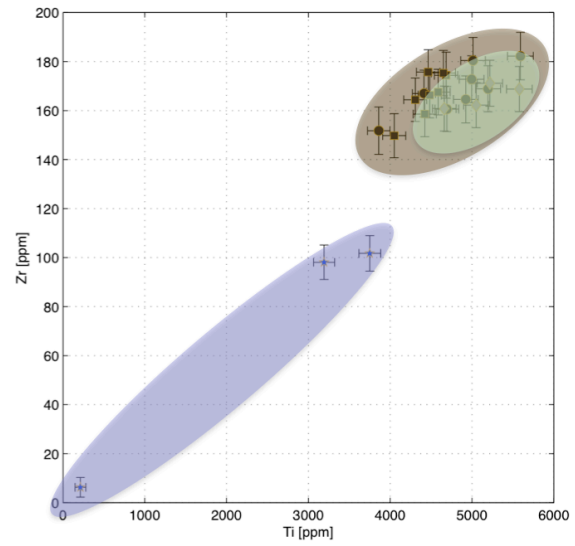
Patterns emerge in the Ti/Ca plots of Figure 38 for clays that confirm the change in the bi-modal system at stage 4. In stage 2 the single fracture zone datum plots below and to the left of the protolith cluster, signalling its depletion in Ca and Ti relative to the host rock. XRD analysis confirms this because the fault filling material is an oxidized iron-rich mineral. In stage 3 the fracture center plots slightly left of most of the protolith data, but lies closer to the protolith cluster than in stage 2. This suggests the amount of exotic material being into the fracture decreasing. In stage 4 all distinction between host rock, damage zone and fault zone has been lost and they plot in a tight group. In stage 5 the data is no longer tightly grouped but spread across a line with host rock as the end members. Like the Ti/Zr plot for the clay group, this Ti/Ca distribution over the 4 stages suggests a

decrease of exotic material entering the system and the increase of alteration between rock already present in the system.

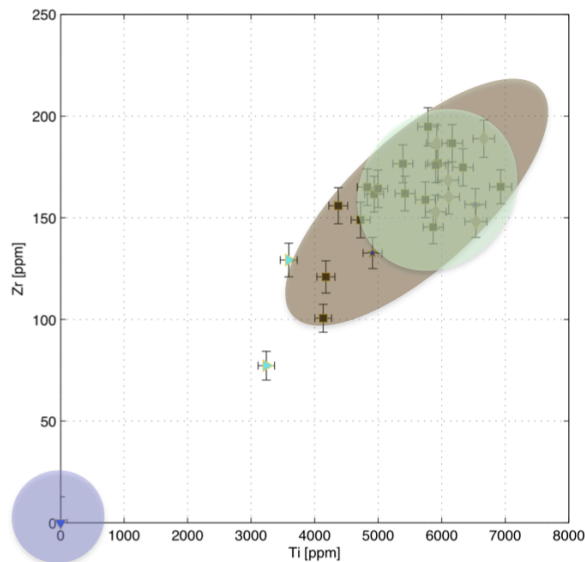
a) Non-clay Stage 2



b) Non-clay Stage 2.5



c) Non-clay Stage 3



d) Non-clay Stage 4

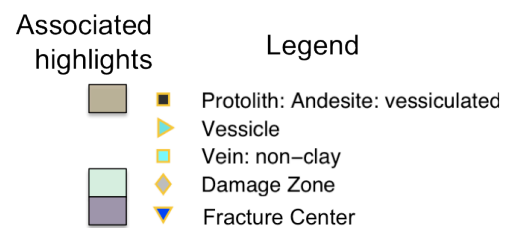
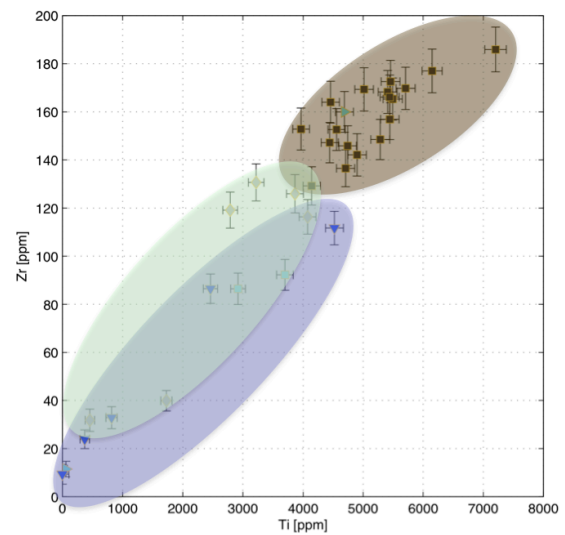
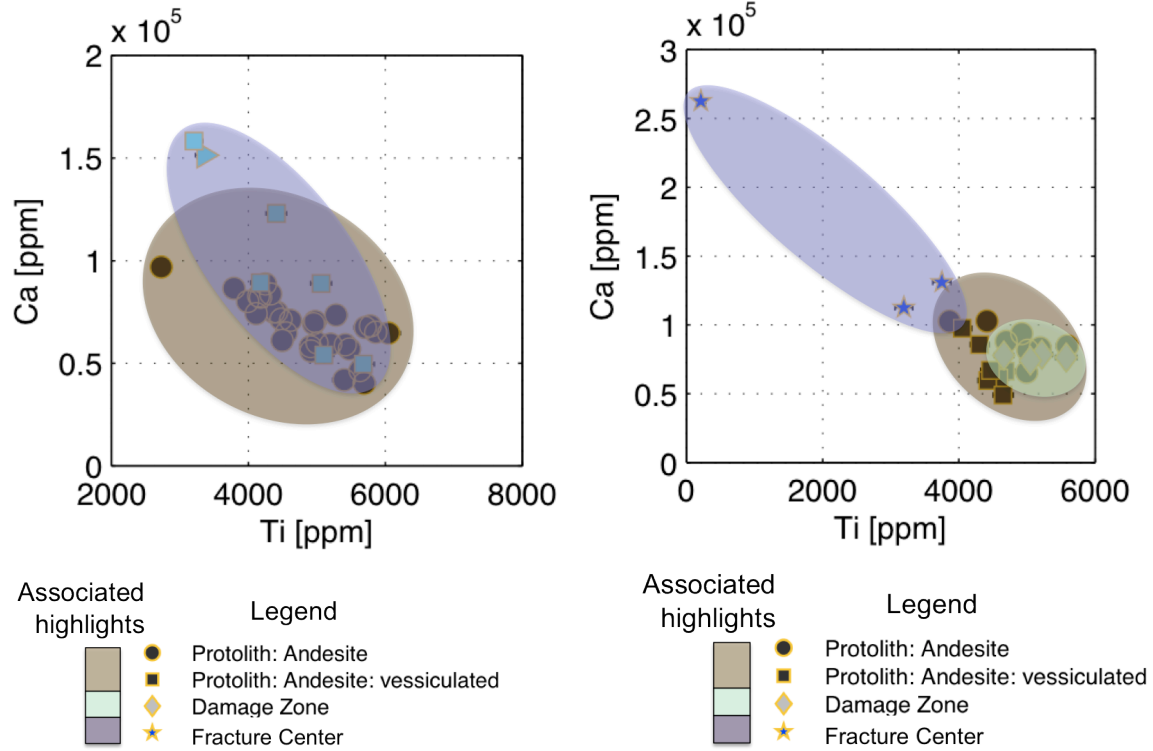
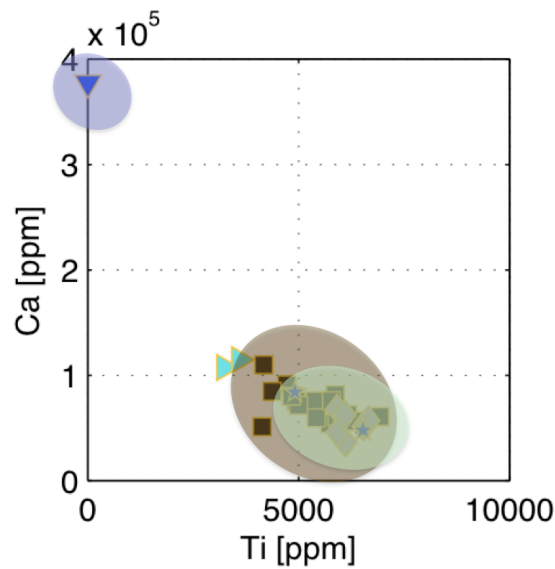


Figure 35: XY plots of Ti/Zr element ratios for each stage of the non-clay group. From the XRF data.

a) Non-Clay Stage 2 b) Non-Clay Stage 2.5



c) Non-clay Stage 3



d) Non-clay Stage 4

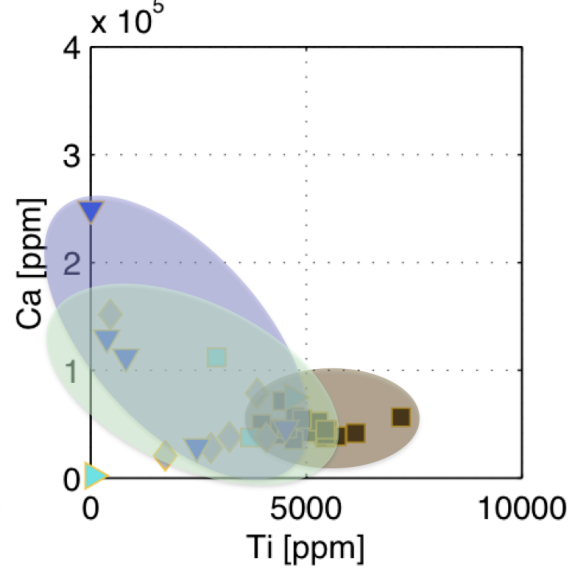
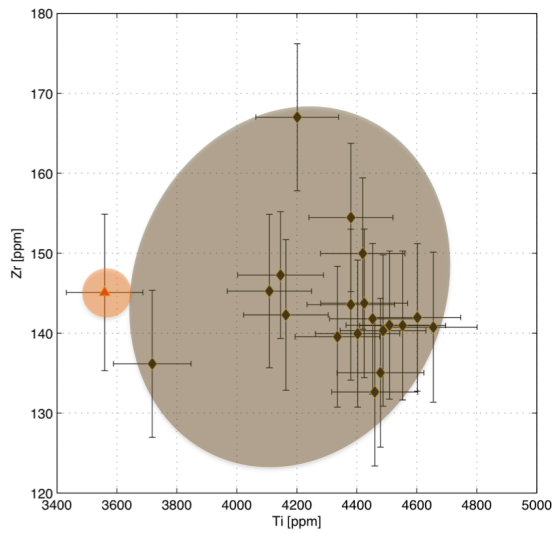


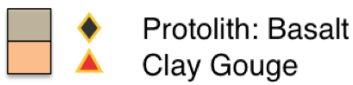
Figure 36: XY plots of Ca/Ti element ratios for each stage of the non-clay group. From the XRF data.

a) Clay Stage 2

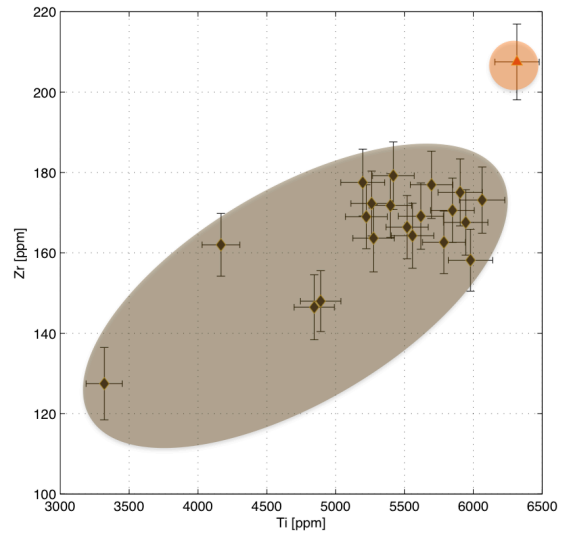


Associated highlights

Legend

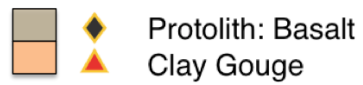


b) Clay Stage 3

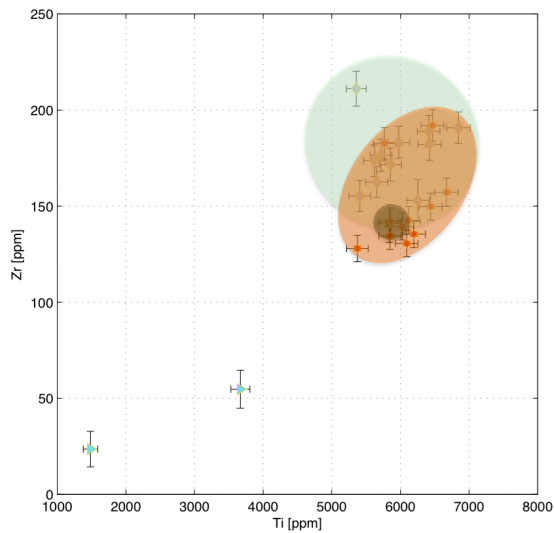


Associated highlights

Legend

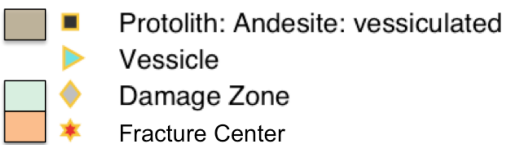


c) Clay Stage 4

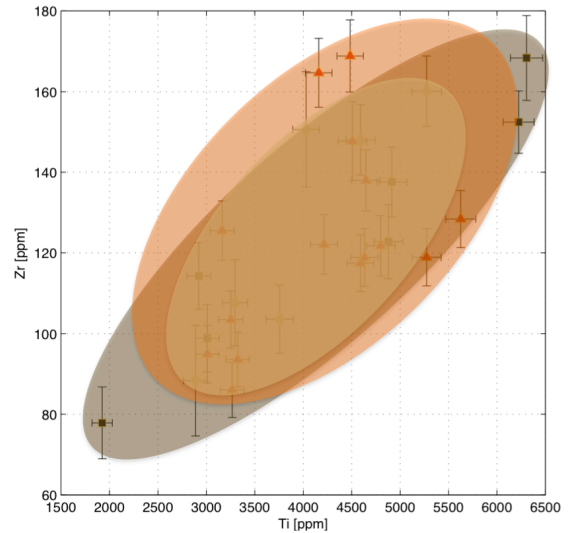


Associated highlights

Legend



d) Clay Stage 5



Associated highlights

Legend

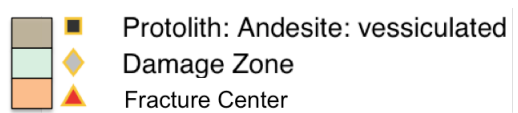
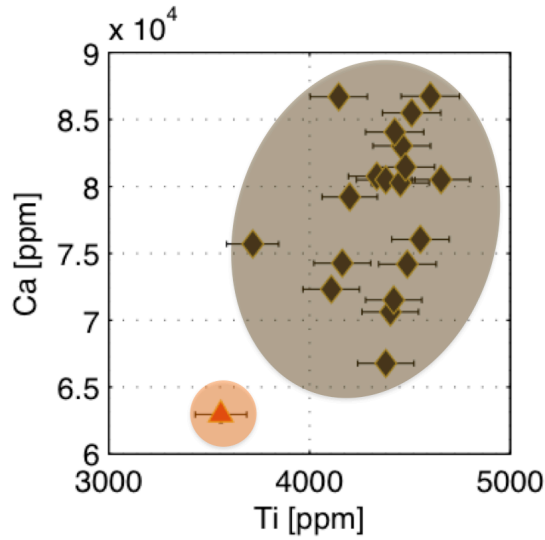


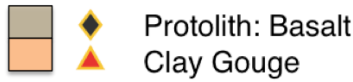
Figure 37: XY plots of Ti/Zr element ratios for each stage of the clay group. From the XRF data.

a) Clay Stage 2

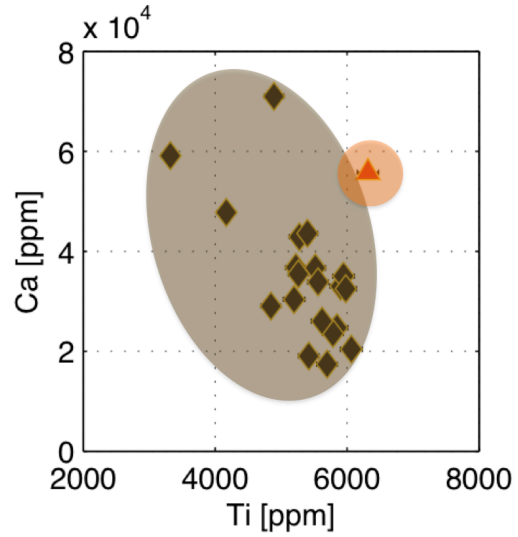


Associated highlights

Legend

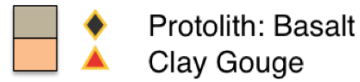


b) Clay Stage 3

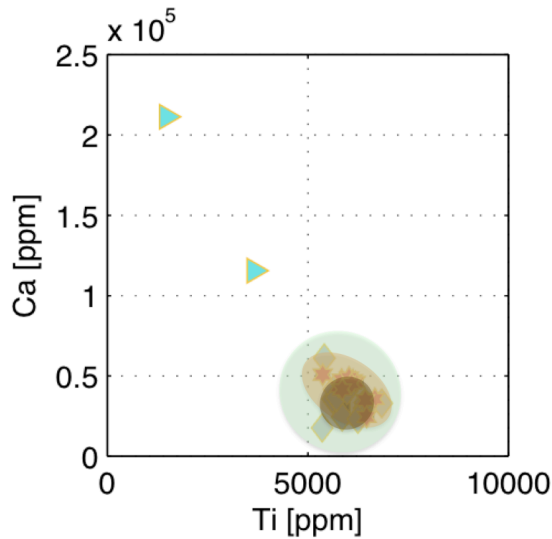


Associated highlights

Legend

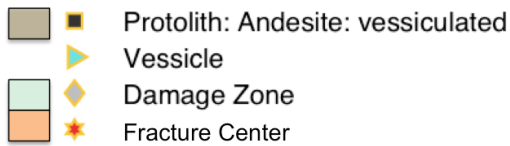


c) Clay Stage 4

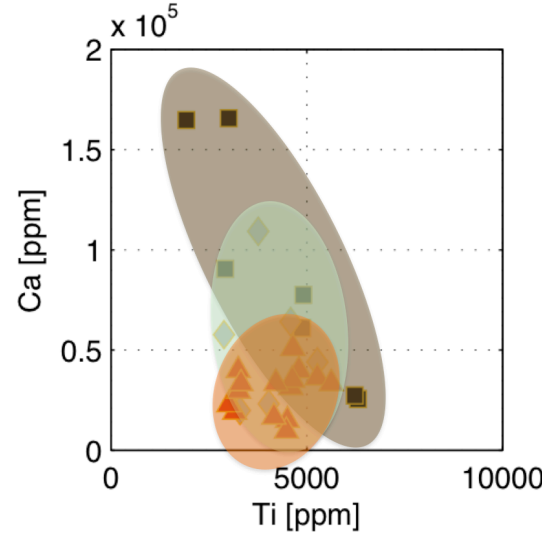


Associated highlights

Legend



d) Clay Stage 5



Associated highlights

Legend

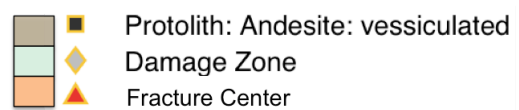


Figure 38: XY plots of Ca/Ti element ratios for each stage of the clay group. From the XRF data.

3.4 Correcting the Macroscopic Data for Clay Fractures

3.4.1 Macroscopic vs. Microscopic Porosity Measurements

In this study connecting macroscopic to microscopic measurements was difficult to achieve. This disconnect was in part due to the reliance of each measurement method on a different length-scale of observation, making it difficult to find a common quantitative framework to connect them. However, trends in each of the measurement scales were similar, and observations of the detailed porosity structure within macroscopic structure suggested a method to connect the two scales in attempt to correct macroscopic porosity data found to be inconsistent with the rest.

To compare the skeletal porosity found in the microscopic and macroscopic measurements, the maximum measured porosity values were cross-plotted (Figure 39). Plotting above the 1:1 line shows that the measured maximum skeletal porosity was higher in the microscopic measurements for a particular fracture system, while plotting below the line demonstrates the opposite. The data shows that only in the clay stage 3 system were the maximum measurements equivalent. The rest of the fracture systems do not follow a 1:1 correlation. In five of the eight analyzed fracture systems, microscopic measurements yielded higher maximums than the macroscopic measurements. Furthermore, the two systems yield roughly linear trends but with very different slopes. The non-clay system is associated with a slope relating change in microscopic porosity relative to macroscopic porosity of approximately equal to or greater than one. However, the clay system is reasonably fit by a slope of about a third. This suggests very different mechanisms, and length-scales of porosity production. It is important to note also that the initial stage of both groups show roughly similar skeletal porosity. The divergence only occurs at higher stages, suggesting each system evolves from similar origins.

Included in Figure 39 are plots of the corrected macroscopic skeletal porosity values for the stage 4 and stage 5 clay samples. The reasons for calculating these corrected values are explained in section 3.4.2, and the process of how these values were obtained is explained in section 3.4.3. Once the macroscopic skeletal porosity was corrected for in clay stages 4 and 5, the clay system is associated with a slope relating change in microscopic porosity relative to macroscopic porosity of approximately equal to or greater than one, like the non-clay system. The adjusted values suggest a strong correlation between the macroscopic and microscopic porosity measurements.

It should be noted that the skeletal porosity of the clay system and non-clay system are closely matched in stage 2. However, as fracture evolution progresses the clay group appears to asymptotically approach 50% while the non-clay systems skeletal porosity approaches 100%. This highlights the slowdown of porosity production through the fracture evolution stages in the clay systems as compared to the non-clay systems. It suggests that the mechanism of porosity production in the late stages of clay-dominated fracture evolution is either reduced in scale or that an altogether different mechanism begins to emerge.

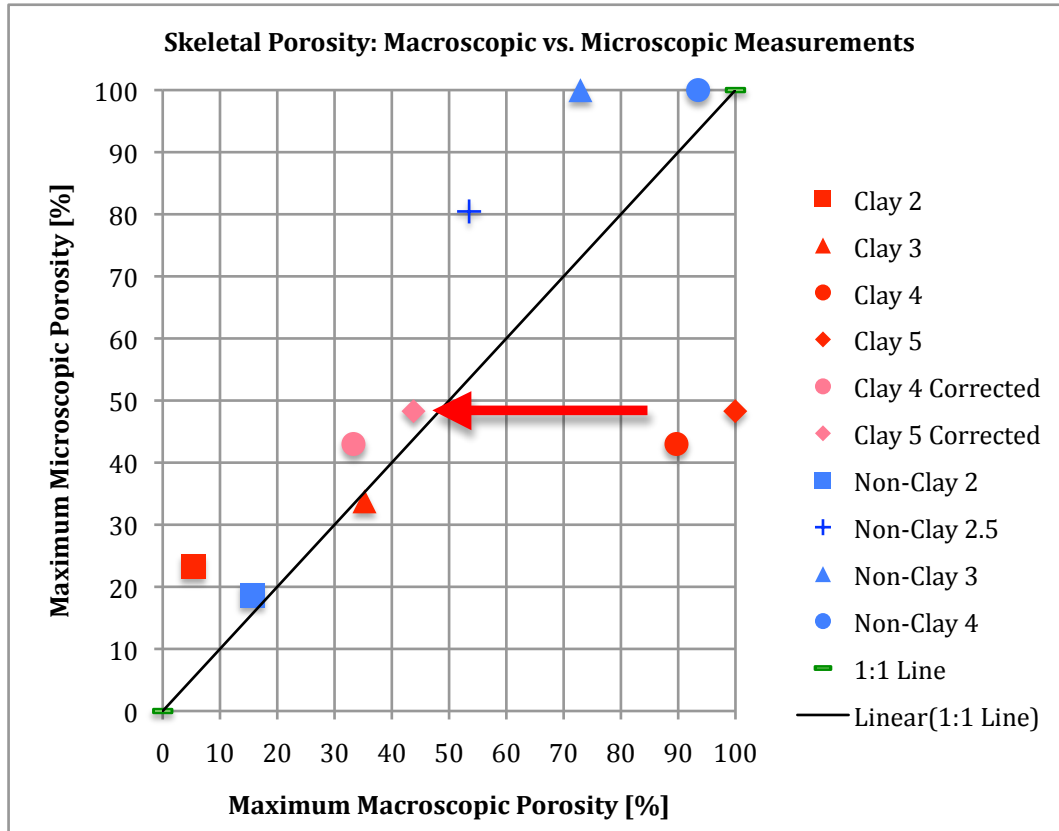


Figure 39: Comparison of the maximum skeletal porosity values found in the macroscopic measurements vs. those found in the microscopic measurements. The 1:1 reference line plots an ideal correlation between the macroscopic and microscopic measurements if they are equivalent. The arrow highlights the leftward shift of the original clay stage 4 and 5 values to the corrected clay stage 4 and 5 values.

3.4.2 Possible errors in porosity measurement

The difficulty of distinguishing between mineral alteration/replacement and dilation as mechanisms of porosity generation through fracture was previously demonstrated in Figure 39. Elemental chemistry as measured by the XRF can be used to determine if the skeletal porosity mapped in clay stages 4 and 5 is healed crack porosity or alteration of host rock. In the case of healing of dilatant fracture porosity, elements with very low solubility such as zirconium, Zr, and titanium, Ti, should have distinct concentrations compared to the host rock and in general will appear relatively depleted. However replacement of minerals through dissolution or replacement should retain concentrations of such immobile elements similar to the original host rock mineralogy. Figure 40 shows a cross-plot of these two relatively immobile (Baumgartner and Olsen, 1995, McCraig, 1997; Manatschal et al, 2000). The plot shows that the damage zone and fault rock have concentrations within the range of the host rock, which implies replacement rather than precipitation into void space from a solution (whether proximal or far travelled). This interpretation assumes that 1) the fault rock and wall rock originate from the same protolith and have the same diagenetic state prior to faulting and 2) the protolith is relative homogeneous at this length-scale and is adequately characterized by the XRF sampling as shown by reasonably narrow ranges of host rock measurements.

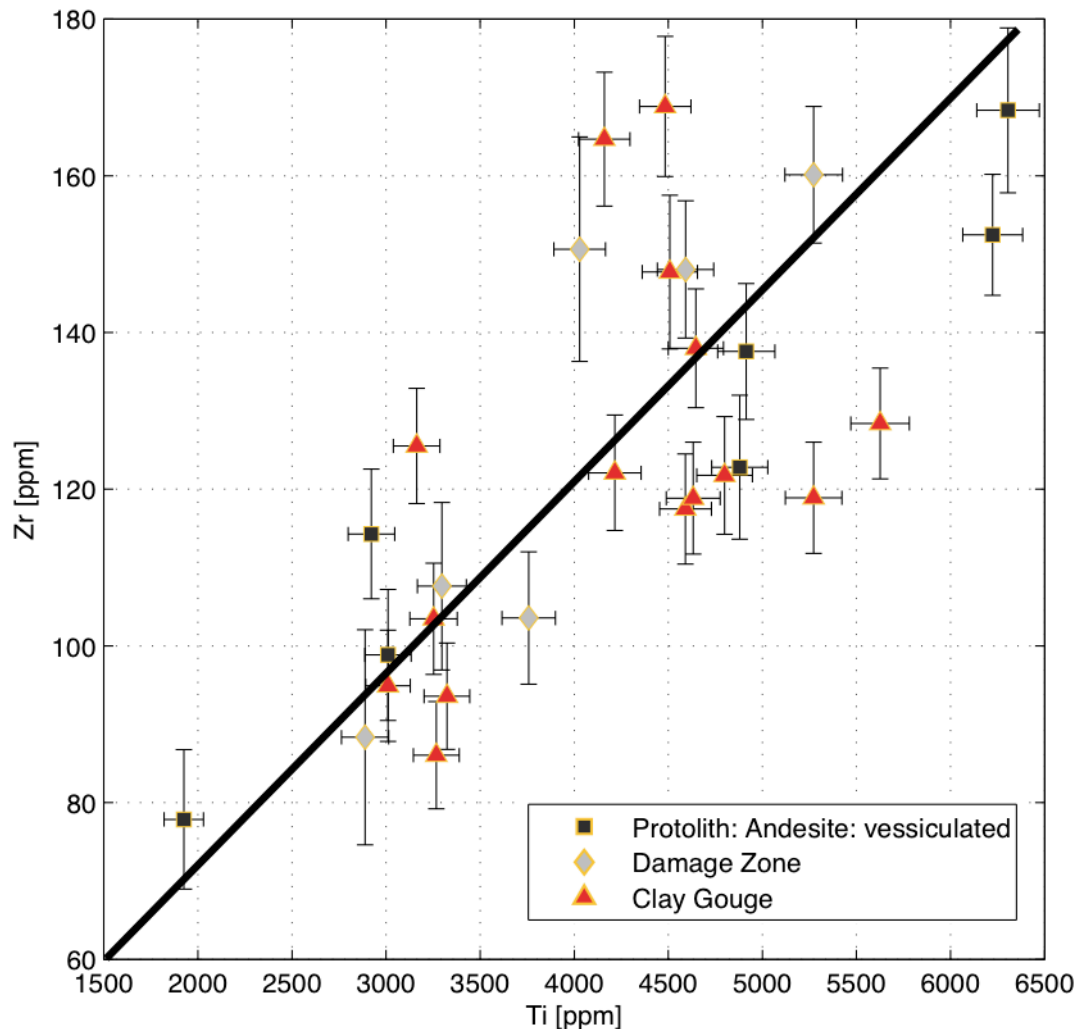


Figure 40: Plot of the elements Ti and Zr, which define a line, in clay stage 5.

In this framework, cross plots of these immobile species against more mobile species can: (1) show fluid transport and deposition into void space if there is relative enrichment of the mobile species associated with apparent depletion of the immobile species; (2) replacement if mobile species are preferentially depleted or enriched without a change in the immobile species. Figure 41 shows that the concentrations of mobile elements Ca and Sr are distinctively grouped into protolith, damage zone rock and clay gouge rock zones with little associated change in the relatively immobile species Ti. This relationship suggests the fault rock was primarily derived through mineral replacement rather than precipitation into open voids from a solution. Thus the large skeletal porosity in clay stage 5 is largely derived from alteration and not fracture-induced dilation.

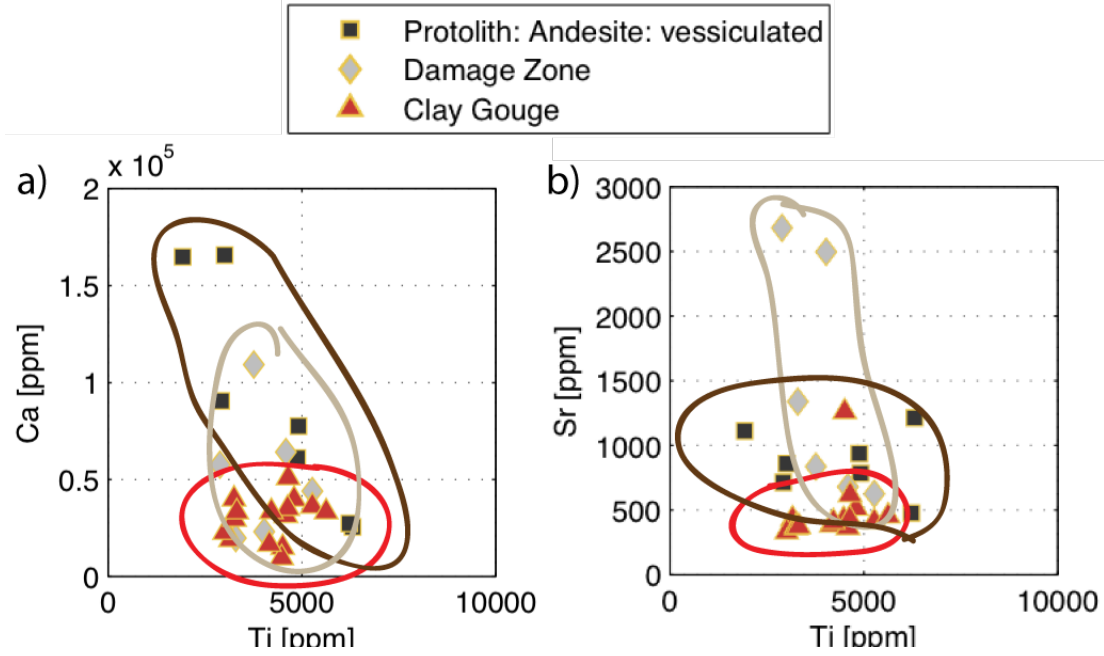


Figure 41: XRF plots for clay stage 5. The circles highlight distinct rock groups; brown is the unaltered protolith rock, gray is the damage zone rock and red is the fault rock.

3.4.3 Method to correct macroscopic porosities in clay stages 4 and 5

This suggests that the skeletal porosity in clay stage 5 most likely to be altered host rock and does not reveal a history of repeated dilation. To distinguish this difference in mechanism, the following steps and calculations were made: 1) The microscopic measurements were grouped into two distinct zones: fault zone and damage zone. 2) The average porosity value for each zone was calculated. 3) The macroscopic measurements were grouped into three distinct zones: fault zone, damage zone, and host rock. 4) Each macroscopic porosity measurement along the core was multiplied by the zone-appropriate microscopic porosity average calculated in step 2. However, the macroscopic host rock porosity values were left unchanged, because the microscopic porosity values were not documented in some of the thin sections due to width limitations of the slides

In addition, the following steps were taken to factor in the open porosity measured on microscopic level: 5) Steps 1-3 were repeated for open porosity measurements. 6) The zone-appropriate open porosity was *added* to each macroscopic porosity along the transect (because each macroscopic open porosity measurement was zero).

These steps give an adjusted interpretation of the dilation revealed by macroscopic porosity mapping in section 3.3.1 and reflects the mineral alteration that is the primary source for elemental transport discussed in section 3.3.2.

Steps 1-4 were also applied to clay stage 4 because it also exhibited anomalous behavior discussed in section 3.3.1. Figure 42 plots the corrected skeletal porosity for clay stages 4 and 5 against the original values of all the clay stages for comparison.

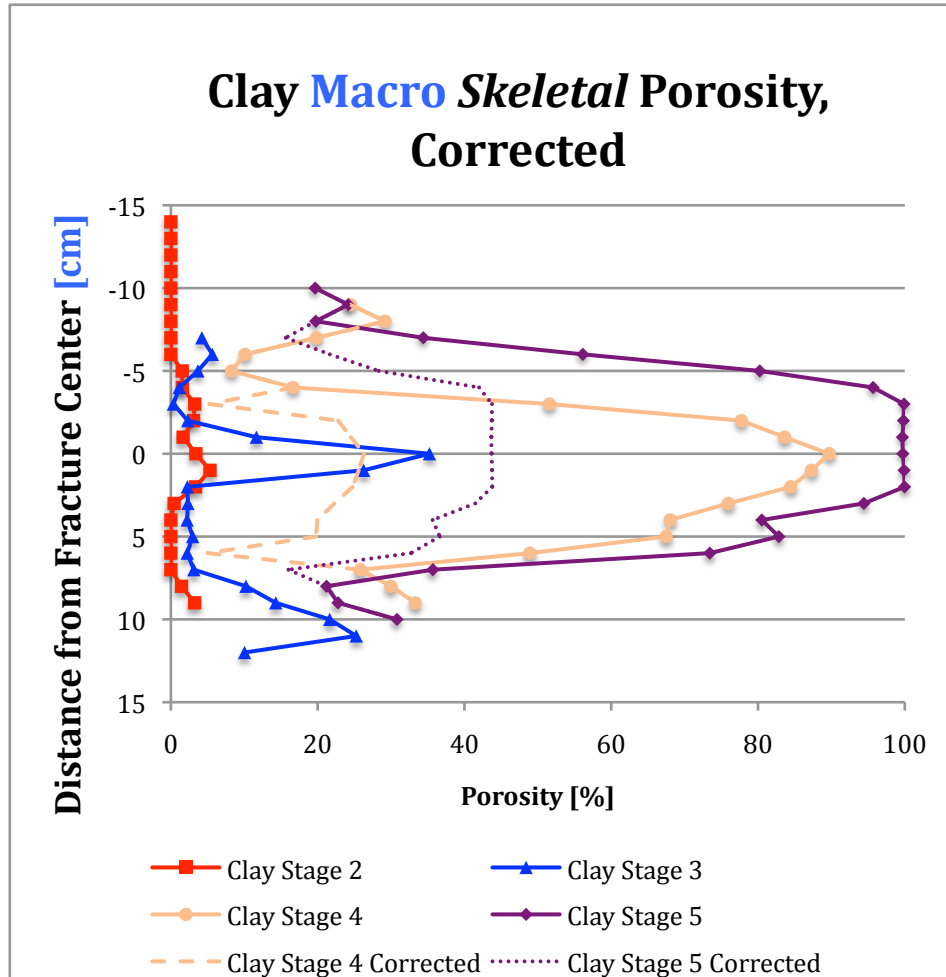


Figure 42: Skeletal porosity across all clay groups. Includes the adjusted values for clay stage 4 and 5.

3.5 XRD Analysis Results

Table 2 presents the XRD analysis showed that a wide range of minerals exist across the different fracture stages and in each end-member group. The XRD data was primarily used to confirm the presence of minerals deduced through petrographic analysis in the thin sections. The key minerals identified in thin section and supported by XRD analysis are pointed out in 3.1.1 and 3.2.1.

The only mineral that consistently appeared across every fracture stage in both non-clay and clay groups was quartz. Therefore, quartz was chosen as an indicator mineral to be examined for patterns consistent with increasing quartz content in evolving fracture development.

3.5.1 Using quartz weight % as an indicator of fracture stage and porosity

Quartz was found in both clay and non-clay fracture systems, stages 2-5. It is a major mineral constituent in the protolith but also was found in significant volumes, along with calcite, in the fracture-filling cementing material. Analysis of microscopic porosity

revealed that the weight percentage of quartz in a fracture system relative to its weight percentage in the host rock follows an upward trend. That is, quartz constituted an increasing percentage in each progressive fracture stage for both groups. Therefore, quartz may act as an indicator mineral for fracture evolution in this location.

The plots in figure 38a does not demonstrate any significant trends between quartz enrichment in fracture rock and and the stage of evolution in non-clay systems. The fracture rock, however, is consistently enriched with quartz relative to the host rock. This is expected in non-clay systems, which are, by definition, fractures filled with calcite and quartz precipitates.

A correlation between quartz and the stage of fracture evolution is apparent clay systems (Figure 38b). In stages 2-4 stages of fracture evolution the fracture zone is depleted in quartz relative to the host rock. Progressing through these stage the quartz depletion nears 0. Then in stage 4 the fracture system becomes enriched in quartz relative to the host rock.

The data that is plotted suggest that non-clay systems become more enriched in quartz than clay systems, and at earlier stages. These results are consistent with the idea that at more evolved stages non-clay systems are preferentially enriched in high-strength cementing minerals like quartz as compared to clay-dominated systems that by definition consist of other, lower-strength minerals.

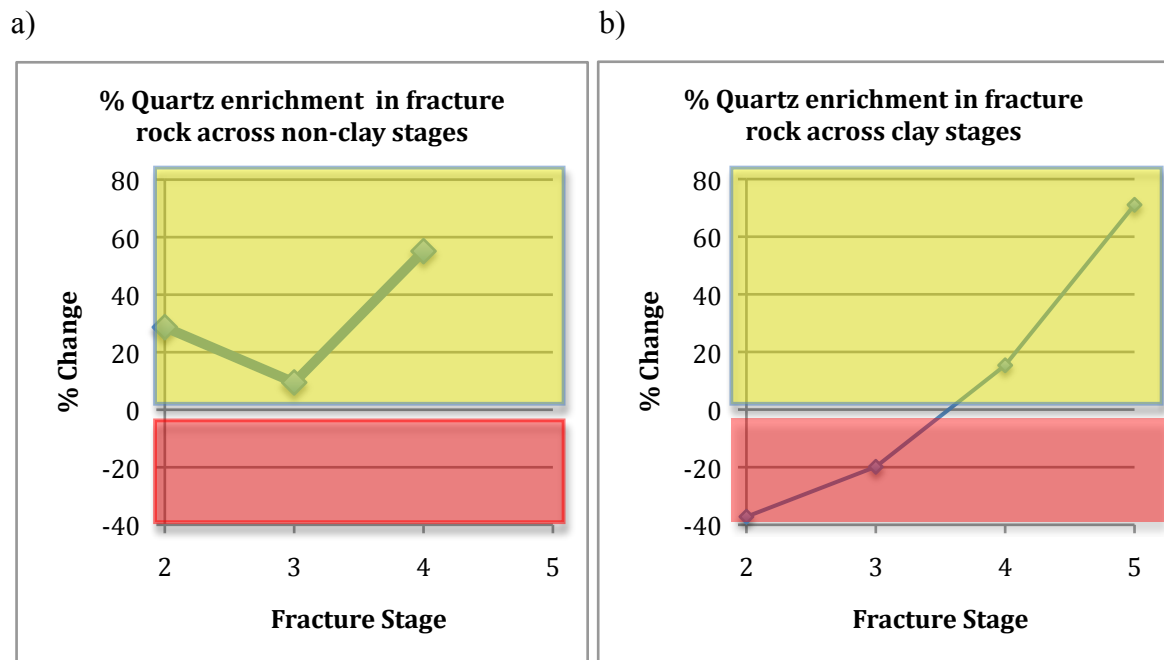


Figure 43: Charts plotting $[(\text{Weight \% of quartz in fracture rock}) - (\text{weight \% of quartz in host rock})] / (\text{weight \% of quartz in host rock})$ at each stage of host rock from representative XRD samples. The red shaded area indicates fracture zones that are depleted of quartz compared to the host rock. The yellow shaded area indicates fracture zones that are enriched in quartz compared to the host rock.

Beyond this confirmation of mineral categorization, however, lies the potential for quartz as an indicator of secondary porosity that is preferentially associated with the dilation of the rock volume or fracture during deformation. More samples at each fracture stage must be measured in order to obtain a statistically relevant correlation.

4 DISCUSSION

4.1 Implications for Open Porosity in Fracture Systems

Open porosity is essential to geothermal circulation development for several reasons. It is an indicator of recent fracturing, and therefore a good demonstration of how a system will fracture when artificially induced. Open porosity is also necessary to create connected porosity, a pre-requisite to permeability and fluid flow.

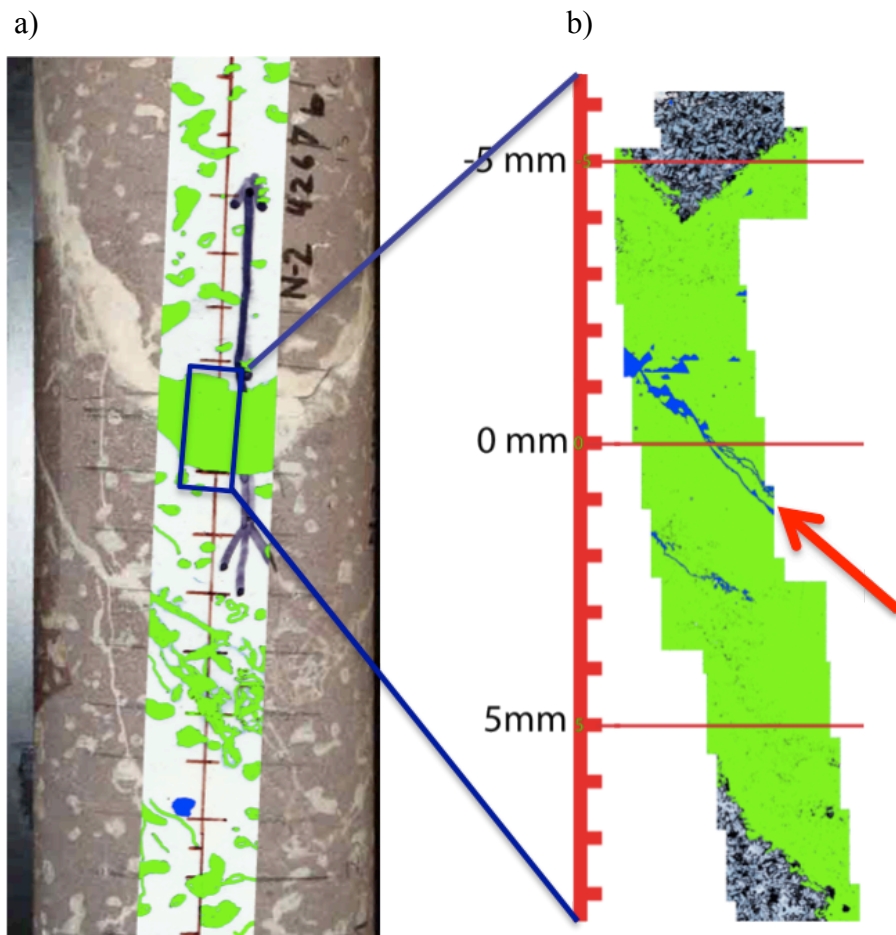
For these reasons the circumstances in which open porosity is a critical control on the development of hydrothermal systems, prospecting for hidden resources, or creating it in engineered systems. The results of this study imply that open porosity is only generated in highly evolved systems (in clay stage 5 and non-clay stages 3 and 4) and that non-clay fractures tend to produce much more open porosity than clay-filled fractures.

Whereas open porosity was only measureable under a microscope in clay-dominated systems, non-clay systems demonstrated open porosity that could be seen in hand sample. Such a significant difference in pore size impacts fluid flow as the size of the pore throat (the area across which fluid has to flow to pass from one pore to another) is a limit on permeability. The sample with the most open porosity is the non-clay stage 4. It is unclear whether a non-clay stage 5 system would have more or less open porosity. The consistent relationship of increasing open porosity with increasing fracture evolution in clay stage 2-5 and in and in non-clay stages 2-4 suggests that a stage non-clay stage 5 would exhibit the highest porosity.

However, the work of Moore et. al (2009) states that permeability (and thereby open porosity) peaks at the point right before the brecciation of the host rock and before significant grain size reduction commences. The fracture zones studied in Moore's paper were non-clay. As defined in this paper, brecciation begins to occur at late stage 3 to stage 4, so by following Moore's conceptual model the permeability in this study's samples should peak in stage 3. Consistent with this result, the open porosity peaks in non-clay fractures at stage 4. In the clay dominated fracture system, porosity peaks at stage 5. However, despite peaking at this late stage of the development, the porosity is largely microscopic and inspection of the thin sections suggest the pore space is largely isolated. In addition, unlike the non-clay system in slip can continue to cause cracking, textures in the clay-filled fractures suggests clays can flow resulting in at least partial preservation of pore isolation even after fracture reactivation.

Figure 44 represents the typical mechanical context of the open porosity found in the non-clay systems. The open porosity in these systems tend to be through-going, crack-like and connected. It tends to be centered in the middle of the calcite and/or silica-filled fractures. The healed porosity in the non-clay systems tends to preserve the sharp edges created in earlier fractures. All of these factors imply that dilation is the dominating porosity-generating mechanism throughout all of the non-clay fracture evolution stages.

It should be noted that the thin section shown in Figure 44b originates from a slab surface taken from the center of the core, while from purple box highlighted in Figure 44a represents the surface of the core, as explained in the methodology section 2.2. Therefore, the rock represented in each picture does not originate from the exact same location within the core sample. However, because the same non-clay fracture is represented in both Figure 44a and Figure 44b, and because they are located less than 3 cm away from each other in three-dimensional space, the two figures are comparable.



Non-clay stage 3

Figure 44: In a), the purple box highlights a ~2 cm cross-section of the non-clay stage 3 macroscopic porosity map that is enlarged in b) and represented by the non-clay stage 3 microscopic porosity map. The brown ticks in a) represent 1 cm intervals. The red arrow in b) highlights the crack-like open porosity typical of non-clay system fractures.

The only clay-dominated fracture system that showed any porosity generation was non-clay stage 5, and only in microscopic analysis. The open porosity found in thin section was limited to the damage zone within 15 mm of the damage zone/gouge zone border (Figure 45). The open porosity drops to almost zero almost immediately into the gouge zone above the 0 mm mark.

There are two types of open porosity found in the damage zone: (1) rounded porosity in relatively unaltered protolith within the damage zone and (2) crack-like porosity found within the healed porosity that permeate the damage zone. The rounded porosity is consistent with chemical dissolution of the rock. The through-going crack-like fractures within the healed porosity are similar to the crack-like open porosity found in the non-clay fracture of Figure 44, but on a smaller scale.

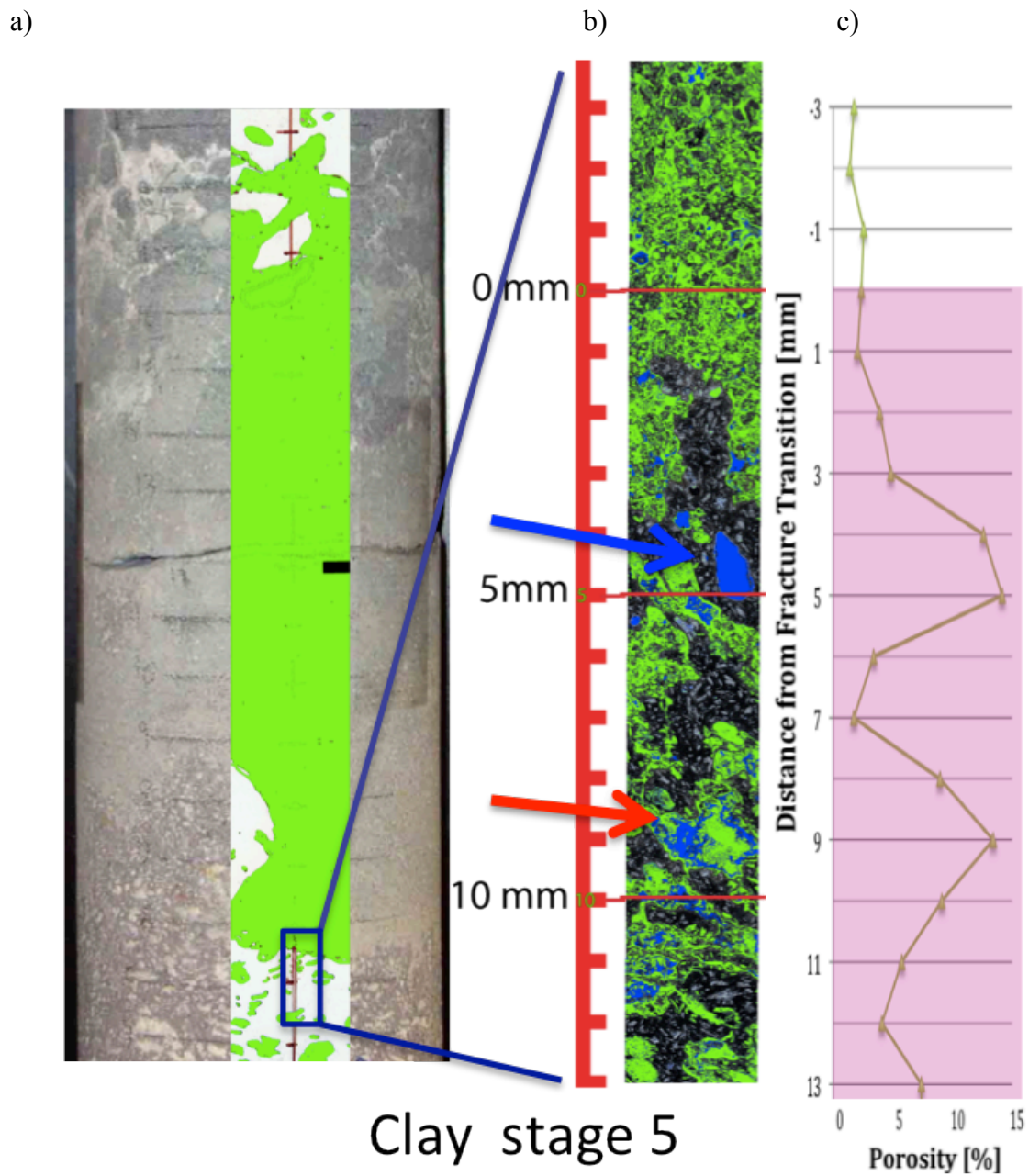


Figure 45: In a), the purple box highlights a ~2 cm cross-section of the clay stage 5 macroscopic porosity map that is enlarged in b) and represented by the clay stage 5 microscopic porosity map. The microscopic open porosity is quantified in c). The brown ticks in a) represent 1 cm intervals. The red arrows in b) highlights the through-going fracture-like porosity, and the blue arrow highlights rounded porosity consistent with dissolution of rock. The pink area highlighted in c) represents the damage zone.

Both types suggest that open porosity generated in a clay-dominated system forms parallel to the fracture zone where it is still close to the area subjected to shear deformation. However, it is limited to rock dominated by high-strength, brittle protolith and outside of the very clay-enriched areas like gouge. This confined area of damage zone just outside of the fracture rock shows calcite and silica-healed fractures, and open porosity appears to form from dilatancy during re-fracturing events, though on a very small scale as compared

to non-clay systems. The rounded porosity present in this same region may be formed by fluids flowing through this fractured damage zone outside of a relatively impermeable fracture zone that is “clogged” with clay. Both types of open porosity provide evidence to support the idea that low-strength, low-friction clay minerals act as a lubricant and sealing mechanism during shear stress deformation.

The results of this study suggest that induced fracturing for geothermal energy development would produce the highest potential fluid flow in a highly evolved non-clay fracture system. Large faults containing clay could still interact with a stimulation by channelling flow along their damage zones but also restricting flow across the fault zone thus leading to channelization of the stimulation.

4.2 A Conceptual Mechanism Model for Clay and Non-Clay Fracturing

The aim of this study was to quantify the relationship between fracture porosity and secondary mineralogy in basaltic rocks. The XRF, XRD, macroscopic and microscopic porosity analyses of this study support the following model that can explain the behavior of a fault system under shear deformation according to the dominating mineralogy that occupies its fractures.

Fracture systems filled with cement characterized by high frictional-strength, non-clay minerals like calcite and quartz (Lockner and Beeler, 2002), that are re-fractured by shear deformation will generate new porosity. This open porosity, initially only microscopic, tends to form in the center of the fracture with some grain scale porosity in the fracture walls. The macroscopic porosity data shows that the porosity of a non-clay system continuously increases with each progressive fracture stage. The porosity tends to remain limited to the fracture zone and does not propagate very far into the damage zone surrounding the fracture.

The XRF data shows that with each re-fracturing event, the porosity generated allows an inflow of new exotic material with a different elemental chemistry than the host rock. The distribution of this new material throughout the fracture zone and into the damage zone can be traced by the increase or decrease of immobile elements across the width of the measured high-porosity zone.

As the fracture system continues to evolve into the advanced stage of brecciation, porosity peaks. Open, macroscopic porosity develops. XRF analysis shows that exotic material flowing into the system begins to seep into cracks beyond the primary fracture zone, giving the damage zone a chemical signature falling between the fracture and the host rock.

In non-clay systems, the XRF data shows a peak of exotic material input at the center of the fracture in every fracture stage. It suggests that a non-clay fracture system grows from the inside out, re-cracking near the center of the fracture system, injecting new material and healing itself. This injection-to-center model keeps the exotic material localized within the fracture core and explains the sharp drop-off of porosity outside of the fracture zone in non-clay systems. If repeated enough times, this process can grow a non-clay fracture system outward from the center.

A clay fracture system behaves like a non-clay system in the initial fracture stage. The fracture is a zone of dilation and is filled with high-strength minerals like quartz and calcite along with weaker clay minerals. The porosity is confined close to the fracture zone. XRF data shows that the fracture material is chemically distinct from the host rock.

By stage 3 the clay fracture system begins to behave differently from the non-clay fracture system. The clay minerals in the fracture begin to become more prevalent than the high-strength cement. The clay minerals begin to plug up the fracture and inhibit porosity generation there. The source of new porosity generation becomes directed to the damage zones parallel to the fracture, where high-strength cements continue to flow into new cracks. XRF analysis shows that the fracture is still chemically distinct from the host rock.

In stage 4, the clay has become prevalent enough to effectively clog the fracture system. XRF analysis shows that new exotic material ceases to flow into the center of the fracture system, though it still flows in along the fracture/damage zone border. Chemical alteration of the fracture zone occurs. The chemical signatures of the host rock and fracture zone become less distinct as they begin to trade ions. By stage 5 the center of the fracture is so clogged that new porosity generation effectively ceases. Skeletal porosity asymptotically approaches a maximum of about 50%. The only new generation of porosity occurs in the damage zone, outside of the clay-dominated fracture zone as shown in the macroscopic porosity data.

The driving mechanism behind the widening of the clay system then is a combination of alteration and dilation. The dilation occurs on a microscopic level along the edge of the clay gouge. As the system evolves, alteration becomes significantly more prevalent than dilation. As a whole the system becomes anisotropic with porosity limited to the margins of the fault where some host rock remains intact. This generation of porosity allows enough fluid to flow in to promote alteration of the damage zone into clay but not to contribute significant mass or exotic chemistry suggesting fluid flow might only occur over short length-scales. This process widens the clay-filled fracture over time.

5 CONCLUSIONS

An unfractured body of rock, when subjected to shear stress, will begin a process of deformation that will over time create a system of increasingly numerous and complex fractures. These fractures create porosity that allows for the flow of fluids and creates potential for geothermal exploitation fluid flow and exploitation.

The fracture system will over time progress from a stage 1 to a stage 5 fracture system. As the fracture proceeds through the fracture stages, the width of the fracture system and its associated damage zone will increase in width outward from the original fracture.

If the fracture system is dominated by in flow of high-strength secondary minerals like calcite and quartz, it will generate porosity in higher and higher amounts over time. If it becomes filled with low-strength materials like clays, new porosity generation will decrease over time until the system essentially becomes choked with clay.

The highest potential for permeability and fluid flow in a geothermal system exists in a highly developed, non-clay dominated fracture system.

6 ACKNOWLEDGMENTS

There is no way I could not have accomplished this thesis without the support of many, many people. I would first like to thank my advisor Dr. Nicholas Davatzes for his unyielding support even at times when he needed to take a break more than I did. Thanks to Amelia Letvin for being my partner in crime under Nick's guidance and for helping me gather my data both in Salt Lake City and in Philadelphia. I want to thank the graduate department staff and students of Temple University's geology department for getting me to the United States and then helping me feel at home once I arrived. Specifically I want to thank Steve Peterson, Mike Swyer, Luke Walsh and Jesse Thornburg for helping me prepare and run my XRD samples and analyzing them with a skill and persistence that I could only hope to match. Thank you to Alexandra Davatzes, Madhi Narayanan, Shelah Cox, Jim Ladd and Kelly Blake for helping get me on my feet and running around Temple like a true "visiting scholar." Thanks goes out to the EGI Utah core library for allowing me to nab their core samples. Specifically, thank you Bridget Ayling, Peter Rose and David Langton, the rock man. I want to thank the students of RES for sharing with me the most unforgettable year of my life. Thanks to the RES staff for making it last while it could. And finally, thanks to my parents who locked me in their attic during the final month of my thesis so I could focus on writing this paper.

7 TABLES

7.1 Table 1

Table 1: Core samples used for measurements in this study. Includes name of well at Newberry that core was extracted from, the depth from which the core was extracted, the dominating mineralogy of the fracture system, its stage of fracture development, and the section of the fracture that the core sample belongs to.

Well	Measured Depth [feet]	Measured Depth [meters]	Fracture Mineralogy	Stage	Section
N2	3523	1073.8	Non-clay	4	Protolith Hanging Wall
N2	3523.5	1073.9	Non-clay	4	Fracture
N2	3617	1102.4	Clay	2	Fracture
N2	3617	1102.4	Clay	2	Protolith Footwall
N2	3936	1199.6	Non-clay	2	Protolith Hanging Wall
N2	3937	1199.9	Non-clay	2	Fracture
N2	3937.5	1200.1	Non-clay	2	Protolith Footwall
N2	4152	1265.5	Non-clay	2.5	Protolith Hanging Wall
N2	4152	1265.5	Non-clay	2.5	Fracture
N2	4152	1265.5	Non-clay	2.5	Protolith Footwall
N2	4267	1300.5	Non-clay	3	Fracture
N2	4267	1300.5	Non-clay	3	Protolith Footwall
N2	4302	1311.2	Clay	4	Fracture
N2	4303	1311.5	Clay	4	Protolith Footwall
N2	4305	1312.1	Clay	5	Protolith Hanging Wall
N2	4306	1312.4	Clay	5	Fracture
N2	4308	1313.0	Clay	5	Protolith Footwall
N2	4338	1322.2	Clay	3	Protolith Hanging Wall
N2	4338	1322.2	Clay	3	Fracture
N2	4339	1322.5	Clay	3	Protolith Footwall

7.2 Table 2

Table 2: XRD results. Column 1 is the well number and depth at which the sample run for XRD analysis was retrieved from in measured depth. Column 2 identifies the fracture end-member and the stage. Lines highlighted yellow in this column identifies data was produced from rock that that lay adjacent to the thin taken of the fracture. Lines colored in orange indicate the samples designated as the best representation of host rock. Column 3 describes the part of the fracture that the sample was taken from. Column 4 designates the number of sample if multiple pieces were sampled from the same feature described in column 3. Column 5 lists the mineral identified in the sample by XRD. Column 6 lists the weight fraction of the mineral found in the sample.

Depth	Stage	Zone	Sect ion	Mineral	Wt%
N2-3617	Clay 2	Fracture		Albite	75.6
N2-3617	Clay 2	Fracture		Augite	13.2
N2-3617	Clay 2	Fracture		Quartz	7.6
N2-3617	Clay 2	Fracture		Hectorite	3.6
N2-3617	Clay 2	PFW (B)		Albite	85.6
N2-3617	Clay 2	PFW (B)		Quartz	8.6
N2-3617	Clay 2	PFW (B)		Montmorillonite	6.8
N2-3617	Clay 2	PFW (A)		Albite	73.3
N2-3617	Clay 2	PFW (A)		Quartz	12.1
N2-3617	Clay 2	PFW (A)		Augite	7.1
N2-3617	Clay 2	PFW (A)		Montmorillonite	5.9
N2-3617	Clay 2	PFW (A)		Calcite	1.6
N2-4338	Clay 3	Fracture		Albite	39.4
N2-4338	Clay 3	Fracture		Quartz	36.7
N2-4338	Clay 3	Fracture		Calcite	6.8
N2-4338	Clay 3	Fracture		Chlorite	4.9
N2-4338	Clay 3	Fracture		Fayalite	4.9
N2-4338	Clay 3	Fracture		Muscovite	4.3
N2-4339	Clay 3	PFW		Quartz	45.8
N2-4339	Clay 3	PFW		Albite	42.3
N2-4339	Clay 3	PFW		Fayalite	5.4
N2-4339	Clay 3	PFW		Calcite	4.9
N2-4339	Clay 3	PFW		Pyrite	1.6
N2-4302	Clay 4	Fracture B	2/2	Quartz	34.4
N2-4302	Clay 4	Fracture B	2/2	Albite	33.5
N2-4302	Clay 4	Fracture B	2/2	Dolomite	9.8
N2-4302	Clay 4	Fracture B	2/2	Fayalite	6.9

N2-4302	Clay 4	Fracture B	2/2	Illite	5.5
N2-4302	Clay 4	Fracture B	2/2	Calcite	3
N2-4302	Clay 4	Fracture B	2/2	Clinochlore	2.8
N2-4303	Clay 4	Fracture B	2/2	Pigeonite	2.2
N2-4304	Clay 4	Fracture B	2/2	Sederholmite	1.9
N2-4302	Clay 4	Fracture B	1/2	Quartz	28.4
N2-4302	Clay 4	Fracture B	1/2	Albite	25.6
N2-4302	Clay 4	Fracture B	1/2	Dolomite	15.4
N2-4302	Clay 4	Fracture B	1/2	Maghemite	8.1
N2-4302	Clay 4	Fracture B	1/2	Hematite	6.8
N2-4302	Clay 4	Fracture B	1/2	Illite	6.2
N2-4302	Clay 4	Fracture B	1/2	Clinochlore	4.2
N2-4302	Clay 4	Fracture B	1/2	Chalcopyrite	3
N2-4302	Clay 4	Fracture B	1/2	Pigeonite	2.1
N2-4302	Clay 4	Fracture A	2/2	Quartz	45.8
N2-4302	Clay 4	Fracture A	2/2	Albite	21
N2-4302	Clay 4	Fracture A	2/2	Dolomite	13.8
N2-4302	Clay 4	Fracture A	2/2	Illite	4.2
N2-4302	Clay 4	Fracture A	2/2	Hematite	4.1
N2-4302	Clay 4	Fracture A	2/2	Fayalite	3.5
N2-4302	Clay 4	Fracture A	2/2	Clinochlore	3
N2-4302	Clay 4	Fracture A	2/2	Chalcopyrite	2.3
N2-4302	Clay 4	Fracture A	2/2	Pigeonite	1.5
N2-4302	Clay 4	Fracture A	2/2	Chalcophanite	0.8
N2-4303	Clay 4	PFW B		Quartz	50
N2-4303	Clay 4	PFW B		Dolomite	20.3
N2-4303	Clay 4	PFW B		Albite	15.1
N2-4303	Clay 4	PFW B		Chalcopyrite	6.3
N2-4303	Clay 4	PFW B		Hematite	3.9
N2-4303	Clay 4	PFW B		Clinochlore	3.6
N2-4303	Clay 4	PFW B		Anhydrite	0.8
N2-4303	Clay 4	PFW A		Quartz	39.7
N2-4303	Clay 4	PFW A		Albite	23
N2-4303	Clay 4	PFW A		Calcite	15.2
N2-4303	Clay 4	PFW A		Dolomite	10.4
N2-4303	Clay 4	PFW A		Hematite	5.2
N2-4303	Clay 4	PFW A		Clinochlore	4.3
N2-4303	Clay 4	PFW A		Pigeonite	2.2
N2-4305	Clay 5	PHW		Quartz	43.9
N2-4305	Clay 5	PHW		Albite	23.3
N2-4305	Clay 5	PHW		Montmorillonite	9
N2-4305	Clay 5	PHW		Hematite	7
N2-4305	Clay 5	PHW		Chalcopyrite	6.7
N2-4305	Clay 5	PHW		Gypsum	3.4
N2-4305	Clay 5	PHW		Pigeonite	2.5

N2-4305	Clay 5	PHW		Fayalite	2.4
N2-4305	Clay 5	PHW		Clinochlore	1.6
N2-4305	Clay 5	Fracture B		Quartz	60.3
N2-4305	Clay 5	Fracture B		Calcite	13.2
N2-4305	Clay 5	Fracture B		Albite	10.5
N2-4305	Clay 5	Fracture B		Clinochlore	6.3
N2-4305	Clay 5	Fracture B		Anhydrite	3.7
N2-4305	Clay 5	Fracture B		Hematite	3.4
N2-4305	Clay 5	Fracture B		Dolomite	2.2
N2-4305	Clay 5	Fracture B		Pigeonite	0.4
N2-4306	Clay 5	Fracture A	2/2	Quartz	75.1
N2-4306	Clay 5	Fracture A	2/2	Albite	16.1
N2-4306	Clay 5	Fracture A	2/2	Clinochlore	8.8
N2-4306	Clay 5	Fracture A	1/2	Albite	29.5
N2-4306	Clay 5	Fracture A	1/2	Quartz	26.1
N2-4306	Clay 5	Fracture A	1/2	Dolomite	19.2
N2-4306	Clay 5	Fracture A	1/2	Montmorillonite	8.8
N2-4306	Clay 5	Fracture A	1/2	Hematite	6.6
N2-4306	Clay 5	Fracture A	1/2	Magnetite	6.1
N2-4306	Clay 5	Fracture A	1/2	Clinochlore	3.7
N2-4308	Clay 5	PFW		Dolomite	61.2
N2-4308	Clay 5	PFW		Quartz	13
N2-4308	Clay 5	PFW		Chalcopyrite	8.5
N2-4308	Clay 5	PFW		Albite	7.1
N2-4308	Clay 5	PFW		Hematite	3.4
N2-4308	Clay 5	PFW		Illite	2.3
N2-4308	Clay 5	PFW		Clinochlore	2.2
N2-4308	Clay 5	PFW		Orthclase	1.7
N2-4308	Clay 5	PFW		Epidote	0.5
N2-3936	Calcite 2	PHW		Albite	72.9
N2-3936	Calcite 2	PHW		Augite	12.9
N2-3936	Calcite 2	PHW		Quartz	10.8
N2-3936	Calcite 2	PHW		Hectorite	3.4
N2-3937	Calcite 2	Fracture (B)	1/2	Albite	76.7
N2-3937	Calcite 2	Fracture (B)	1/2	Quartz	8.8
N2-3937	Calcite 2	Fracture (B)	1/2	Calcite	6.5
N2-3937	Calcite 2	Fracture (B)	1/2	Augite	5.8
N2-3937	Calcite 2	Fracture (B)	1/2	Hematite	2.2
N2-3937	Calcite 2	Fracture (A)	2/3	Albite	70.6
N2-3937	Calcite 2	Fracture (A)	2/3	Quartz	13.9
N2-3937	Calcite 2	Fracture (A)	2/3	Calcite	6.8
N2-3937	Calcite 2	Fracture (A)	2/3	Augite	4.8
N2-3937	Calcite 2	Fracture (A)	2/3	Hectorite	2.1

N2-3937	Calcite 2	Fracture (A)	2/3	Hematite	1.8
N2-3937	Calcite 2	Fracture (A)	1/3	Albite	71.1
N2-3937	Calcite 2	Fracture (A)	1/3	Calcite	11.3
N2-3937	Calcite 2	Fracture (A)	1/3	Augite	8.2
N2-3937	Calcite 2	Fracture (A)	1/3	Chlorite	5.7
N2-3937	Calcite 2	Fracture (A)	1/3	Hectorite	3.6
N2-3937	Calcite 2	PFW (B)		Albite	55.7
N2-3937	Calcite 2	PFW (B)		Quartz	32.7
N2-3937	Calcite 2	PFW (B)		Hematite	5.2
N2-3937	Calcite 2	PFW (B)		Orthoclase	4.3
N2-3937	Calcite 2	PFW (B)		Fayalite	1.1
N2-4267	Calcite 3	F (B)		Quartz	42.7
N2-4267	Calcite 3	F (B)		Albite	22.4
N2-4267	Calcite 3	F (B)		Dolomite	9.3
N2-4267	Calcite 3	F (B)		Hematite	8.6
N2-4267	Calcite 3	F (B)		Calcite	8.4
N2-4267	Calcite 3	F (B)		Montmorillonite	7.5
N2-4267	Calcite 3	F (B)		Clinochlore	1.1
N2-4267	Calcite 3	F (A)		Quartz	46.4
N2-4267	Calcite 3	F (A)		Albite	21
N2-4267	Calcite 3	F (A)		Hematite	8.7
N2-4267	Calcite 3	F (A)		Calcite	7
N2-4267	Calcite 3	F (A)		Dolomite	7
N2-4267	Calcite 3	F (A)		Tosudite	5.7
N2-4267	Calcite 3	F (A)		Montorillonite	3.5
N2-4267	Calcite 3	F (A)		Pigeonite	0.7
N2-4267	Calcite 3	PFW		Quartz	39
N2-4267	Calcite 3	PFW		Albite	28.6
N2-4267	Calcite 3	PFW		Montmorillonite	11.3
N2-4267	Calcite 3	PFW		Hematite	9.8
N2-4267	Calcite 3	PFW		Gypsum	5.5
N2-4267	Calcite 3	PFW		Chalcopyrite	4.9
N2-4267	Calcite 3	PFW		Clinochlore	0.9
N2-3523	Calcite 4	PHW		Albite	46.9
N2-3523	Calcite 4	PHW		Quartz	37
N2-3523	Calcite 4	PHW		Bytownite	7.9
N2-3523	Calcite 4	PHW		Anhydrite	3.3
N2-3523	Calcite 4	PHW		Hematite	2.8
N2-3523	Calcite 4	PHW		Pigeonite	2.1
N2-3523.5	Calcite 4	Fracture		Quartz	57.4
N2-3523.5	Calcite 4	Fracture		Albite	16.1
N2-3523.5	Calcite 4	Fracture		Chalcopyrite	15.6

N2-3523.5	Calcite 4	Fracture		Maghemite	5.6
N2-3523.5	Calcite 4	Fracture		Augite	2.4
N2-3523.5	Calcite 4	Fracture		Forsterite	1.7
N2-3523.5	Calcite 4	Fracture		Nontronite	1.3
N2-3523.5	Calcite 4	Splay Fracture		Albite	46.2
N2-3523.5	Calcite 4	Splay Fracture		Quartz	44.6
N2-3523.5	Calcite 4	Splay Fracture		Orthoclase	4.6
N2-3523.5	Calcite 4	Splay Fracture		Hematite	1.9
N2-3523.5	Calcite 4	Splay Fracture		Pigeonite	1.8

BIBLIOGRAPHY

- Achauer, U., Evans, J.R., and Stauber, D.A. (1988). High-resolution seismic tomography of compressional wave velocity structure at Newberry volcano, Oregon Cascade Range. *Journal of Geophysical Research*, v. 93, no. B9, p. 10,135-10,147.
- Almeida, R. (2007). Mesoscale fracture fabric and paelostress along the San Andreas Fault at SAFOD. Submitted to the Office of Graduate Studies of Texas A&M University in partial fulfillment of the requirements for the degree of Master of Science. Unpublished.
- Baumgartner, L. P. and S.N. Olsen (1995). A least-squares approach to mass transport calculations using the isocon method, *Econ. Geol.*, 90, 1261-1270.
- Bargar, K. and Keith, T. (1999). Hydrothermal Mineralogy of Core from Geothermal Drill Holes at Newberry Volcano, Oregon. U.S. Geological Survey Professional Paper 1578. p. 2.
- Bos, B. and Spiers, C.J. (2002). Fluid-assisted Healing Processes in Gouge-bearing Faults; Insights from Experiments on Rock Analogue System, *Pure and Applied Geophysics*, v. 159, p. 2,537-2,566.
- Brown, S.R. (1987). Fluid flow through rock joints: Effects of surface roughness. *Journal Geophysical Research*, v. 99, p. 9373-9390.
- Caine, J. S., Evans, J. P., Forster, C. B. (1996). Fault zone architecture and permeability structure, *Geology* 24, 1025–1028.
- Davatzes, N. C. and Hickman, S. H. (2010). The feedback between stress, faulting, and fluid flow: Lessons from the Coso Geothermal Field, CA, USA. *Proceedings World Geothermal Congress 2010. Bali, Indonesia, 25-29 April 2010.*
- Fitterman, D.V. (1988). Overivew of the structure and geothermal potential of Newberry Volcano, Oregon. *Journal of Geophysical Research*, v. 93, no. B9, p. 10,059-10,066.
- Freeze, R. A. and Cherry, J. A. (1979). Groundwater. Prentice-Hall. London, England, 617 p.
- Jaeger, J.C., Cook, N.G.W., and Zimmerman, R.W. (2007), Fundamentals of Rock Mechanics; Fourth Edition. Blackwell Publishing, Malden, Massachusetts, USA, 475 p.
- Karner, S.L., Marone, C., and Evans, B. (1997) Laboratory study of fault healing and lithification.
- Laubach, S. E. and Ward, M. E. (2006). Diagenesis in porosity evolution of opening-mode fractures, Middle Triassic to Lower Jurassic La Boca Formation, NE Mexico. *Tectonophysics*, v. 419, p. 75–97.
- Lockner, D.A. and N.M. Beeler (2002). Rock failure and earthquakes. *International Handbook of Earthquake and Engineering seismology*, v. 81A, p. 505-537.

- Manatschal, G., Marquer, D., Frueh-Gree, G. L. (2000), Channelized fluid flow and mass transfer along a rift-related detachment fault (eastern Alps, southeast Switzerland, Geological Society of America Annual Bulletin, 112 (1), p. 21-33.
- McCraig, A. M. (1997), The geochemistry of volatile fluid flow in shear zones, Deformation-Enhanced Fluid Transport in the Earth's Crust and Mantle, vol. 8, Chapman and Hall, London, p 227-266.
- McWhorter, D. B. and Sunada, D.K. (1977). Ground-Water Hydrology and Hydraulics: Water Resources Publications, LLC. Fort Collins, Colorado, p. 18.
- Moore, D.E., Lockner, D.A. and Byerlee, J.D. (1994). Reduction of permeability in granite at elevated temperatures. Science, v. 265, p. 1558–1561.
- Moore, D. E., Lockner, D. A., Ito, H., Ikeda, R., Tanaka, H., Omura, K. (2009). Geometry of the Nojima Fault at Nojima-Hirabayashi, Japan – II. Microstructures and their Implications for Permeability and Strength. Pure and Applied Geophysics, v .166, p. 1669–1691.
- Morris, D. A. and Johnson, A. I. (1967). Summary of hydrologic and physical properties of rock and soil materials as analyzed by the Hydrologic Laboratory of the U.S. Geological Survey. U.S. Geological Survey Water-Supply Paper 1839-D, p. 42.
- Morrow, C.A., Moore, D.E. and Lockner, D.A. (2001) Permeability reduction in granite under hydrothermal conditions. Journal of Geophysical Research, v. 106(B12), p 30,551-30,560.
- Paterson, M.S. and Wong, T.-f. (2005). Experimental Rock Deformation: Brittle Field, 2nd Edition. Springer, New York, 348 p.
- Schleicher, A. M., van der Pluijm, B.A., Solum, J.G., Warr, L. N. (2006). Origin and significance of clay-coated fractures in mudrock fragments of the SAFOD borehole (Parkfield, California). Geophysical Research Letters, v. 33, L16313, 5 p.
- Schleicher, A. M., Tourscher, S. N., van der Pluijm, B. A., Warr, L. N. (2009). Constraints on mineralization, fluid-rock interaction, and mass transfer during faulting at 2–3 km depth from the SAFOD drill hole. Geophysical Research Letters, v. 114, B04202, 12 p.
- Sibson, R. H. (2003). Thickness of the seismic slip zone. Bulletin of the Seismology Society of America, 93, 1169– 1178.
- Vrolijk, P. and van der Pluijm, B. A. (1999). Clay gouge. Journal of Structural Geology 21, 1039– 1048.
- Yasuahara, Polak, Mitani, Grader, Halleck and Elsworth (2006) Evolution of fracture permeability through fluid-rock reaction under hydrothermal conditions, Earth and Planetary Science Lettes, v. 224(1-2), p. 186-200.